

ABSTRACT

GOKCE, BILAL. Measurement and Control of In-plane Surface Chemistry at the Si/SiO₂ Interface. (Under the direction of Professor Kenan Gundogdu).

In-plane directional control of surface chemistry during interface formation can lead to new opportunities regarding device structures and applications. Control of this type requires techniques that can probe and hence provide feedback on the chemical reactivity of bonds not only in specific directions but also in real time. In this thesis work, I demonstrate both control and measurement of the oxidation of H-terminated Si(111).

The nonlinear optical tool of Second-Harmonic-Generation (SHG) is used to show that Si oxidation in air is a two-stage process where the H of the “up” bonds of the outermost Si layer is replaced by OH, followed by O insertion into the “back” bonds. Detailed information about both stages is revealed by investigating the effect of uniaxial strain and carrier concentration on this chemical reaction. It is shown that even small amounts of strain manipulate the reaction kinetics of surface bonds significantly, with tensile strain enhancing oxidation and compressive strain retarding it. This dramatic change suggests a strain-driven charge transfer mechanism between Si–H up bonds and Si–Si back bonds in the outer layer of Si atoms.

Data on differently doped samples reveal that high concentrations of electrons increase the chemical reactivity of the outer-layer Si-Si back bonds relative to the Si-H up bonds while high concentrations of holes cause a greater increase in the reactivity of the Si–H up bonds than that of the Si–Si back bonds. However, the thicknesses of the natural oxides of all samples follow the same path and stabilize near 1 nm at room temperature, regardless of the chemical kinetics of the different bonds, as determined by spectroscopic ellipsometry.

Real-time measurement during SHG experiments is achieved by analyzing SHG anisotropy data with the anisotropic bond-charge model of nonlinear optics where peaks in the SHG spectrum are correlated with the near alignment of bonds to the direction of the excitation field.

© Copyright 2012 by Bilal Gokce

All Rights Reserved

Measurement and Control of In-plane Surface Chemistry
at the Si/SiO₂ Interface

by
Bilal Gokce

A dissertation submitted to the Graduate Faculty of
North Carolina State University
in partial fulfillment of the
requirements for the degree of
Doctor of Philosophy

Physics

Raleigh, North Carolina
2012

APPROVED BY:

Kenan Gundogdu

Committee Chair

Gerald Lucovsky

David E. Aspnes

Salah M. Bedair

DEDICATION

I dedicate this thesis to my wife Emine Gokce who has supported me throughout the years of my study. I am most grateful to God for blessing me with her and I am thankful to Emine for all of her kind support, her unconditional love and for her sharing this journey and her life with me. All this wouldn't have been possible without her.

BIOGRAPHY

Bilal's story begins prior to his birth when his father Selahattin moves to Germany to study mechanical engineering but despite his brilliant intellect can't finish his university degree due to financial reasons. This incidence would cause him to strive for the academic success of his children. When the second-born and first son Bilal was born on December 22, 1983 in Krefeld, Germany to Yüksel and Selahattin Gökçe, Bilal would always obtain endless love from his parents. Being thankful to God for his parents, Bilal had a wonderful childhood and teenagehood with his father as his biggest supporter and his Math and Science tutor. Wanting to study Physics since 9th grade Bilal moved to Aachen to study Physics at RWTH Aachen University after finishing high school at Ricarda-Huch-Gymnasium in 2003. Fascinated by lasers and its applications he started to work as a Research Assistant and later as a Research Associate at Fraunhofer Institute for Laser technology in 2007. He earned his "Diplom-Physiker" degree in the field of solid state physics and laser technology in 10/2008. In his early study years it was clear to him that he wanted to pursue a doctorate. But the decision to come to the US was initiated by his then fiancé Emine. This is why before finishing his degree Bilal searched for a professor with who he might be interested working with. In 5/2008 he contacted Prof. Kenan Gundogdu and liked him immediately as a person as well as his work focusing on optics and lasers for solid-state applications. He decided to send his only application to the Physics Program of NC State University and he got accepted. When Bilal came to the US on New Year's Day 2009 not only a new year but also a new chapter in his life started. In the same year he got married to Emine, who is currently a Ph.D. candidate in the Chemistry department and expects to graduate within 2 months.

After all these years of studying Bilal's most important realization is that Selahattin Gökçe may have not earned any university degree but after earning the highest academic degree Bilal ascertains that more than any degree he is thankful for the virtues that his father has taught him.

ACKNOWLEDGMENTS

Many people have made this thesis possible.

First, I wish to thank my advisor, Prof. Kenan Gundogdu, for his support and guidance during my graduate studies. He was the one who made my transition from Germany to the US as smooth as possible. Not only was he there for academic issues but also for personal matters outside school. I will always remember the days in the laboratory when we worked 18-20 hours to do experiments some days. Those long days were worth it since I ended up being first author on 7 papers in high-impact journals. Dr. Gundogdu established a perfect atmosphere in our group and rewarded hard work with Group outing days at Lake Johnson or at the Pacific Ocean. Dr. Gundogdu, I am forever in your debt for being the best advisor that one could wish for!

Firsts are always special and are always being remembered. There are a lot of first's that I am proud to have been part of for the Gundogdu Group. I am the first student, we wrote the first paper of the group, I am the first student to give a talk at an international conference and I am the first graduate.

It has also always been an honor to work with Prof. Dave Aspnes. I always say that I have been lucky to work an enthusiastic brilliant advisor who is a rising star and with the wise and renowned Dr. Aspnes. I learned a lot from Dr. Aspnes, but his modesty has probably impressed me most. I recognize one of my favorite quotes in him which is this quote by Benjamin Franklin "To be humble to superiors is duty, to equals courtesy, to inferiors nobleness." Dr. Aspnes, thank you for your nobleness.

Also thanks to my distinguished committee members Prof. Gerald Lucovsky and Prof. Salah Bedair who I consider both as role models as persons and scientists.

Thanks to members of the Gundogdu Group: Cong, Chao, Robert, Andy, Sam and members of the Aspnes Group: Eric, Judith and Nick.

Also thanks to my fellow physics Ph.D.-students Murat An and Serdar Elhatisari for making my life as a student more fun.

I would like to thank my parents, Yüksel and Selahattin Gökçe, and my sisters Hilal, Nihal and Iclal for their constant love and support.

Especially, I thank my beloved wife, Emine, for being with me during this incredible journey. Her idea to come to the US turned out to be a good one and I am happy that we did this step

Finally, “All the thanks and praises to Allah, the Lord of all Existence” for giving me the opportunities and leading my way.

TABLE OF CONTENTS

LIST OF TABLES	viii
LIST OF FIGURES.....	ix
1 Introduction.....	1
1.1 Application of Second-Harmonic Generation to interface phenomena	3
2 Theory of nonlinear optical experiments	4
2.1 Brief history of nonlinear optical experiments	4
2.2 Light-matter interaction.....	5
2.3 Second-harmonic generation	6
2.3.1 Interface sensitivity of SHG	7
2.3.2 Macroscopic tensor-based model.....	8
2.3.3 Microscopic bond model	9
2.3.4 Back-reflection Second-harmonic Generation of Si (111).....	13
3 Experiments.....	23
3.1 Second-harmonic generation	23
3.2 Silicon.....	25
3.3 Chemical Treatment	28
3.3.1 Hydrogen Termination	28
3.3.2 Methoxylation.....	30
3.4 Application and Calculation of Strain	30
3.4.1 Application of Strain	30
3.4.2 Strain detection by Reflectance Anisotropy Spectroscopy	31
3.4.3 Strain calculation by geometrical considerations	34

3.5	Spectroscopic Ellipsometry	35
3.6	Atomic Force Microscopy	38
4	Results and Discussion	39
4.1	SHG Data Analysis	39
4.2	Effect of Strain on Oxidation of H-Si(111)	42
4.2.1	Dependence on direction of strain	43
4.2.2	Dependence on magnitude of strain	50
4.2.3	Dependence on type of strain	51
4.2.4	Real-Time Control of Surface Chemistry	55
4.3	Effect of Steps on Oxidation of H-Si(111)	56
4.4	Effect of Doping on Oxidation of H-Si(111)	59
4.4.1	n-type Surfaces	59
4.4.2	p-type Surfaces	63
4.5	Observation of Structural Dynamics	67
4.6	Oxidation of methoxylated Si(111)	69
4.7	Third-harmonic generation during oxidation of H-Si(100)	70
5	Conclusion	72
6	References	74
	APPENDICES	83
	Appendix A – Matlab Bond Model Code	84
	Appendix B – Origin Fitting function	85

LIST OF TABLES

Table A. Summary of Silicon Samples	28
Table B. Fitting parameters yielding the best fit for data in Figure 24	41
Table C. Parameters yielding the best fits of Equation 44 to the data of Figure 28	49
Table D. Parameters yielding the best fits of exponential functions to the data of Fig. 4.....	54
Table E. Parameters yielding the best fits of exponential functions of the data of Fig. 4.....	66

LIST OF FIGURES

Figure 1. Maiman's laser. This is ruby laser that emits a red beam. It was first operated at Hughes Research Laboratories in California, USA, on 16th May 1960.	4
Figure 2. Experimental second-harmonic generation setup used by Franken in 1961 (from [65]).	5
Figure 3. Illustration of frequency doubling during SHG.	6
Figure 4. SHG signal arising from interface region of amorphous SiO ₂ and crystalline Silicon.	7
Figure 5. Illustration of charge acceleration and dipole radiation caused by an incoming electric field interacting with Silicon.	12
Figure 6. Schematic of the waist (red lines) of a Gaussian beam focused on an interface with a Si crystal, drawn approximately to scale for 800 nm radiation arriving from the left with an f-number of 1. The waist asymptotically approaches the dashed lines. The effective depth over which SHG is emitted from the bulk cannot be resolved on this scale.	14
Figure 7. SHG Setup. 810 nm pulses from a Ti:sapphire oscillator are divided into two paths by the beam splitter. The sample is excited at a 45 degree angle of incidence. The SHG signal is normalized against long-term intensity fluctuations by the signal from the quartz crystal.	23
Figure 8. Screenshot of the SHG LabVIEW program user interface.	24
Figure 9. Band structure of Silicon. Calculated with the Empirical Pseudopotential Method. Arrow shows indirect band gap of 1.1eV.	25
Figure 10. Calculated dielectric function of Silicon at room temperature from Ref. [79].	26

Figure 11. Silicon Crystal is shown with three distinct bond directions. The arrow denotes the (111) direction.27

Figure 12. Illustration of Hydrogen terminated Silicon.28

Figure 13. AFM image of H-terminated Si.29

Figure 14. Illustration of methoxylated Silicon.30

Figure 15. Application of Strain.31

Figure 16. Spectra of reflectance anisotropy of Si(111) stripes strained along [1-10] (from Reference 87).32

Figure 17. Amplitude and strain values extracted from Figure 16 and plotted with a linear regression (red curve).33

Figure 18. Typical RAS spectrum with strain applied on Si(111) sample33

Figure 19. Deformation of laser beam focus after being reflected from a surface that is bent over a cylindrical mandrel.34

Figure 20. Spectroscopic ellipsometry setup.36

Figure 21. (a) Calculated changes from 1.5 to 6.0 eV expected in the $\cos(2\omega t)$ and $\sin(2\omega t)$ coefficients of the intensity measured with a rotating-compensator ellipsometer, caused by the addition of 0.1 nm overlayers of SiO_2 and amorphous Si on a crystalline Si substrate, as indicated. (b) As (A), but for the $\cos(4\omega t)$ and $\sin(4\omega t)$ coefficients.37

Figure 22. SHG response of oxidized Si(111) for p-polarized excitation and detection. The data exhibit C_{3v} symmetry. A peak in the oxidized-surface response occurs whenever one of the back bonds (see Figure 23) aligns nearly parallel to the excitation field.39

Figure 23. Bond directions in Si(111). Electric field is aligned parallel to 111 in the illustration.40

Figure 24. ABM fit of data shown in Figure 22.....41

Figure 25. SHG response H-terminated Si(111) for p-polarized excitation and detection.42

Figure 26. Evolution of SHG p-p data for three initially H-terminated Si(111) samples during air exposure. Red arrows in the insets mark the direction of the strain applied to the silicon crystal from the bond perspective. (a) no applied strain; (b) 0.06% external strain applied along 121; (c) 0.05% external strain applied along 10143

Figure 27. Thicknesses of the (a) oxide and (b) interface layers for an on-axis sample as determined by spectroscopic ellipsometry45

Figure 28. Evolution of the average hyperpolarizabilities for all Si bonds from the data shown in Figure 26. These values are obtained by fitting the SHG response to the function given by Equation 16. The green lines show fits to the Chapman-Richards function given in Equation 44. The specific hyperpolarizabilities are (a) up bond of the unstrained sample; (b) up bond of the sample strained along 121; (c) up bond of the sample strained along 101; (d) back bonds of the unstrained sample; (e) back bonds of the sample strained along 121; (f) back bonds of the sample strained along 10146

Figure 29. Two-step process for Oxidation of H-terminated Silicon.....47

Figure 30. (a) Evolution of SHG during air exposure of an H-terminated unstrained Si sample. (b) As (a), but for 0.015% tensile strain along 101. (c) Evolution of the average of the SHG signals at 120°, 0°, and -120° for different tensile strains.....50

Figure 31. Evolution of the average of SHG signals at azimuth angles of 120°, 0°, and 120° for different tensile strained samples.....51

Figure 32. (a) The first 80 min of SHG signals at 120°, 0°, and 120° for a sample under 0.015% tensile strain. (b) As (a), but for 600 min for a sample under 0.031% compressive strain.52

Figure 33. (a) Evolution of the average hyperpolarizabilities of the up bonds for compressed and unstrained samples and a sample under tension. The green lines are fits to an exponential function. (b) As (a), but for Si back bonds.53

Figure 34. SHG response for the first 190 min for an initially H-terminated singular Si(111) surface as a function of air exposure. No strain was applied for the first 10 min. At that time, marked by the black arrow, strain was applied in an arbitrary direction. Inset: 3D plot of the same data.55

Figure 35. (a) Evolution of p-p SHG data for a 4.6°-vicinal, initially H-terminated Si(111) sample during air exposure. (b) The first four SHG scans of the data in A, together with those at 20 and 25 min.56

Figure 36. (a, blue dots) SHG data for the first scan in Fig. 8A, together with an ABM simulation (black line). The simulation assumes that only the support bonds at the step sides in (b) are oxidized, as shown in by the red atoms in (c). The hyperpolarizabilities used in the simulation are: 2-8i, 0.3, 0.8 and 0.8 for the Si-O support bond, the Si-H bond, and the two Si-Si bonds to the terraces.58

Figure 37. (a) Evolution of SHG for an initially H-terminated P-doped Si(111) sample of carrier concentration 10^{12} cm^{-3} during air exposure. (b) As (a), but with a carrier concentration of 10^{14} cm^{-3} . (c) As (a), but with a carrier concentration of 10^{16} cm^{-3} . (d) Evolution of the average magnitudes of the three SHG peaks for each of these samples, along with that for the As-doped sample with a carrier concentration of $n = 10^{18} \text{ cm}^{-3}$60

Figure 38. Evolutions of the hyperpolarizabilities of the up and back bonds of the n-type samples as indicated. The hyperpolarizabilities were calculated in the ABM.61

Figure 39. Evolutions of the oxide thicknesses for n-type materials as measured by SE.62

Figure 40. AFM scans of boron doped Si(111) samples for 0h, 1h, and 3h of oxidation in air (a)-(c) carrier concentration $p=1.3 \times 10^{15} \text{ cm}^{-3}$ (d)-(f) carrier concentration $p =5.1 \times 10^{18} \text{ cm}^{-3}$63

Figure 41. (a) Evolution of SHG during air exposure of an H-terminated Si(111) sample with $p=3.6 \times 10^{16} \text{ cm}^{-3}$ (b) as (a) but for $p=5.1 \times 10^{18} \text{ cm}^{-3}$ 64

Figure 42. (a) Evolution of the average hyperpolarizabilities of the up bonds for boron-doped Si(111) samples with $p = 1.3 \times 10^{15}$, 3.6×10^{16} , and $5.1 \times 10^{18} \text{ cm}^{-3}$. (b) As (a), but for the Si back bonds.65

Figure 43. (a) first 40 min of Fig 2a; (b) first 40 min of Fig 2b.The green curves show the exponential fits.66

Figure 44. (a) Evolution of the azimuths of the dominant features for the unstrained on-axis sample. (b) As (c), but for the sample strained along 121. (c) As (b) but for strain along 101. (d)-(f) Results of force-field calculations showing the result of O insertion in different bonds.68

Figure 45. Evolution of the average magnitudes of the three SHG peaks for an oxidizing methoxylated Si(111) sample in air.70

Figure 46. THG signal of a Si(100) sample.70

Figure 47. Time evolution of the THG response during oxidation of H-Si(100).71

1 Introduction

One of the most important inventions of the 20th century is the transistor, invented at Bell Laboratories in 1947 by William Shockley, John Bardeen and Walter Brattain. It is the basis of modern electronics. These first transistors were made of Germanium because of its substantially high electron and hole mobility at room temperature, and that it has a relatively low surface recombination velocity so minority carriers are not rapidly extinguished. In today's microelectronics industry, transistors have many applications such as microprocessors¹, computer memories², biological/chemical sensors³⁻⁷, photovoltaics⁸⁻¹², microfluidics¹³⁻¹⁸ and micro-electromechanics^{19,20}. But in all these applications the base transistor material is Silicon not Germanium. The huge success of Silicon-based materials in electronics technology is mainly due to the realization of metal-oxide-semiconductor field-effect transistors (MOSFETs), which require a defect free Si/SiO₂ interface.

Because of the key role that this interface plays in devices, surface processes on Silicon has been extensively studied. Namely surface oxidation,^{21,22} passivation with a variety of atoms,^{23,24} interaction of H-terminated surfaces with hydrocarbons,^{25,26} photo induced reactivity,²⁷ and nanopatterning²⁸⁻³⁰ of surfaces are under investigation. Many experimental and theoretical tools have been applied to study the formation and characterization of this interface. Initial theoretical studies mostly relied on linear optical techniques such as interferometry and ellipsometry,^{31,32} which had been used to measure the thickness of oxides thicker than 200Å where a quadratic dependence for the oxide thickness is observed. In 1965 Deal and Grove interpreted these results successfully with a model that describes the evolution of oxide thicknesses for both dry and wet conditions.^{33,34} The model takes into account the pressure, diffusion of oxidant species in the ambient through the oxide, and reaction of these species at the interface.³⁵ Although the model yields accurate results for thick oxides, it fails for oxides thinner than 25nm. But as Silicon technology progressed and the thickness of SiO₂ in metal-oxide-semiconductor structures was reduced to ~1nm scales to get faster processing with reduced power, understanding the initial steps of oxidation became more important.

Different techniques such as infrared absorption spectroscopy³⁶⁻⁴¹ and Fourier transform infrared transmission spectroscopy^{42,43} provided significant information about the initial steps of oxidation under controlled conditions by measuring spectral changes in Si-H vibrations and relating them to chemical composition of the surface bonds. Chabal and coworkers³⁶ found that during thermal oxidation of Hydrogen terminated Si(111), Oxygen is incorporated into Si-Si bonds without removing surface hydrogen from the Si-H bonds. Comparing the activation energies needed for the reaction of Oxygen with Si-Si bonds and Si-H bonds they deduce a higher reaction probability for the oxidation of Si-Si. These results led to a better understanding of the initial thermal oxidation process of Silicon in controlled conditions.³⁶

Precise control of chemical processes on surfaces requires monitoring chemical reactivities along different bond directions. However conventional linear optical techniques do not provide information about the chemical kinetics along different directions. In contrast, nonlinear optical methods are suitable to provide information about the structure of bonds. But their application to real-time characterization of surface processes is not realized in its full capacity. One such tool is Second-Harmonic Generation (SHG) spectroscopy. In my thesis work, I employ SHG to measure chemical changes along different bond directions. Hence, it is possible to investigate bond-specific structural dynamics and chemical kinetics during surface reactions on Silicon. SHG experiments are performed to investigate the oxidation of strained and unstrained H-terminated Si(111) with different doping concentration in real time. These data are analyzed with the anisotropic bond-charge model (ABM) of nonlinear optics. With this methodology several problems on the initial oxidation process such as the inconsistency regarding the duration of Hydrogen passivation as well as its dependency on doping and strain will be addressed.

These studies not only improve understanding of surface chemistry at the bond level and lead to complementary information to conventional structural-characterization techniques. They also provide us with the opportunity to control in-plane surface chemistry during material growth.

1.1 Application of Second-Harmonic Generation to interface phenomena

The capability of SHG to selectively access the Si-dielectric interface has long been known. Important research in this area was conducted by a collaboration of Lucovsky, Kurz and coworkers.^{44,45} Findings include: strained Si interlayers at the Si/SiO₂ interface cause a redshift of the Si interband critical points E'_0 and E_1 during thermal oxidation,⁴⁴ vicinal Si(111) subjected to different annealing temperatures shows that SHG signal changes after annealing due to a modification of atomic bonding at the steps of the surface.⁴⁵ Further research on bonding configurations in step structures was performed by Hollering, McGilp and Vandriel and coworkers.⁴⁶⁻⁵⁰ The sensitivity of SHG to buried interfaces was also exploited to measure Angstrom-scale interface roughness in situ without removing the oxide⁵¹⁻⁵³ and to investigate the effect of strain^{54,55} at the Si/SiO₂ interface. Additionally, electric-field induced second-harmonic generation (EFISH) was used to probe charge traps at the Si/SiO₂ interface.⁵⁶⁻⁶⁰

Most of the mentioned research work utilized a macroscopic theory based on a tensor description (see section 2.3.2) to interpret their data. However, the capability to interpret SHG data in terms of atomic-scale bond parameters has been achieved only relatively recently with formulation of a microscopic theory, the ABM (see section 2.3.3). Downer and coworkers used this model to determine that during hydrogen termination of vicinal Si(100) charge redistribution from step-edges to underlying back bonds occurs, thus providing a qualitative microscopic view of step-edge chemistry.⁶¹ Ehlert et al. employed the ABM to interpret SHG data from different experimental geometries for optical fingerprinting of Si surface bonds.⁶² These are just some examples of SHG studies on the Si/SiO₂ interface to demonstrate the power of this nonlinear optical technique.

2 Theory of nonlinear optical experiments

2.1 Brief history of nonlinear optical experiments

The era of nonlinear-optical experiments begins with the invention of the first laser⁶³ (Figure 1) in 1960 when Theodore Maiman used a high-power flash lamp to photo-pump a 1cm long ruby rod to produce the first laser beam at a wavelength of 694.3nm.

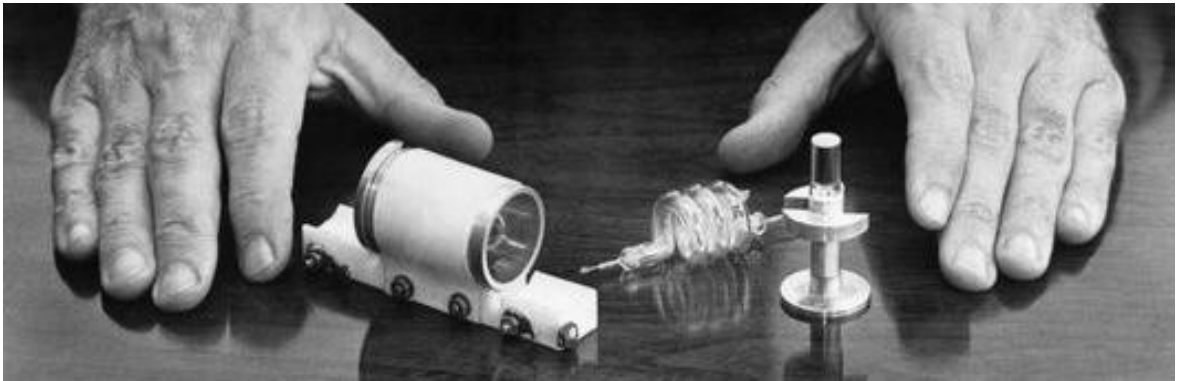


Figure 1. Maiman's laser.* This is ruby laser that emits a red beam. It was first operated at Hughes Research Laboratories in California, USA, on 16th May 1960.

Although this laser was described as "a solution looking for a problem" by some scientist at that time other more foresightful scientists found immediate use for it. One of its first application was the very first nonlinear-optical experiment, an SHG experiment, performed by Franken et al. in 1961⁶⁴ with the experimental setup shown in Figure 2.

* © Howard Hughes Research Laboratories publicity photo

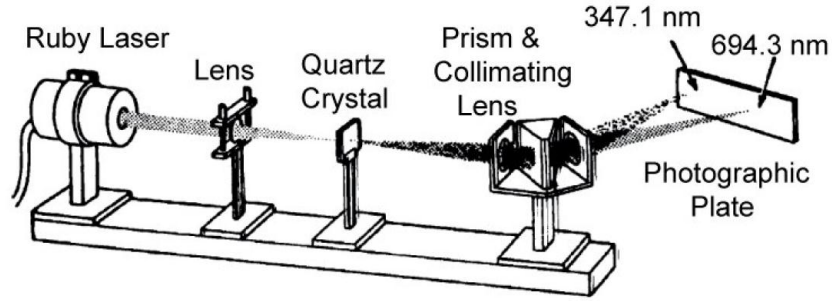


Figure 2. Experimental second-harmonic generation setup used by Franken in 1961 (from [65]).

A ruby laser with a wavelength centered at 694.2nm was used to generate the isotropic second harmonic signal in a quartz crystal at the wavelength of 347.1 nm. This pioneering work was followed by many other nonlinear optical experiments, which were based on a diversity of nonlinear-optical effects such as sum-frequency generation, multi-photon absorption, four-wave mixing, Kerr-lens mode locking and many others. The following sections describe the theory of nonlinear optical processes specifically SHG.

2.2 Light-matter interaction

When light interacts with a medium its electric field polarizes charges present in the medium creating electric dipoles. The sum of the electric dipole moments gives rise to the polarization \vec{P} of the material. In the linear case \vec{P} is given by

$$\vec{P}_L(\vec{r}, t) = \int_{-\infty}^{\infty} \chi^{(1)}(\vec{r} - \vec{r}', t - t') \cdot \vec{E}(\vec{r}', t') d\vec{r}' dt' \quad \text{Equation 1}$$

where $\vec{E}(\vec{r}', t')$ is the external driving field and $\chi^{(1)}(\vec{r} - \vec{r}', t - t')$ is the linear susceptibility. Taking the Fourier transform of Equation 1 leads to

$$\vec{P}_L(\vec{k}, \omega) = \underbrace{\chi^{(1)}(\vec{k}, \omega)}_{=\int_{-\infty}^{\infty} \chi^{(1)}(\vec{r}, t) e^{-i\vec{k}\vec{r} + i\omega t} d\vec{r} dt} \cdot \vec{E}(\vec{k}, \omega) \quad \text{Equation 2}$$

If the applied field is a strong laser field then the nonlinear case occurs and the polarization can be expanded as a power series of the electric field. If the electric field is expanded as a sum of plane waves the following power series expansion for the polarization is obtained:

$$\vec{P}(\vec{k}, \omega) = \vec{P}_L(\vec{k}, \omega) + \vec{P}^{(2)}(\vec{k}, \omega) + \vec{P}^{(3)}(\vec{k}, \omega) + \dots = \vec{P}_L(\vec{k}, \omega) + \chi^{(2)}(\vec{k} = \vec{k}_i + \vec{k}_j, \omega = \omega_i + \omega_j) \cdot \vec{E}(\vec{k}_i, \omega_i) \cdot \vec{E}(\vec{k}_j, \omega_j) + \chi^{(3)}(\vec{k} = \vec{k}_i + \vec{k}_j + \vec{k}_l, \omega = \omega_i + \omega_j + \omega_l) \cdot \vec{E}(\vec{k}_i, \omega_i) \cdot \vec{E}(\vec{k}_j, \omega_j) \cdot \vec{E}(\vec{k}_l, \omega_l) + \dots$$

Equation 3

where in general $\chi^{(2)}$ is a second rank tensor and $\chi^{(3)}$ is a third rank tensor, and $\vec{P}^{(2)}$ and $\vec{P}^{(3)}$ are the second and third-order nonlinear polarization, respectively.

2.3 Second-harmonic generation

Second-harmonic generation is associated with $\chi^{(2)}$ introduced in Equation 3. In quantum mechanical terms, SHG is the conversion of two photons of same frequency ω and energy $\hbar\omega$ to a photon of frequency 2ω energy $2\hbar\omega$ after matter-interaction in a $\chi^{(2)}$ process as shown in Figure 3.

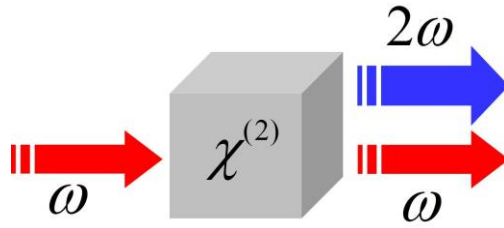


Figure 3. Illustration of frequency doubling during SHG.

The third-rank tensor $\chi^{(2)}$ contains more symmetry characteristics than the second-rank tensors of linear optics, which is why nonlinear optical spectroscopy is intrinsically more powerful for characterization of materials in comparison to linear-optical experiments. The

nature of $\chi^{(2)}$ dictates that the dipole-allowed generation of SHG signals requires an ordered arrangement of asymmetric bonds, which leads to the interface and surface sensitivity of SHG. This will be shown in the following.

2.3.1 Interface sensitivity of SHG

From Equation 3 the SHG contribution to the second order polarizability can be extracted as

$$\vec{P}(2\omega) = \chi_{ijk}^{(2)} \vec{E}(\omega) \vec{E}(\omega). \quad \text{Equation 4}$$

Say \check{z} is an inversion (parity) operation. Centrosymmetric materials are invariant under this operation meaning $\check{z}\chi_{ijk}^{(2)} = \chi_{ijk}^{(2)}$. But on vectors like \vec{P} and \vec{E} the parity operator acts as $\check{z}\vec{P} = -\vec{P}$ and $\check{z}\vec{E} = -\vec{E}$. If the operator is performed on Equation 4 we obtain

$$\check{z}\{\vec{P}(2\omega)\} = -\vec{P}(2\omega) = \check{z}\{\chi_{ijk}^{(2)} \vec{E}(\omega) \vec{E}(\omega)\} = \vec{P}(2\omega) \quad \text{Equation 5}$$

This equation is only true for $\vec{P} = 0$, hence \vec{P} is dipole-forbidden in centrosymmetric materials. Let us now consider the Si-SiO₂ system.

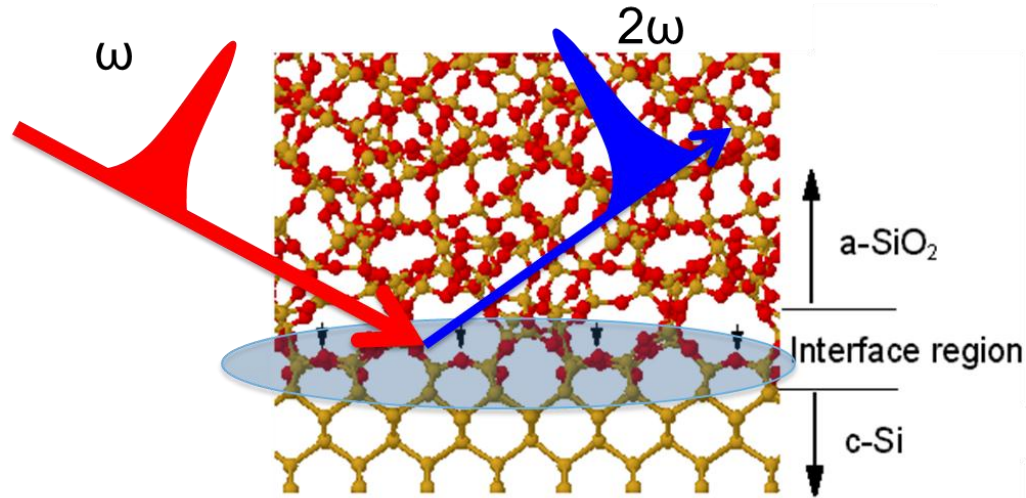


Figure 4. SHG signal arising from interface region of amorphous SiO₂ and crystalline Silicon.

In this system, crystalline Si consists of an ordered array of centrosymmetric bonds, and the overlying amorphous SiO₂ consists of asymmetric disordered bonds. According to the above description the SHG is dominated by the interface between the dipole-forbidden bulk and oxide (Figure 4). Therefore it provides a unique window into the oxidation process and is used in this thesis to study the oxidation of H-terminated Si. SHG data can be explained by two major models, which are mentioned in Section 1.1 and will be explained in more detail in the following.

2.3.2 Macroscopic tensor-based model

Equation 3 shows that the generated nonlinear field can be calculated if the nonlinear susceptibilities are known. A phenomenological approach to describe these susceptibilities and SHG from cubic and isotropic media was developed by Sipe et al.^{49,66}. This approach uses the macroscopic crystal symmetry of the medium, taking into account both bulk and surface effects, to analyze the SHG results. The starting point of this approach is Equation 4, which can be rewritten as

$$\begin{pmatrix} P_x^{(2)} \\ P_y^{(2)} \\ P_z^{(2)} \end{pmatrix} = \begin{pmatrix} \chi_{xxx}^{(2)} & \chi_{xyy}^{(2)} & \chi_{xzz}^{(2)} & \chi_{xxy}^{(2)} & \chi_{xxz}^{(2)} & \chi_{xyz}^{(2)} \\ \chi_{yxx}^{(2)} & \chi_{yyy}^{(2)} & \chi_{yzz}^{(2)} & \chi_{yyx}^{(2)} & \chi_{yyz}^{(2)} & \chi_{yyz}^{(2)} \\ \chi_{zxx}^{(2)} & \chi_{zyy}^{(2)} & \chi_{zzz}^{(2)} & \chi_{zxy}^{(2)} & \chi_{zxx}^{(2)} & \chi_{zyz}^{(2)} \end{pmatrix} \begin{pmatrix} E_x E_x \\ E_y E_y \\ E_z E_z \\ 2E_x E_y \\ 2E_x E_z \\ 2E_y E_z \end{pmatrix} \quad \text{Equation 6}$$

If we now consider a (111) oriented diamond-based structure like Si and assume that the y-axis is perpendicular to the plane of symmetry Equation 6 takes the form,

$$\begin{pmatrix} P_x^{(2)} \\ P_y^{(2)} \\ P_z^{(2)} \end{pmatrix} = \begin{pmatrix} \chi_{xxx}^{(2)} & -\chi_{xxx}^{(2)} & 0 & 0 & \chi_{xxz}^{(2)} & 0 \\ 0 & 0 & 0 & \chi_{xxz}^{(2)} & 0 & -\chi_{xxx}^{(2)} \\ \chi_{zxx}^{(2)} & \chi_{zyy}^{(2)} & \chi_{zzz}^{(2)} & 0 & 0 & 0 \end{pmatrix} \begin{pmatrix} E_x E_x \\ E_y E_y \\ E_z E_z \\ 2E_x E_y \\ 2E_x E_z \\ 2E_y E_z \end{pmatrix} \quad \text{Equation 7}$$

where tensor coefficients $\chi_{ijk}^{(2)}$ are phenomenologically determined and listed in Reference 66 for different crystal symmetries.

For a p-polarized electric field interacting with Si(111) and the p-polarized SH fields being detected a more compact form of the SHG response is

$$E_{pp}^{2\omega}(\phi) = a_0^{pp} + a_3^{pp} \cos 3\phi \quad \text{Equation 8}$$

where ϕ is the angle of rotation and a_0^{pp} , a_3^{pp} are constants that contain several of the tensor coefficients $\chi_{ijk}^{(2)}$ and account for isotropic and anisotropic contributions to the nonlinear susceptibility, respectively.

This approach has been successfully applied to explain experimental results but an extensive use of this model is limited to cubic- or diamond-based lattices, because of their relatively easy symmetry.^{51,67-70} For many years analysis of nonlinear-optical (NLO) data were limited to such tensor-based approaches, but tensors contain only symmetry information, and therefore generally provide little or no insight about processes occurring at the atomic scale.

2.3.3 Microscopic bond model[†]

The anisotropic bond model (ABM)^{71,72} of NLO bypasses standard tensor descriptions as described in the previous section by expressing NLO data in terms of a few physically meaningful atomic-scale parameters. While tensors can still be constructed if desired, the approach allows in addition fundamental mechanisms to be identified, and a greater understanding of NLO to be achieved. Like in the tensor-based description, ABM is phenomenological, but instead of listing coefficients consistent with crystal symmetry,

[†] In part published in "Measurement and control of in-plane surface chemistry during the oxidation of H-terminated (111) Si"

Bilal Gokce, Eric J. Adles, David E. Aspnes, Kenan Gundogdu
PNAS 107, 17503–17508 (2010)

parameters are derived from a one-dimensional force model for the motions of bond or free charges that result from the application of an external field. The formulation simply follows the basic physics of NLO, specifically interpreting the NLO response as the far-field radiation emitted by bond charges driven anharmonically along bond directions.

The calculation involves four steps:

1. Evaluate the local (driving) field at the charge site
2. Solve the force equation to find the resulting motion of the charge
3. Calculate the radiation resulting from the acceleration of the charge
4. Superpose the radiation from all charges

The simplifying assumption that only motion along the bond axis is relevant is made, which is equivalent to assuming that the bonds are rotationally symmetric.

The equation of motion for the motion of a charge q_j along bond unity vectors \hat{b}_j when a field $\vec{E}e^{-i\omega t}$ is applied can be described by

$$F = q_j \vec{E} \cdot \hat{b}_j e^{-i\omega t} - \kappa_1(x - x_0) - \kappa_2(x - x_0)^2 - \gamma \frac{dx}{dt} = m \frac{d^2x}{dt^2} \quad \text{Equation 9}$$

where κ_1 is the harmonic (linear) polarizability, κ_2 is the anharmonic longitudinal hyperpolarizability, x is the position of the charge, x_0 its equilibrium position and γ represents frictional losses. Equation 9 is a second order differential equation that can be solved by

$$x = x_0 + \Delta x_1 e^{-i\omega t} + \Delta x_2 e^{-i2\omega t}. \quad \text{Equation 10}$$

Using this ansatz leads to

$$\Delta x_1 = \frac{q_j}{\kappa_1 - m\omega^2 - i\gamma\omega} \vec{E} \cdot \vec{b}_j \quad \text{Equation 11}$$

and

$$\Delta x_2 = \frac{q_j \kappa_2}{\kappa_1 - 4m\omega^2 - i\gamma 2\omega} \cdot \left(\frac{q_j \vec{E} \cdot \vec{b}_j}{\kappa_1 - m\omega^2 - i\gamma\omega} \right)^2 = \frac{q_j \kappa_2}{\kappa_1 - 4m\omega^2 - i\gamma 2\omega} \Delta x_1^2$$

Equation 12

By substituting Equation 11 & Equation 12 into the expression for an induced dipole $\vec{p}_j = q_j \Delta \vec{x}_j$ we obtain

$$p_{1j} = q_j \Delta x_1 = \alpha_{1j} (\vec{b}_j \cdot \vec{E}) \quad \text{Equation 13}$$

$$p_{2j} = q_j \Delta x_2 = \alpha_{2j} (\vec{b}_j \cdot \vec{E})^2 \quad \text{Equation 14}$$

where α_{1j} is the linear polarizability and α_{2j} is the second-order nonlinear hyperpolarizability of the j^{th} bond. The polarization \vec{P} is obtained by $\vec{P} = \frac{1}{V} \sum_j \vec{p}_j$, which leads to

$$\vec{P} = \vec{P}^{(1)} + \vec{P}^{(2)} = \frac{1}{V} \sum_j \alpha_{1j} (\vec{b}_j \cdot \vec{E}) \vec{b}_j + \frac{1}{V} \sum_j \alpha_{2j} (\vec{b}_j \cdot \vec{E})^2 \vec{b}_j \quad \text{Equation 15}$$

According to the classical far-field radiation equation we obtain following dipolar contributions to SHG (or first-order nonlinearities)

$$E_{ff}^{2\omega} \propto \sum_j \alpha_j (\hat{b}_j \cdot \vec{E})^2 \hat{b}_j \quad \text{Equation 16}$$

Equation 16 provides the atomic-scale connection between the observed SHG signal and the interface parameters, which is followed in real time to extract the chemical changes that occur on a bond-specific basis.

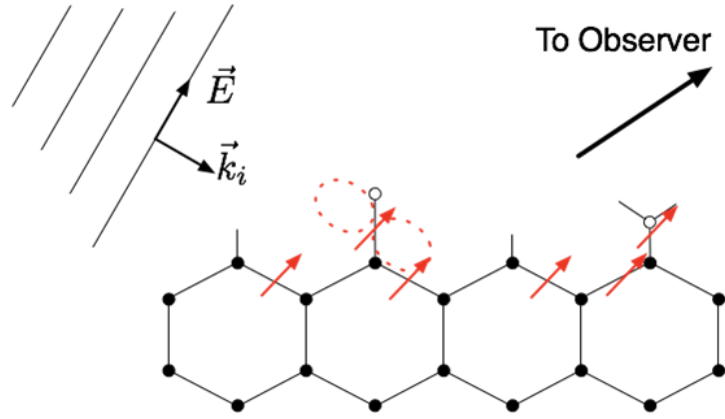


Figure 5. Illustration of charge acceleration and dipole radiation caused by an incoming electric field interacting with Silicon.

An important outcome of Equation 16 is illustrated in Figure 5: When a laser pulse is incident on a material it induces charge acceleration which leads to radiation. A critical assumption of ABM is that the acceleration of its bond charge, and hence its radiated SHG signal, is maximized when a particular asymmetric bond is aligned parallel to the driving field.

SHG as described in this section neglects the electric quadrupole from the bulk as well as the effect of an external E^{DC} -field. With these contributions included the i -th component of the polarization given by Equation 4 will take the form

$$P_i(2\omega) = \underbrace{\chi_{ijk}^{(2)} E_j(\omega) E_k(\omega)}_{dipole} + \underbrace{\chi_{ijkl}^{(3)} E_j(\omega) \nabla_k E_l(\omega)}_{quadrupole} + \underbrace{\chi_{ijkl}^{(3)} E_j(\omega) E_k(\omega) E_l^{DC}(0)}_{DC\ field} \quad \text{Equation 17}$$

However, these higher order terms are usually orders of magnitude weaker than the dipole contribution. The relative interface and bulk contributions to the overall SHG signal is being assessed in the next section.

2.3.4 Back-reflection Second-harmonic Generation of Si (111)[‡]

Here, backscattered SHG from focused Gaussian beams, and its use for obtaining information about materials and interfaces is considered. One objective is to compare the interface and bulk contributions to the overall SHG signal, necessary information when SHG is used as an interface diagnostic. Although the generation of SHG is dipole-forbidden in the bulk of inversion-symmetric materials such as Si, higher order processes such as those due to field gradients associated with highly focused beams, could possibly yield significant SHG contributions. Second, the importance of the symmetry of the unit cell in determining the nature of the observed signals is highlighted. For example, the threefold rotation symmetry of Si(111) eliminates the nodal-plane behavior of backscattered SHG that is characteristic of amorphous materials, whereas diffraction effects are the same for both.

Third, misconceptions that arise if conclusions drawn from calculations of SHG in transmission under near-phase-matched conditions are applied to backscattering are clarified. In transmission the intrinsic-anharmonic or κ_2 mechanism dominates, whereas in backscattering the κ_2 mechanism is only one of several contributions. Because of the great interest of generating “useful amounts”⁷³ of SHG in the early days of nonlinear optics, SHG from near-phase-matched transmission in isotropic and optically uniaxial material was thoroughly analyzed from a macroscopic (phenomenological) perspective^{73,74} and the interesting diffraction phenomena observed are well understood. Although Levine later showed that an anisotropic bond model provided an excellent method of categorizing second-order static susceptibilities⁷⁵, by that time the tensor approach had become embedded and Levine’s approach was not pursued further.

[‡] Published as "Back-reflection second-harmonic generation of (111) Si using focused, Gaussian beams: theory and experiment"
Bilal Gokce, Kenan Gundogdu, Eric J. Adles, David E. Aspnes
J. Korean Phys. Soc. 58, 1237 (2011)

2.3.4.1 Configuration

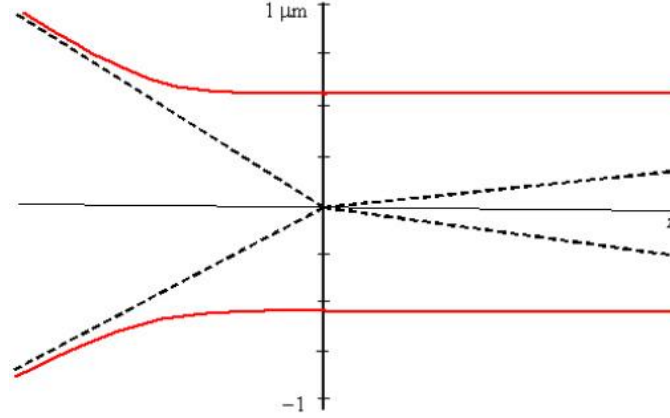


Figure 6. Schematic of the waist (red lines) of a Gaussian beam focused on an interface with a Si crystal, drawn approximately to scale for 800 nm radiation arriving from the left with an f-number of 1. The waist asymptotically approaches the dashed lines. The effective depth over which SHG is emitted from the bulk cannot be resolved on this scale.

Figure 6 is a cross-sectional view of the Gaussian pump beam near its focal point to illustrate the configuration that we investigate here. We assume that a pump beam of wavelength λ_{ext} arrives from the left with an f-number f_n and propagates in the positive z direction. We assume also that the focus is ideal, so the beam has a lateral spatial dependence that is Gaussian, specifically

$$E_{in}(\vec{r}) \sim e^{-(x^2+y^2)/\omega^2(z)} e^{ik_0 z} \quad \text{Equation 18}$$

where

$$\omega^2(z) = \omega_0^2 + \left(\frac{\lambda z}{\pi \omega_0^2} \right)^2 \quad \text{Equation 19}$$

and where $\omega_0 = (2f_n \lambda_{ext} / \pi)$ is the beam waist. Applying the values $\lambda_{ext} = 800$ nm and $f_n = 1$ that we will later use in the calculations for Si, we have $\omega_0 = 0.509$ nm and $\theta_{ext} = 26.6^\circ$ for the half-angle of the incident cone of radiation. At $z = 0$ the beam is partially reflected, but the part that penetrates has the same lateral spatial dependence and by Snell's Law, a half-angle

of 7.0° . The z dependence can be neglected for the interface contribution, since it is only one monolayer thick. However, the bulk contributes over a finite depth, which we show later is effectively determined by the integral of $e^{i(2k_0+k)z}$, where k_0 and k are the magnitudes of the wave vectors of the pump and backscattered SHG radiation, respectively. The effective penetration depth over which SHG is generated is therefore

$$d \sim \frac{1}{2k_0 + k} = \frac{\lambda_{ext}}{4\pi(n_1 + n_2)}, \quad \text{Equation 20}$$

where n_1 and n_2 are the real parts of the refractive indices of the substrate at the pump and SHG frequencies ω and 2ω , respectively. For Si we take ω and 2ω to correspond to wavelengths λ of 800 and 400 nm, respectively, in which case $\tilde{n}_1=3.69+i0.005$ and $\tilde{n}_2=6.89+i0.31$, respectively, as found in the literature⁷⁶. The material is slightly absorbing at both wavelengths, so their imaginary parts justify convergence of the Fourier integral without materially affecting the effective thickness or causing a significant reduction in intensity over the active depth. This depth d is too small to be resolved on the scale of Fig. 1. Hence, to an excellent approximation the radiation emerges from a disc of approximate aspect ratio of diameter to thickness of about 150:1. The main point here is that the lateral spreading of the pump beam in the material is completely negligible, so we can represent the field from the pump beam in the material as

$$E_{in}(\vec{r}, t) \sim E_0 e^{-(x^2+y^2)/\omega^2(z)} e^{ik_0 z} e^{-i\omega t} \quad \text{Equation 21}$$

where the coefficient E_0 is a constant. While we do the evaluation specifically for Si, the large value of ω_0/d shows that large variations in parameters are possible without affecting the basic assumptions. Ignoring local field effects, the field at the bond site j is then given by $\vec{E}_{in}(\vec{r}_j, t)$, which completes step 1.

2.3.4.2 SHG generation

The far-field SHG signal $\vec{E}_j^{ff}(\vec{r}_j, t)$ that arises from the bond j located at \vec{r}_j , as seen by an observer located at $\vec{r} = r\hat{r}$, is given by

$$\vec{E}_j^{ff}(\vec{r}_j, t) = \frac{q\omega^2}{rc^2} [\vec{l} - \hat{k}\hat{k}] \cdot \left[-i\frac{\omega n_2}{c} \Delta\vec{r}_{1j}(\hat{k} \cdot \Delta\vec{r}_{1j}) + 2\Delta\vec{r}_{2j} \right] e^{-i\vec{k} \cdot \vec{r}_j} e^{ikr - i2\omega t} \quad \text{Equation 22}$$

which is Equation 26 of Ref. 72 with the linear-response term omitted. It incorporates the solution of the force equation for the bond charge j and the calculation of its contribution to the overall radiation, i.e., the result of completing steps 2 and 3. Here, $\hat{k} = \hat{r}$, $k = 2\omega n_2/c$ is the SHG wave vector in the material, and n_2 is the real part of \tilde{n}_2 . The positions \vec{r} and \vec{r}_j are measured from a common origin in the laboratory frame. The vectors $\Delta\vec{r}_{1j}$ and $\Delta\vec{r}_{2j}$ are the linear and first-order-anharmonic parts, respectively, of the solution of the force equation that describes the motion of q under the action of $\vec{E}_{in}(\vec{r}_j, t)$. They are given by⁷²

$$\Delta\vec{r}_{1j} = \Delta r_{1j} \hat{b}_j = C_1 (\hat{b}_j \cdot \vec{E}_j) \hat{b}_j \quad \text{Equation 23}$$

$$\begin{aligned} \Delta\vec{r}_{2j} = \Delta r_{2j} \hat{b}_j = & q \left[\Delta\vec{r}_{1j} \cdot \nabla_{\vec{r}_j} (b_j \cdot \vec{E}_j) \right] \hat{b}_j \\ & - q \left[\Delta\vec{r}_{1j} \times (\nabla_{\vec{r}_j} \times \vec{E}_j) \right] \hat{b}_j - C_3 \Delta r_{1j} \Delta r_{1j} \hat{b}_j \end{aligned} \quad \text{Equation 24}$$

where

$$C_1 = \frac{q}{\kappa_1 - m\omega^2} \quad \text{Equation 25}$$

$$C_2 = \frac{q}{\kappa_1 - 4m\omega^2} \quad \text{Equation 26}$$

$$C_3 = \frac{\kappa_2}{\kappa_1 - 4m\omega^2} \quad \text{Equation 27}$$

We do not use C_2 in the above, but we define it now because it will be used later. Here, κ_1 and κ_2 are the linear (Hooke's Law) and first-order-hyperpolarizability restoring coefficients, respectively, and \hat{b}_j is the unit vector of bond j along the bond direction. For simplicity we assume that only the longitudinal motion, i.e., that along the bond direction, is relevant.

Specifically, the first term in Equation 22 is the relativistic contribution and the first, second, and third terms on the right-hand side of Equation 24 are due to spatial dispersion, magnetism, and hyperpolarizability, respectively. The electric field is

$$\vec{E}_j = \vec{E}_{in}(\vec{r}_j) = E_0(x_j, y_j)\hat{x}e^{i\vec{k}_0\vec{r}_j} = E_0\hat{x}e^{-(x_j^2+y_j^2)/\omega_0^2}e^{ik_0z_j} \quad \text{Equation 28}$$

For definitiveness it is assumed that the field is polarized in the x direction.

2.3.4.3 Evaluation for Si(111): sum over a unit cell

Now Si(111) is considered, taking \hat{z} to be the surface normal. Although there are two Si atoms per unit cell, for bookkeeping purposes we need consider only one. We take the four bond vectors to be $\hat{b}_1 = \hat{z}$, $\hat{b}_2 = \hat{b}_2(\phi) = (\sqrt{8}\hat{x}\cos(\phi) + \sqrt{8}\hat{y}\sin(\phi) - \hat{z})/3$, $\hat{b}_3 = \hat{b}_2(\phi + 120^\circ)$, and $\hat{b}_4 = \hat{b}_2(\phi + 240^\circ)$. Since $\hat{b}_1 \cdot \vec{E}_j = 0$, \hat{b}_1 does not contribute. Among them, the remaining bonds exhibit threefold rotational symmetry, which implies that the only nonvanishing terms in the various products that follow must have azimuthal dependences of $n\phi$, where $n = 0, 3, 6, \dots$. This has significant consequences on the nature of the emerging radiation, as we show below.

We now factor the sum over j into a sum over a single unit cell and a sum over unit cells. The former establishes the basic character of the emerging radiation, and the latter determines the diffraction pattern. The objective is to assess backscattering, so we write

$$\vec{k} = k(\hat{x}\theta_x + \hat{y}\theta_y - \hat{z}) = k(\hat{x}\theta\cos(\phi') + \hat{y}\theta\sin(\phi') - \hat{z}) \quad \text{Equation 29}$$

where ϕ' is the azimuth angle locating the observer. In Equation 29 we assume that θ_x and θ_y are small compared to 1 (paraxial ray approximation for the viewer, from the perspective inside the material). This is justified by noting that $k\omega_0 = 2\pi n_2\omega_0/\lambda_{ext}) = 22.1$ using the numbers given above. As we shall show, the cutoff of the Gaussian diffraction pattern occurs at $(k\omega_0\theta)^2 = 4$. Therefore, at cutoff $\theta \sim 0.090 = 5.2^\circ$, and the paraxial-beam approximation for the internal radiation is justified. After some algebra the relativistic term becomes

$$\sum_{cell} \vec{E}_{REL}(\vec{r}_j) = -i \frac{16\sqrt{2}\omega^3 q n_2 C_1^2 E_0^2 \cos^2 \phi}{81rc^3} (\sqrt{8}\theta_x \cos \phi + \sqrt{8}\theta_y \sin \phi + 1) \\ \times [\hat{x}(\sqrt{8} \cos \phi - \theta_x) + \hat{y}(\sqrt{8} \sin \phi - \theta_y) + \hat{z}\sqrt{8}(\theta_x \cos \phi + \theta_y \sin \phi)\sqrt{8}] \quad \text{Equation 30}$$

$$\rightarrow -i \frac{4\sqrt{2}\omega^3 q n_2 C_1^2 E_0^2}{27rc^3} [\hat{x} \cos 3\phi + \hat{y} \sin 3\phi + \hat{z}(\theta_x \cos 3\phi + \theta_y \sin 3\phi)] \quad \text{Equation 31}$$

The result of the full calculation is shown in Equation 30, and the reduced version, summed over the 3 contributing bonds and retaining only the Fourier components allowed by the threefold rotational symmetry, is given in Equation 31. We show Equation 30 in detail because it illustrates the importance of symmetry in the sum over the unit cell. The various ϕ dependences generate harmonics from 2ϕ to 5ϕ , and had the bonds been oriented randomly from cell to cell, as considered in Ref. 72, the result would be quite different. In that case only the even harmonics would survive, and a close inspection of Equation 30 reveals that this would lead to nodal planes. However, with a threefold rotational symmetry the nodal-plane contribution is basically nonexistent, as seen in Equation 31. Rather than present the remaining contributions to the same level of detail we simply cite the results. For the spatial-dispersion contribution we obtain

$$\sum_{cell} \vec{E}_{SD}(\vec{r}_j) = -\frac{8\sqrt{2}\omega^2 q C_1 C_2 E_0}{27rc^3} \left\{ (\hat{x}\theta_x + \hat{y}\theta_y) \left(\frac{\partial E_0}{\partial x} \cos 3\phi + \frac{\partial E_0}{\partial y} \sin 3\phi \right) \right. \\ \left. + \frac{\partial E_0}{\partial z} [(\hat{x} \cos 3\phi + \hat{y} \sin 3\phi) + \hat{z}(\theta_x \cos 3\phi + \theta_y \sin 3\phi)] \right\} \quad \text{Equation 32}$$

and for the hyperpolarizability term

$$\sum_{cell} \vec{E}_\kappa(\vec{r}_j) = -\frac{8\sqrt{2}\omega^2 q C_1^2 C_3 E_0^2}{81rc^3} [\hat{x} \cos 3\phi + \hat{y} \sin 3\phi + \hat{z}(\theta_x \cos 3\phi + \theta_y \sin 3\phi)] \quad \text{Equation 33}$$

The magnetic contribution vanishes identically, as expected since we are not considering motion perpendicular to the bond. These equations are all to be multiplied by the exponential factors in Equation 28, and the partial derivatives in Equation 32 act on these factors.

Before calculating diffraction effects, we make some comments about the relative magnitudes of the various terms. We first note that in calculating SHG power we take the absolute squares of the above expressions. Considering these individually, the relativistic and hyperpolarizability contributions have the same ϕ dependences, and upon squaring, these will be cylindrically symmetric. The θ contributions are of second order and can be ignored. However, the spatial-dispersion expression needs more careful consideration. The leading term is in principle also cylindrically symmetric, but the relative importance of the nodal-plane contribution depends on the relative magnitude of the lateral and longitudinal partial derivatives. By Equation 28 the longitudinal derivative is simply $ik_0 E_0 e^{-x^2/\omega_0^2}$ whereas the lateral derivatives have the form $-(2x/\omega_0^2)E_0 e^{-x^2/\omega_0^2}$. The maximum value of the former is obviously $k_0 E_0$. The latter expression reaches its maximum value at $x^2/\omega_0^2 = 1/2$, for which the value of the derivative is $-0.86E_0/\omega_0$.

Thus the relative magnitudes of the longitudinal and lateral derivatives reduces to evaluating $0.86/\omega_0 k_0$. This is most conveniently done by expressing both quantities in terms of the exterior wavelength λ_{ext} . For k_0 the expression is simply $k_0 = 2\pi n_1/\lambda_{ext}$. For ω_0 the calculation is more complicated. We note that the beam waist is determined by the f-number f_n of the incident beam according to $\omega_0 = 2f_n \lambda_{ext}/\pi$. Putting the two expressions together we find that the ratio of lateral to longitudinal derivatives is $0.86/(4n_1 f_n)$. Substituting the previous value for n_1 and assuming an exterior value $f_n = 1$ gives a ratio of 0.058. For the

data shown below, $f_n = 5$ and the ratio is approximately 0.012. Thus in this situation the longitudinal derivative dominates by over an order of magnitude. Given the aspect ratio of 150:1 for the contributing region, this could have been anticipated.

The main point is that for this unit-cell configuration, it is impossible to focus an external beam to the point where the lateral field gradient is large enough to make a difference. This lateral-gradient contribution is reduced further because it vanishes on-axis. In contrast, for amorphous materials where the unit-cell average is taken over all bond directions, the reverse is true⁷².

2.3.4.4 Diffraction

We now consider diffraction. With the contributions of the lateral derivatives eliminated, the calculation is standard. For the lateral integration all mechanisms give the same result:

$$\int_{-\infty}^{+\infty} dx dy e^{-2(x^2+y^2)/\omega_0^2} e^{i(2\vec{k}_0-\vec{k})\vec{r}} = \frac{\pi}{2} \omega_0^2 e^{-k^2 \omega_0^2 \theta^2 / 8} e^{i(2k_0+k)z} \quad \text{Equation 34}$$

For the longitudinal direction the hyperpolarizability contribution arises only from the interface, so no integration is required. We complete this calculation by setting $z = 0$ in Equation 34 and multiplying the result by N_s , the surface density of unit cells. For the relativistic and spatial-dispersion contributions the z integration is necessary, and the result is a factor of $iN_B/(2k_0 + k)$, where N_B is the bulk density of unit cells. Combining terms and writing the wave vectors as functions of the respective refractive indices, $\vec{E}^{ff}(\vec{r})$ becomes

$$\begin{aligned} \vec{E}^{ff}(\vec{r}) = & \frac{\pi\sqrt{2}\omega^2 q E_0^2 \omega_0^2}{81rc^2} \left[\frac{3N_B C_1}{n_1 + n_2} (C_1 n_2 + 2C_2 n_1) - 4N_S C_3 \right] \times [\hat{x} \cos 3\phi + \hat{y} \sin 3\phi \\ & + \hat{z}(\theta_x \cos 3\phi + \theta_y \sin 3\phi)] e^{-k^2 \omega_0^2 \theta^2 / 8} \end{aligned}$$

Equation 35

The first, second, and third terms in large brackets are the relativistic, spatial-dispersion, and interface-hyperpolarizability contributions, respectively. In taking the absolute square to

obtain the back-reflected intensity, it is seen that the ϕ dependence vanishes. The result is simply a Gaussian spot with a cutoff angle given internally by $k^2\omega_0^2\theta^2 = 4$.

The above expression does not take into account Fresnel reflection losses for either the pump beam or the emitted SHG radiation. Assuming normal-incidence transmission on both sides of the interface and noting that in generating SHG the incoming field is squared, the overall Fresnel efficiency is

$$\eta = \frac{8n_2}{(n_1 + 1)^2(n_2 + 1)} \quad \text{Equation 36}$$

For this application $\eta = 0.31$. Although we have seen that the paraxial-ray approximation is applicable internally, Snell's Law increases the cone angle of the emergent beam by about a factor of 7, so on the outside this approximation is no longer valid.

2.3.4.5 Comments with respect to earlier work

The analysis of the generation of SHG by near-phase-matched transmission, as done in References 74 and 73, is a much more difficult problem than SHG by backscattering, and some comments are appropriate. Under near-phase-matched conditions the propagation equations are singular or nearly singular, and their solution requires that the amplitude of the generated wave increase linearly with distance. Secondly, near-phase-matching is almost always done with optically uniaxial or biaxial materials, so crystal optics is involved. This leads to interesting diffraction patterns for the emerging SHG, and an essential vanishing of signals when the phase-mismatch Δk is smaller than 0 (see also Reference 77). However, none of these effects are possible in the backscattering geometry, where Δk is large and positive.

2.3.4.6 Conclusion

The difference in unit-cell symmetry leads to large differences in the backscattered response:

The nodal planes characteristic of amorphous material do not appear when the unit cell is tetrahedral. While tighter lateral focusing increases lateral field gradients and therefore nominally increases the spatial-dispersion contribution from the bulk, focusing is found to make little difference because spatial dispersion remains dominated by the longitudinal spatial variation of the phase term. Data obtained during oxidation (see Section 4) of an initially H-terminated Si(111) surface show that for this configuration the interface contribution is considerably larger than that of the bulk hence the bulk contribution can be neglected.

3 Experiments

3.1 Second-harmonic generation

A schematic illustrating of the SHG configuration is given in Figure 7.

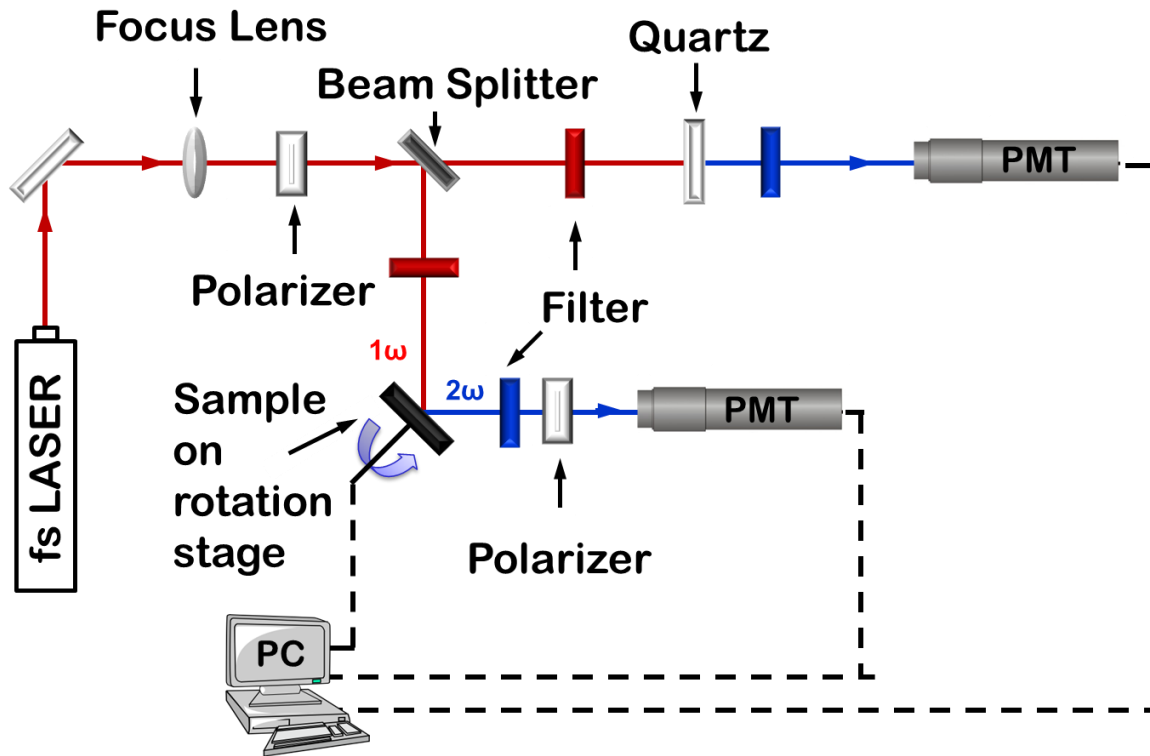


Figure 7. SHG Setup. 810 nm pulses from a Ti:sapphire oscillator are divided into two paths by the beam splitter. The sample is excited at a 45 degree angle of incidence. The SHG signal is normalized against long-term intensity fluctuations by the signal from the quartz crystal.

Experiments are performed in the reflection geometry using p- (TM-) polarized 100 fs pulses from a Kerr-lens mode locked Ti:sapphire oscillator (*Mira 900, Coherent*), which is pumped by a diode-pumped solid-state laser (*Verdi V10, Coherent*). Short pulses are used to generate high peak powers. The wavelength is centered at 806 nm and the repetition rate is 76 MHz. A Laser Spectrum Analyzer (*Rees E200 Series, Heraeus Noblelight Analytics*) is used to

monitor the pulse shape and wavelength. The pulses are focused onto the sample at a 45° angle of incidence in the laboratory frame. The power on the sample is 100-120mW while the peak intensity is $\sim 500 \text{ kW/cm}^2$. A *BG39 Schott* glass filter eliminates the fundamental in the reflected beam. A polarizer following the glass filter prevents any residual s- (TE-) polarized light from reaching the detector. Since the SHG response arises from a few monolayers at the Si-SiO₂ interface the signal is very weak and a photomultiplier tube (PMT) is needed to detect it. The PMT (*P30CWAD5A, Electron Tubes Limited*) is operating in a photon-counting mode. The sample is mounted on a *Newport PR50* rotation stage which is controlled by a *Newport ESP300* motion controller. During the experiment the sample is rotated in 1° increments over a 360° range, with each 360° scan taking 98 s.

The beam is aligned to trace a 4 mm diameter circle during rotation to ensure that laser-induced heating or charging effects are avoided. The PMT in the reference path detects an isotropic SHG signal from a Quartz crystal is used for normalization. Both PMT's are connected to a computer where the signal is processed with a self-written LabVIEW code.

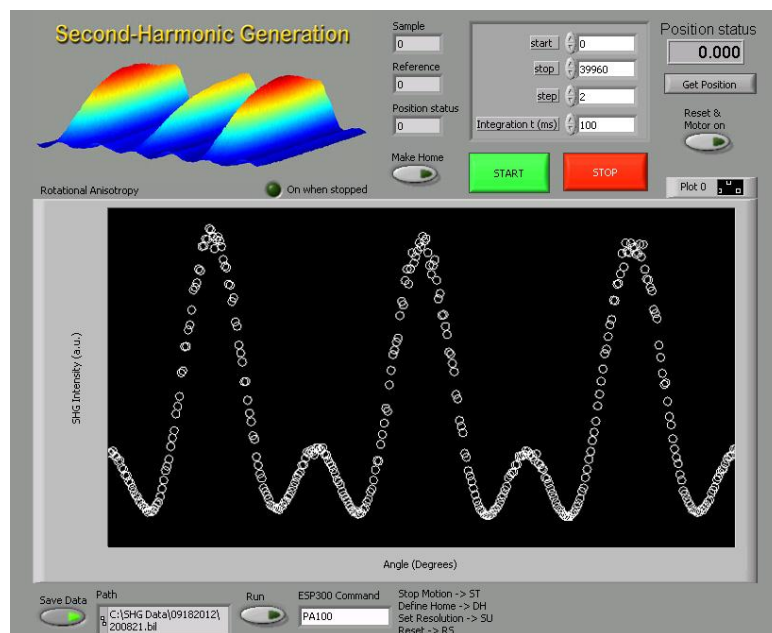


Figure 8. Screenshot of the SHG LabVIEW program user interface.

3.2 Silicon

Physical properties such as optical absorption can be explained with the electronic band structure. Therefore the band structure of Silicon is calculated using a self-written Matlab code that utilizes the Empirical Pseudopotential Method⁷⁸ (EPM), the result is shown in Figure 9.

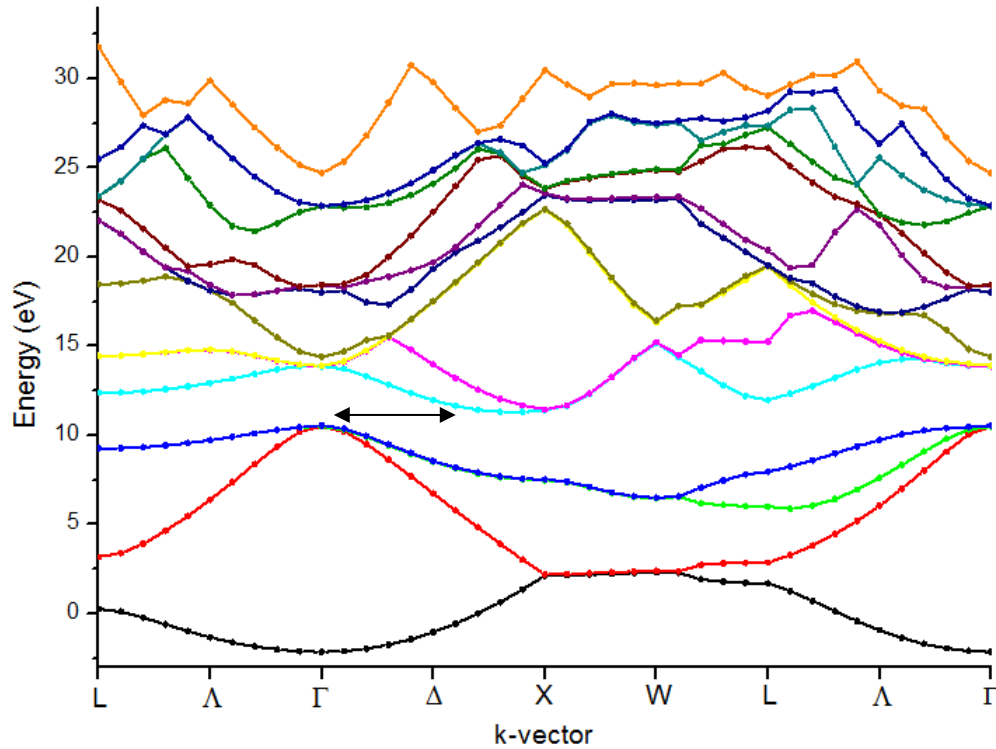


Figure 9. Band structure of Silicon. Calculated with the Empirical Pseudopotential Method. Arrow shows indirect band gap of 1.1eV.

Si is an indirect band gap material semiconductor with an optical transition energy of 1.1eV (see arrow in Figure 9). The major resonances have energies of 3.4eV 4.3eV as evident in the imaginary part of the dielectric function of Si shown in Figure 10.

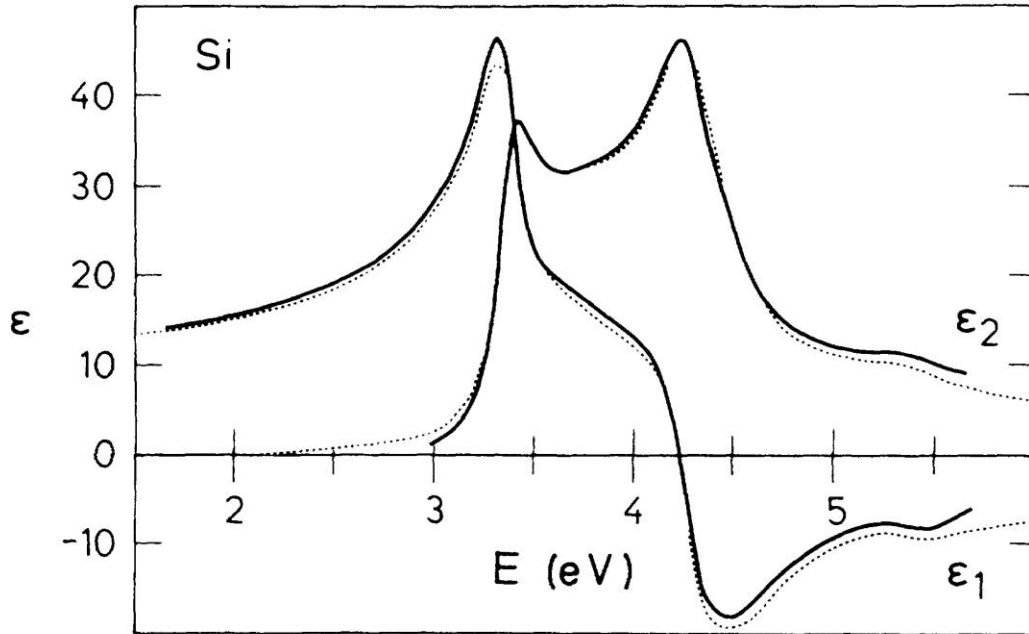


Figure 10. Calculated dielectric function of Silicon at room temperature from Ref. [79].

Since the laser beam has a photon energy of 1.54eV and the generated second-harmonic is at 3.1eV we can assume that the SHG experiments are off-resonant. The penetration depth δ_p of 806-nm light into silicon is 9.2 μm as calculated by

$$\delta_p = \frac{\lambda}{4\pi\kappa} \quad \text{Equation 37}$$

with the wavelength $\lambda=806\text{nm}$ and the imaginary part of the refractive index $\kappa=0.007^{80}$.

Most of the experiments described in this thesis were performed on Silicon in the (111) direction. A picture denoting the (111) direction in a Silicon crystal is shown in Figure 11.

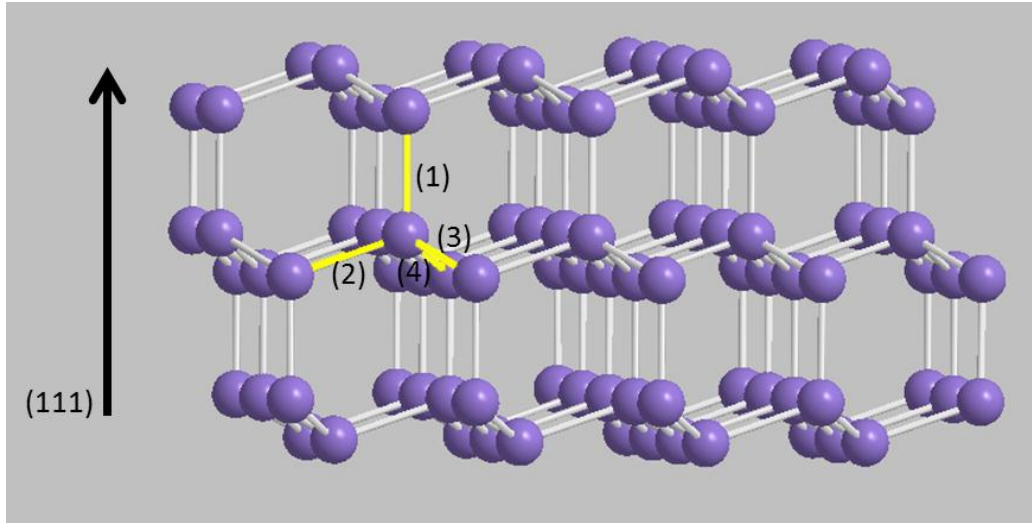


Figure 11. Silicon Crystal is shown with three distinct bond directions. The arrow denotes the (111) direction.

Also highlighted are four bonds, forming a tetrahedron, which are distinct direction for a diamond cubic structure like Si. The Si-Si bond length in the bulk is 2.3\AA and the bond angle is 109.5° .

Silicon samples used in the experiments were single side polished wafers with thicknesses between $175\mu\text{m}$ and $500\mu\text{m}$. They were supplied from 3 different vendors: Virginia Semiconductors, University Wafer, and Wafer World to ensure that the experiments were not depending on the supplier. Data were obtained on two different (111) orientations, one at $0.0 \pm 0.1^\circ$ the other at $4.6 \pm 0.1^\circ$ toward [11-2] and one (100) orientation at $0.0 \pm 0.1^\circ$ as determined by X-ray diffraction. The Doping Concentrations were verified by four-point-probe experiments.

A summary of the wafers is given in Table A.

Table A. Summary of Silicon Samples

	Orientation	Dopant	Doping Concentration
#1	$\langle 111 \rangle \pm 0.1^\circ$	Phosphorous	$3.4 \times 10^{12} \text{ cm}^{-3}$
#2	$\langle 111 \rangle \pm 0.1^\circ$	Phosphorous	$4.5 \times 10^{14} \text{ cm}^{-3}$
#3	$\langle 111 \rangle \pm 0.1^\circ$	Phosphorous	$9.1 \times 10^{14} \text{ cm}^{-3}$
#4	$\langle 111 \rangle \pm 0.1^\circ$	Phosphorous	$5.0 \times 10^{16} \text{ cm}^{-3}$
#5	$\langle 111 \rangle \pm 0.1^\circ$	Arsenic	$5.0 \times 10^{18} \text{ cm}^{-3}$
#6	$\langle 111 \rangle \pm 4.6^\circ$	Phosphorous	$4.8 \times 10^{14} \text{ cm}^{-3}$
#7	$\langle 111 \rangle \pm 0.1^\circ$	Boron	$1.3 \times 10^{15} \text{ cm}^{-3}$
#8	$\langle 111 \rangle \pm 0.1^\circ$	Boron	$3.6 \times 10^{16} \text{ cm}^{-3}$
#9	$\langle 111 \rangle \pm 0.1^\circ$	Boron	$5.1 \times 10^{18} \text{ cm}^{-3}$
#10	$\langle 100 \rangle \pm 0.1^\circ$	Boron	$7.2 \times 10^{14} \text{ cm}^{-3}$

3.3 Chemical Treatment

3.3.1 Hydrogen Termination

During Hydrogen termination native oxides on the Si surface are stripped and the top orbitals of the outmost Si atoms capped with Hydrogen as shown in Figure 12.

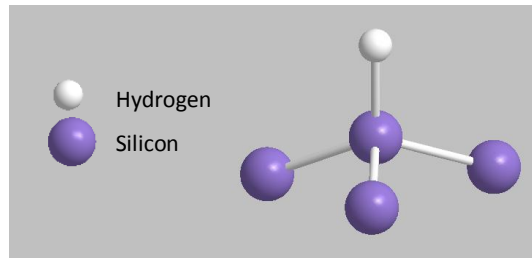


Figure 12. Illustration of Hydrogen terminated Silicon.

Hydrogen termination is achieved by chemical processing of the Si wafers. Samples are cleaned by consecutive 10-min immersions in 80°C NaOH/H₂O₂/H₂O (1:1:5) and 80°C HCl/H₂O₂/H₂O (1:1:5). The replacement of OH with H is completed by a 20 min immersion in 40% NH₄F.^{81,82} To minimize pitting the NH₄F solutions were deoxygenated prior to immersion⁸³. Measurements began approximately 60 seconds after the samples were removed from the NH₄F solution and dried with high-purity N₂. All measurements were made at room temperature (21°C ± 2°C) in ambient laboratory conditions (Humidity 50% ± 10%).

The processed surface is inspected with SHG or Atomic Force Microscopy (AFM). A typical AFM image of an H-terminated Si surface is shown in Figure 13

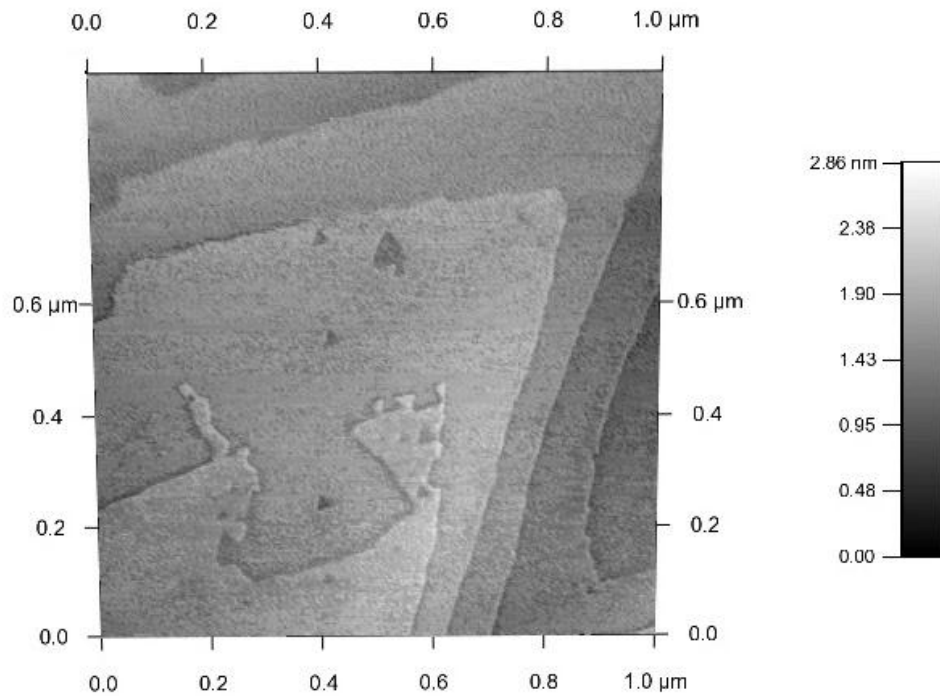


Figure 13. AFM image of H-terminated Si.

3.3.2 Methoxylation

Methoxylation of Si is the replacement of a hydroxyl (-OH) group by a methoxy (-OCH₃) group to obtain Si-OCH₃ structures as shown in Figure 14.

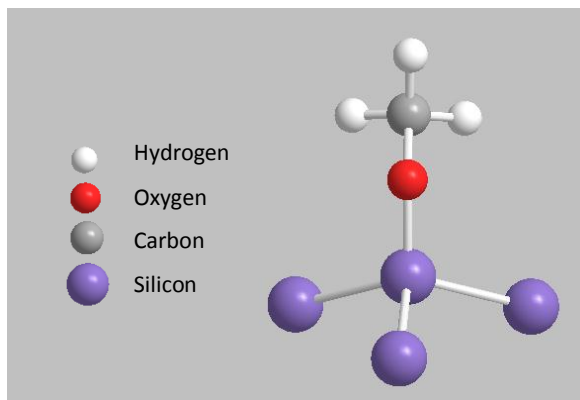


Figure 14. Illustration of methoxylated Silicon.

It is achieved by cleaning, H-termination and immersion in neat anhydrous methanol at 70°C for 12h inside a nitrogen-purged glove box. This procedure leads to the formation of oxide-free methoxy-terminated Si surfaces.^{84,85}

3.4 Application and Calculation of Strain

3.4.1 Application of Strain

In some experiments strain is applied during the oxidation process. This is accomplished by placing the front surface of the samples under tension and bending them over cylindrical mandrels of specified radii of curvature (Figure 15). This geometry also ensured that strain in the perpendicular in-surface direction was negligible.

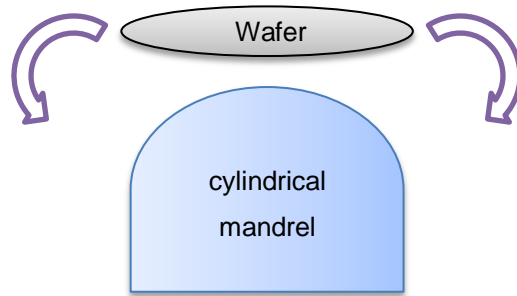


Figure 15. Application of Strain.

3.4.2 Strain detection by Reflectance Anisotropy Spectroscopy

Strain is defined as the ratio of total deformation ΔR to the initial dimension R of a material.

$$\epsilon = \frac{\Delta R}{R} \quad \text{Equation 38}$$

Strain values are determined by geometrical considerations or by Reflectance Anisotropy Spectroscopy (RAS) measurements. The RAS system used in this work is described in Ref. 86. RAS is a linear optical tool able to detect strain levels as low as 10^{-5} .⁸⁷ The measurements are based on RAS spectra similar to the ones shown in Figure 16.

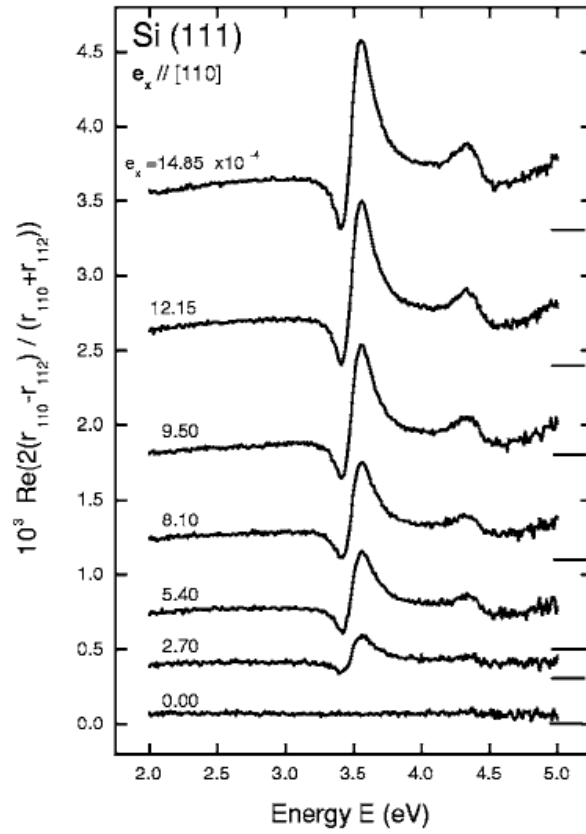


Figure 16. Spectra of reflectance anisotropy of Si(111) stripes strained along [1-10] (from Reference 87).

This Figure shows the RAS spectrum of Si(111) which displays a feature at 3.4 eV that increases in amplitude linearly with strain. For different strain values these amplitudes are extracted from Figure 16 and a linear regression is performed (Figure 17).

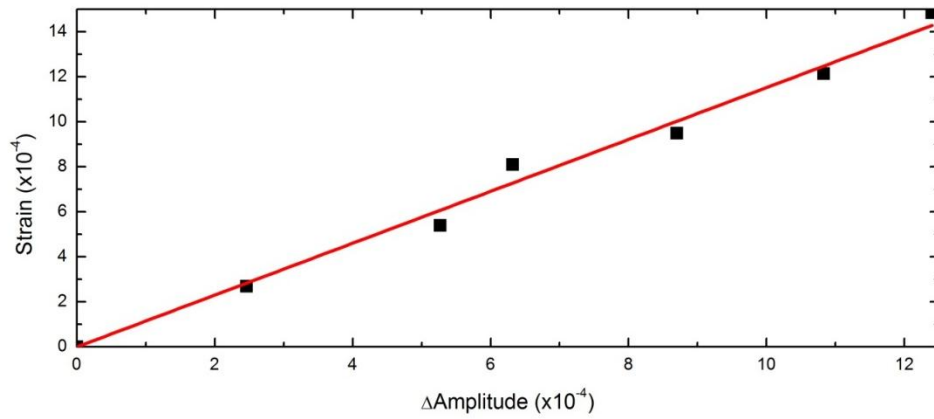


Figure 17. Amplitude and strain values extracted from Figure 16 and plotted with a linear regression (red curve).

This fit yields $S = 1.152A$ which is used to calculate the strain values S for given Amplitudes A .

A typical RAS spectrum of a strained Si(111) sample is shown in Figure 18.

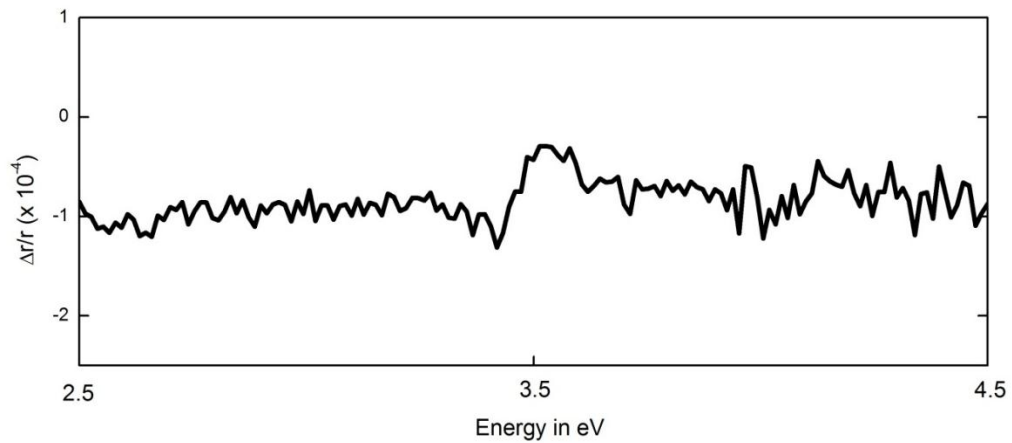


Figure 18. Typical RAS spectrum with strain applied on Si(111) sample

3.4.3 Strain calculation by geometrical considerations

Another method that is used to calculate the strain is based on the deformed focus of a reflected HeNe-Laser beam when the reflecting surface is bent over a cylindrical mandrel (Figure 19).

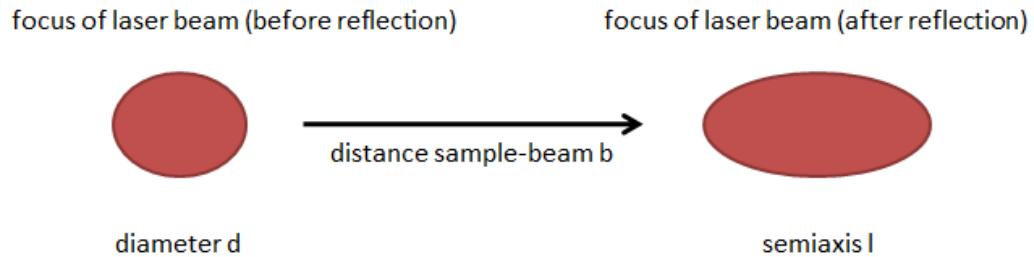


Figure 19. Deformation of laser beam focus after being reflected from a surface that is bent over a cylindrical mandrel.

The thin lens formula $1/f=1/g+1/b$, in which f is the focus, g is the distance between object and lens and b is the distance between image and lens, is put into the magnification expression $M=b/g=l/d$ where l is the height of the image and d is the height of the object. This yields to following expression for the radius of curvature of the sample

$$R_c = \frac{2bl}{d + l} \quad \text{Equation 39}$$

where b,d,l in our system are shown in Figure 19.

According to Reference 88 the strain applied to the sample is given by Equation 40.

$$\epsilon = \frac{R}{2R_c} \quad \text{Equation 40}$$

where R is the thickness of the sample.

3.5 Spectroscopic Ellipsometry

In spectroscopic ellipsometry (SE) light is reflected off a material and the change in the polarization state

$$\chi = \frac{E_p}{E_s} \quad \text{Equation 41}$$

is measured to probe the real and imaginary parts of its dielectric function and obtain information about sample properties, including morphology and chemical composition. Explicitly, ρ the ratio of the polarization states of the incident (χ_{in}) and reflected light (χ_{ref}) is determined. For optically isotropic materials ρ corresponds to the complex reflectance ratio

$$\rho = \frac{\chi_{ref}}{\chi_{in}} \triangleq \frac{r_p}{r_s} \quad \text{Equation 42}$$

where r_p is the p-polarized and r_s is the s-polarized component of the reflectance, respectively.

Each optical element in the SE setup is represented by Jones matrices which have the form of a 2x2 matrix, e.g. an isotropic sample is written as

$$J = \begin{pmatrix} r_p & 0 \\ 0 & r_s \end{pmatrix}. \quad \text{Equation 43}$$

The output field is obtained by multiplication of all Jones matrices representing the setup. Afterwards a Fourier analysis of the output field is performed in order to obtain the necessary information necessary to calculate ρ . Since ellipsometry doesn't directly measure optical properties a multi-layer model analysis is made which accounts for optical constants and thickness parameters of all individual layers.

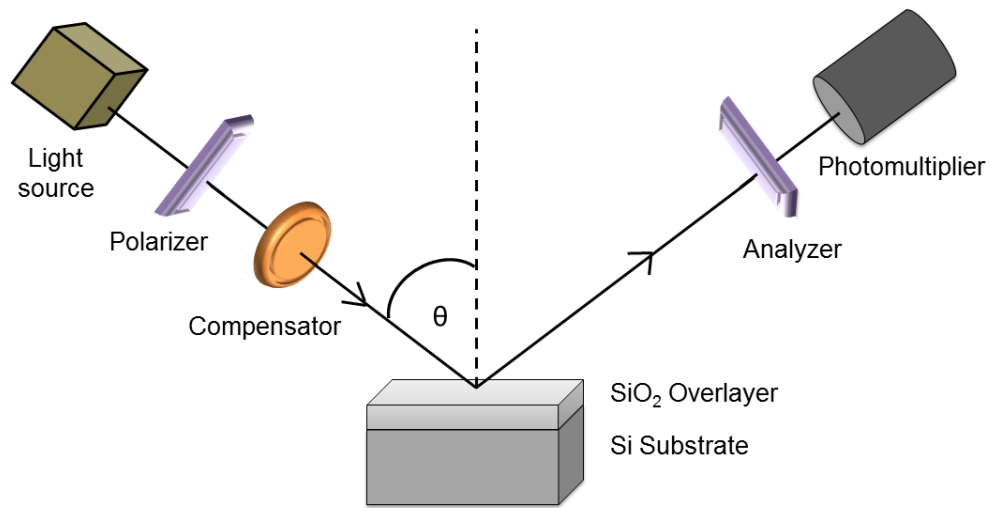


Figure 20. Spectroscopic ellipsometry setup.

In this thesis work, SE is used to characterize the SiO₂ film thickness on a Si substrate as shown in Figure 20. Data are obtained with a previously described spectroscopic ellipsometer⁸⁹ modified for rotating-compensator operation and covering a spectral range from 1.5 to 6.0 eV. Polarizer and analyzer are set at an azimuthal angle of 30° while the angle of incidence was $\theta=67.08^\circ$. The calculated spectral dependences of the changes expected in the C₂, S₂, C₄, and S₄ coefficients of the $\cos(2\omega t)$, $\sin(2\omega t)$, $\cos(4\omega t)$, and $\sin(4\omega t)$ harmonics, respectively, of the detected intensity are shown in Figure 21a and Figure 21b for 0.1 nm thick overlayers of SiO₂ and amorphous Si.

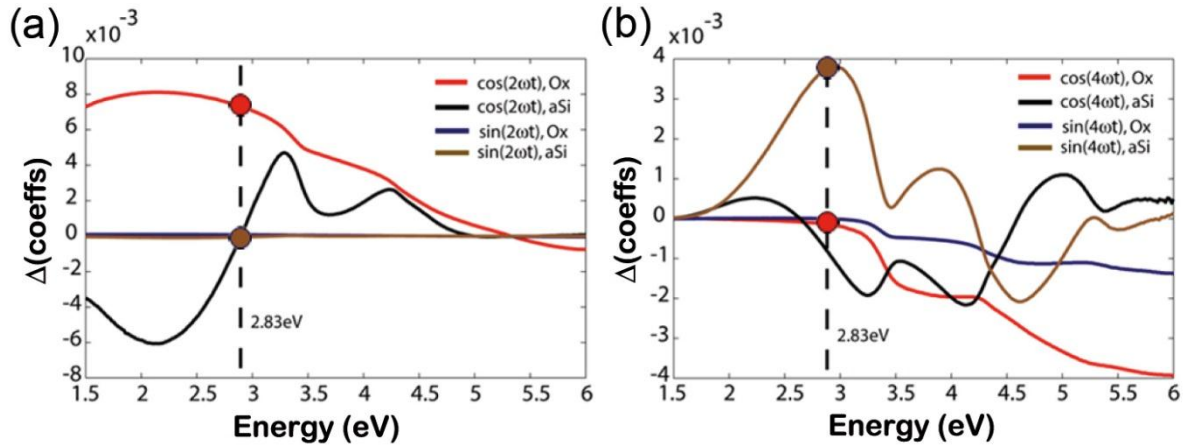


Figure 21. (a) Calculated changes from 1.5 to 6.0 eV expected in the $\cos(2\omega t)$ and $\sin(2\omega t)$ coefficients of the intensity measured with a rotating-compensator ellipsometer, caused by the addition of 0.1 nm overlayers of SiO₂ and amorphous Si on a crystalline Si substrate, as indicated. (b) As (A), but for the $\cos(4\omega t)$ and $\sin(4\omega t)$ coefficients.

At 2.83 eV these changes are specifically $\Delta C_2 = +0.00743$ and -0.00093 for SiO₂ and amorphous Si, respectively, as indicated by the red and brown dots, respectively. The changes ΔS_2 are negligible. At the same energy the changes ΔS_4 are 0.00366 and -0.00001 for SiO₂ and amorphous Si, respectively, as indicated by similar dots. Hence at 2.83 eV the C_2 contribution originates primarily from SiO₂, while that for S_4 primarily from amorphous Si. This provides the opportunity to assess how the SiO₂ overlayer and disordered interface layer evolve with oxidation, assuming that the respective dielectric responses can be modeled by SiO₂ and amorphous Si. The assumption for SiO₂ should be good to a high degree of accuracy. That for the interface could be debated, since the dielectric response for the disordered Si at the Si–SiO₂ interface will probably be somewhat different. However, we believe that this is a good first approximation.⁹⁰ If anything, it is likely to underestimate the actual interface thickness.

3.6 Atomic Force Microscopy

AFM images were obtained with an Asylum Research 3D MFP probe (Santa Barbara, CA), operated in the AC non-contact mode. Experiments were performed in air. Further specifications for this instrument can be found online at <http://www.asylumresearch.com/>.

4 Results and Discussion

In this part a description of how the SHG data are analyzed using the ABM is given before showing and discussing experimental results on the effect of strain, step structures and doping on the oxidation of H-Si(111).

4.1 SHG Data Analysis

The typical SHG response of a oxidized singular Si(111) for p-polarized excitation and detection is shown in Figure 22.

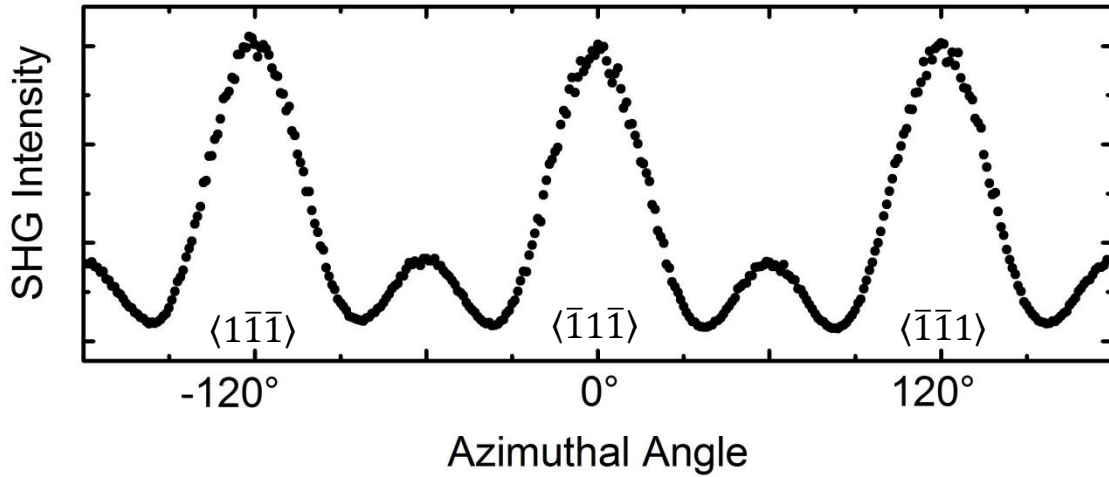


Figure 22. SHG response of oxidized Si(111) for p-polarized excitation and detection. The data exhibit C_{3v} symmetry. A peak in the oxidized-surface response occurs whenever one of the $\langle 1\bar{1}\bar{1} \rangle$, $\langle \bar{1}1\bar{1} \rangle$ and $\langle \bar{1}\bar{1}1 \rangle$ back bonds (see Figure 23) aligns nearly parallel to the excitation field.

The response exhibits threefold symmetry (C_{3v}). According to the bond model (section 2.3.3), the major features in the oxidized-surface data occur when one of the $\langle 1\bar{1}\bar{1} \rangle$, $\langle \bar{1}1\bar{1} \rangle$ and $\langle \bar{1}\bar{1}1 \rangle$ back bonds is nearly parallel to the driving field (Figure 23). For p-polarized light incident at 45° , this minimum angle is 8.4° and occurs when the bond is in the plane of incidence pointing approximately toward the illumination direction.

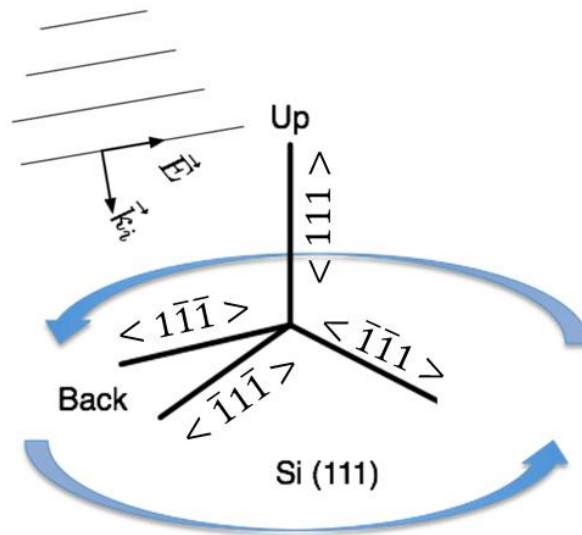


Figure 23. Bond directions in Si(111). Electric field is aligned parallel to $\langle \bar{1}\bar{1}\bar{1} \rangle$ in the illustration.

Since the response of the $\langle 111 \rangle$ (up) bonds is isotropic they contribute to the signal as an offset. The three smaller peaks in Figure 22 are rectified versions of negative field extrema, which are made positive because the intensity, being proportional to the square of the field, is positive definite. The Matlab code shown in Appendix A uses the ABM formalism to generate a fitting function (Appendix B) with five parameters representing the four bond hyperpolarizabilities described by Equation 16 and a constant offset. An example of such a fit is shown in Figure 24.

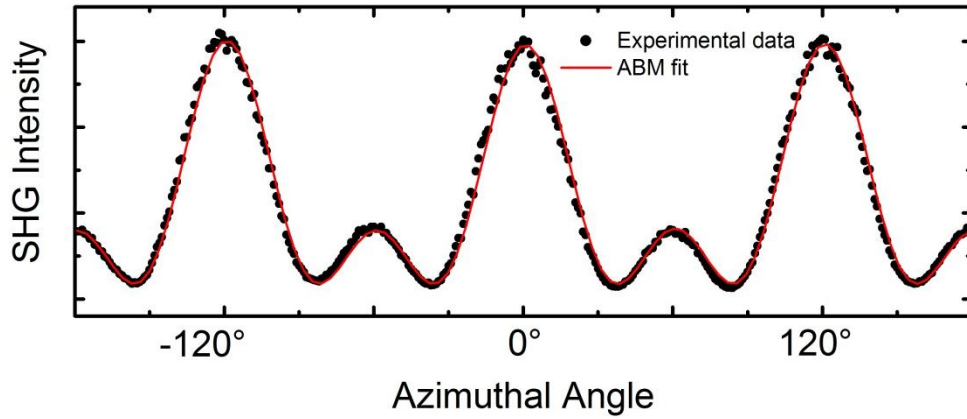


Figure 24. ABM fit of data shown in Figure 22.

The adjusted R^2 value for this fit, which would be equal to 1 for a perfect fit, is 0.99207. The fitting parameters are given in the following table:

Table B. Fitting parameters yielding the best fit for data in Figure 24

	Value	Standard Error
$\alpha_1\langle 111 \rangle$	491.77346	1.97586
$\alpha_2\langle \bar{1}\bar{1}\bar{1} \rangle$	-26.52067	0.12002
$\alpha_3\langle \bar{1}\bar{1}\bar{1} \rangle$	-26.55810	0.11991
$\alpha_4\langle \bar{1}\bar{1}\bar{1} \rangle$	-26.74041	0.11940
offset	26.07145	1.01688

As expected the hyperpolarizabilities of the back bonds are identical within one standard deviation while the hyperpolarizability of the up bond is significantly higher having an opposite sign indicating its opposite direction.

A good way to test the accuracy of the ABM is to see if it can reasonably describe the structure in a Si-SiO₂ interface that contains steps. This test is executed in section 4.3.

The starting point of nearly all oxidation experiments described in this thesis work is the singular H-Si(111) surface which is H-terminated as described in section 3.3.1. The SHG response of H-Si(111) is depicted in Figure 25.

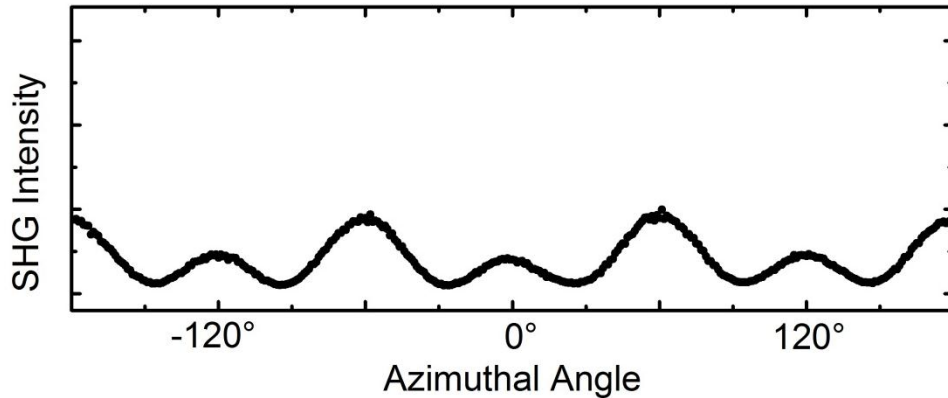


Figure 25. SHG response H-terminated Si(111) for p-polarized excitation and detection.

For the H-terminated surface the major peaks are much smaller and the major and minor peaks are reversed, reflecting partly the reduced electronegativity of H and a relative enhancement of the contribution of the (isotropic) top bond in this case.

4.2 Effect of Strain on Oxidation of H-Si(111)[§]

Bond-specific effects of strain on the oxidation kinetics of H-Si(111) are investigated in the following.

[§] In part published in "Effect of strain on bond-specific reaction kinetics during the oxidation of Hydrogen terminated (111) Si"

Bilal Gokce, David E. Aspnes, Kenan Gundogdu
Applied Physics Letters 98, 121912 (2011)

4.2.1 Dependence on direction of strain

Figure 26 shows the results of consecutive SHG scans for three H-terminated singular Si(111) samples of type #3 from Table A during air oxidation.

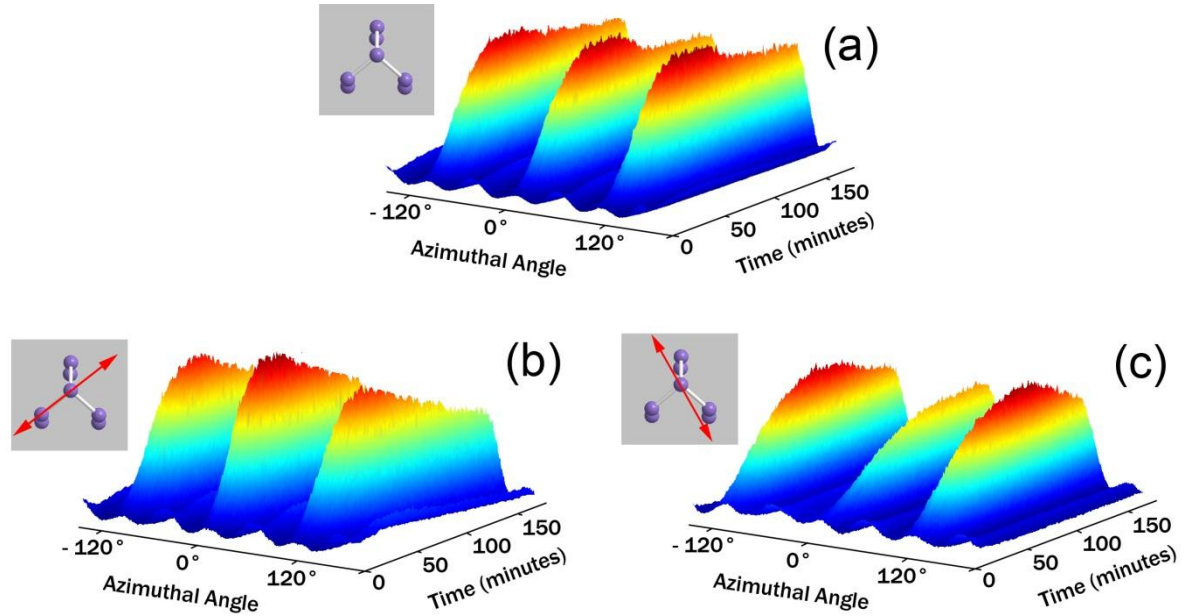


Figure 26. Evolution of SHG p-p data for three initially H-terminated Si(111) samples during air exposure. Red arrows in the insets mark the direction of the strain applied to the silicon crystal from the bond perspective. (a) no applied strain; (b) 0.06% external strain applied along $\langle \bar{1}2\bar{1} \rangle$; (c) 0.05% external strain applied along $\langle \bar{1}01 \rangle$.

In all cases the signal starts with the SHG response of the H-terminated surface, as shown in Figure 25. It then increases to a maximum before decreasing to the reference level for the oxidized surface, shown as the black points in Figure 22. However, the SHG responses differ significantly during oxidation. Panel (a) shows data for the unstrained sample. Here, the three major peaks evolve similarly during oxidation, indicating that oxidation is proceeding isotropically on the macroscopic scale. Panels (b) and (c) display similar data obtained for strain applied along the $\langle \bar{1}2\bar{1} \rangle$ and $\langle \bar{1}01 \rangle$ directions, respectively. The peaks evolve at different rate for the strained samples.

For the data of Panel (b) in Figure 26, the $\langle\bar{1}2\bar{1}\rangle$ direction of the applied 0.08 % strain aligns most closely with the direction of the $\langle\bar{1}1\bar{1}\rangle$ bond. The angles between the strain direction and the bonds are specifically 19.5° for the $\langle\bar{1}1\bar{1}\rangle$ bond and 61.9° for the other two. This is consistent with the increased reactivity of the $\langle\bar{1}1\bar{1}\rangle$ bond as seen in the data, indicating that strain has the greatest influence on the chemical reactivity of bonds in the strain direction, which is probably not surprising. The alternative case is shown in Panel (c). Here, the 0.05% strain along $\langle\bar{1}01\rangle$ is perpendicular to the $\langle\bar{1}1\bar{1}\rangle$ bonds and therefore mainly affects the chemical reactivity in the other two bond directions. In this case the middle peak rises more slowly. For both experiments involving strain, the SHG response starts and ends with C_{3v} symmetry, indicating that the states of the initial and final surfaces are alike. The observed differences are therefore due to the chemical processes involved while oxidation is occurring. To relate the SHG data to the oxidation of bonds in the different directions, we first need to establish the evolution of oxide thickness. To do this we performed SE measurements under the ambient conditions as described above. Data for an unstrained surface are shown in Figure 27a and Figure 27b. These were obtained at a photon energy of 2.83 eV to maximize the distinction between oxide and interfacial layer, as discussed in connection with Figure 21. To avoid artifacts due to hydrocarbon contamination, the surfaces were rinsed in methanol prior to each datum. We repeated the measurements for strained surfaces at different times after H termination. Surprisingly, the oxide and interface thicknesses for all surfaces are the same to within the experimental uncertainty of $\pm 1 \text{ \AA}$. Thus the average SiO_2 overlayer thickness evolves at essentially the same rate for strained and unstrained surfaces, regardless of the relatively complicated kinetics observed with SHG.

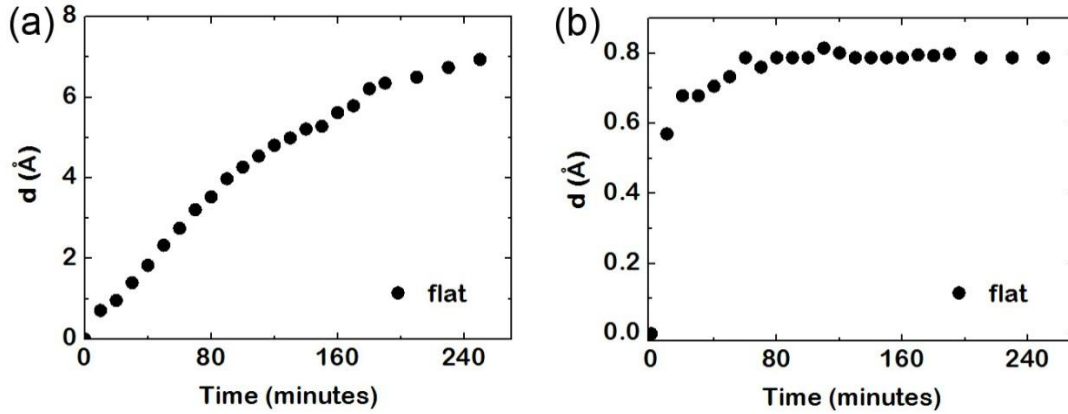


Figure 27. Thicknesses of the (a) oxide and (b) interface layers for an on-axis sample as determined by spectroscopic ellipsometry .

However, we can gain further information from the comparison. For all cases the maximum SHG amplitudes are observed when the oxide layer is 2 to 4 Å thick, which corresponds to oxidation of the first Si bilayer. When the SHG data reach their equilibrium levels the thickness is about 6 Å. For later times C_{3v} symmetry recovers, but the oxide thickness continues to increase until saturating near 8 Å. Therefore, for the strain levels involved in these experiments, the observed anisotropic behavior of the oxidation kinetics is related to the oxidation of the topmost Si bilayer. The anisotropy does not persist for lower layers.

We obtain the hyperpolarizabilities of the four bond directions by the method described in section 4.1. The results for the evolution of these hyperpolarizabilities are given in Figure 28. Since oxidation occurs at different times for bonds in a given direction, at any given time these are average polarizabilities. Nevertheless, the picture yields good insight into the reaction kinetics of individual bonds.

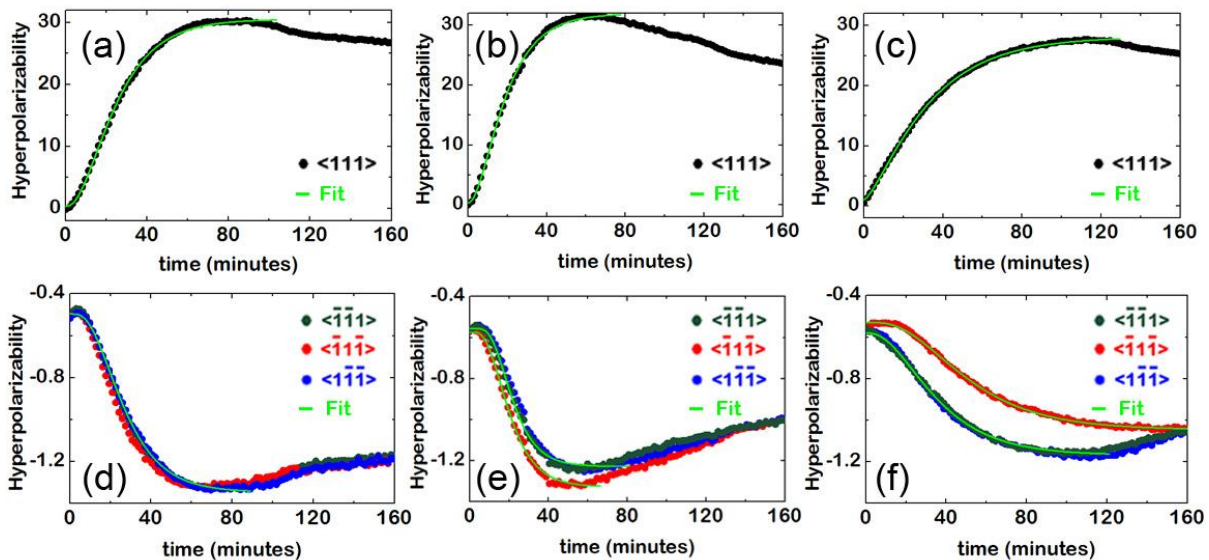


Figure 28. Evolution of the average hyperpolarizabilities for all Si bonds from the data shown in Figure 26. These values are obtained by fitting the SHG response to the function given by Equation 16. The green lines show fits to the Chapman-Richards function given in Equation 44. The specific hyperpolarizabilities are (a) up bond of the unstrained sample; (b) up bond of the sample strained along $\langle \bar{1}2\bar{1} \rangle$; (c) up bond of the sample strained along $\langle \bar{1}01 \rangle$; (d) back bonds of the unstrained sample; (e) back bonds of the sample strained along $\langle \bar{1}2\bar{1} \rangle$; (f) back bonds of the sample strained along $\langle \bar{1}01 \rangle$.

The relationship between the chemical nature of a bond and its hyperpolarizability is subtle. When a bond undergoes a chemical change, the electronic potential is primarily altered at the bond, but the potentials of neighboring bonds are affected as well. However, some general conclusions can still be drawn. Considering the rise of the SHG response for the first 60 to 80 min for all samples, as shown in Figure 28, the striking results are (1) the significant change in the average hyperpolarizability of the up bonds and (2) the near balance between this hyperpolarizability and those of the back bonds. The magnitudes of all four hyperpolarizabilities increase with oxidation, which is exactly what we expect from the differences in electronegativity between O and H. The near balance can be understood as a consequence of chemical induction. The capping atoms draw charge from the capped Si atom in proportion to their electronegativities, thus also modifying the hyperpolarizabilities of the back bonds in proportion to the adsorbate electronegativities. Because the contribution of the

up bonds is independent of sample azimuth, it would be difficult to extract it directly from the raw SHG data of Figure 26 without modeling.

During the rising part of the SHG signal some back bonds also oxidize. That is, the increase in SHG signal and the average hyperpolarizabilities shown in Figure 28 are not due solely to oxidation of the up bonds. We gather this from two observations. First, the SE data indicate that the oxide thickness is about 2 to 4 Å at 80 min. This exceeds the value expected for a single monolayer of OH capping the top silicon atoms. Second, the hyperpolarizabilities of the back bonds of the strained surfaces are themselves anisotropic, which suggests differences in their average chemical nature. However, this effect is much smaller than that seen in the up bonds. The back-bond hyperpolarizabilities only increase by a factor of 3, in comparison with to the 60-fold increase in that of the up bonds. The reason for this smaller change is evident when we consider the nature of the bonding. The oxidation of the top bonds creates an obviously asymmetric potential. However, oxidation of the back bonds replaces a Si-Si bond with a Si-O-Si combination, which is somewhat symmetric. If both Si atoms were same and the bond linear, then the SHG response of the configuration would vanish. However, the terminating Si atoms differ from each other by their electronegativities. Because O insertion forms an Si-O-Si bridge and introduces microscopic strain, the Si bonds involved will be deflected from the directions that they would have in the ideal crystal lattice. Therefore, the excitation field is expected to better align with only one of Si-O bonds in an Si-O-Si bridge, increasing the SHG efficiency. Nevertheless the net hyperpolarizabilities of the oxidized back bonds can never become as strong as that of up bonds.

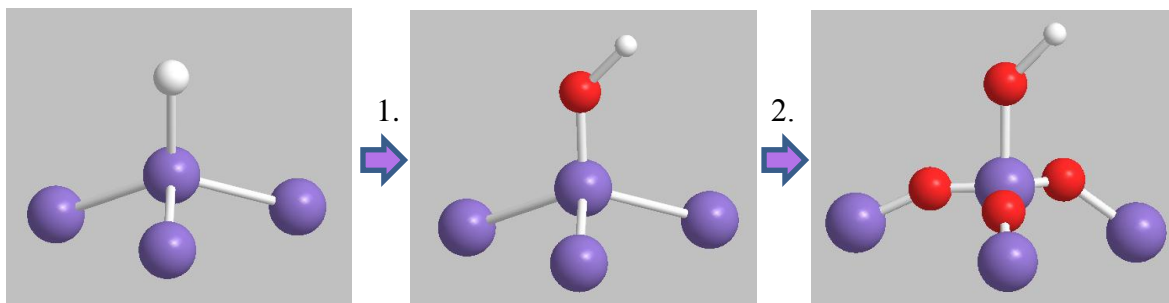


Figure 29. Two-step process for Oxidation of H-terminated Silicon.

Consistent with previous IR studies³, the above discussion indicates a two-step oxidation process described in Ref⁹¹. The first step involved in the oxidation of H-terminated Silicon is the replacement of the Hydrogen of the up-bonds by Hydroxyl-groups as shown in Figure 29. The following second step consists of Oxygen insertion into the back bonds. To lowest order we would expect uniaxial strain to affect the reactivity of back bonds more than that of the up bonds.

To obtain a more quantitative understanding of reaction rates for the different bond directions, we attempted to fit the hyperpolarizabilities to exponential functions. However, simple exponentials gave very poor fits, with large errors. Thus it is clear that the reaction rates of the up and back bonds are coupled. While oxidation may initiate with the up bonds, back-bond oxidation begins soon afterward and introduces local strain, which further complicates oxidation kinetics. Therefore, the rate parameters are not constant, but change as oxidation proceeds. Processes like this are well known in biology, where intertwined factors contribute to population changes. Such processes can be described by the Chapman-Richards equation¹⁵

$$W(t) = U(1 - e^{-ct})^n + y_0 \quad \text{Equation 44}$$

The results of fitting to this equation are the green curves of Figure 28. The fit during the initial part of the data up through the maxima, is excellent. The resulting parameters are summarized in Table C.

Table C. Parameters yielding the best fits of Equation 44 to the data of Figure 28

	U	C	n	y₀
Figure 28a $\langle 111 \rangle$	30.151	0.063	2.561	0.370
Figure 28b $\langle 111 \rangle$	27.129	0.036	1.452	1.040
Figure 28c $\langle 111 \rangle$	31.592	0.077	2.215	0.366
Figure 28d $\langle \bar{1}\bar{1}\bar{1} \rangle, \langle \bar{1}\bar{1}\bar{1} \rangle, \langle 111 \rangle$	-0.849	0.072	4.055	-0.496
Figure 28e $\langle \bar{1}\bar{1}\bar{1} \rangle, \langle 111 \rangle$	-0.516	0.037	3.950	-0.529
Figure 28e $\langle \bar{1}\bar{1}\bar{1} \rangle$	-0.587	0.046	2.873	-0.580
Figure 28f $\langle \bar{1}\bar{1}\bar{1} \rangle$	-0.671	0.116	8.001	-0.556
Figure 28f $\langle \bar{1}\bar{1}\bar{1} \rangle, \langle 111 \rangle$	-0.752	0.106	5.144	-0.573

The actual relationship between these parameters and the chemical reactivities of particular bonds requires theoretical calculations of the hyperpolarizabilities of expected configurations. This can certainly be done, but is beyond the scope of this thesis. However, the results emphasize the complexity of these chemical processes at the bond level, and also show that these complexities can be revealed by a combination of nonlinear optics and bond-charge modeling.

4.2.2 Dependence on magnitude of strain

Figure 30a and Figure 30b show SHG data for samples of type #1 from Table A that are unstrained and under 0.015% tensile strain, respectively.

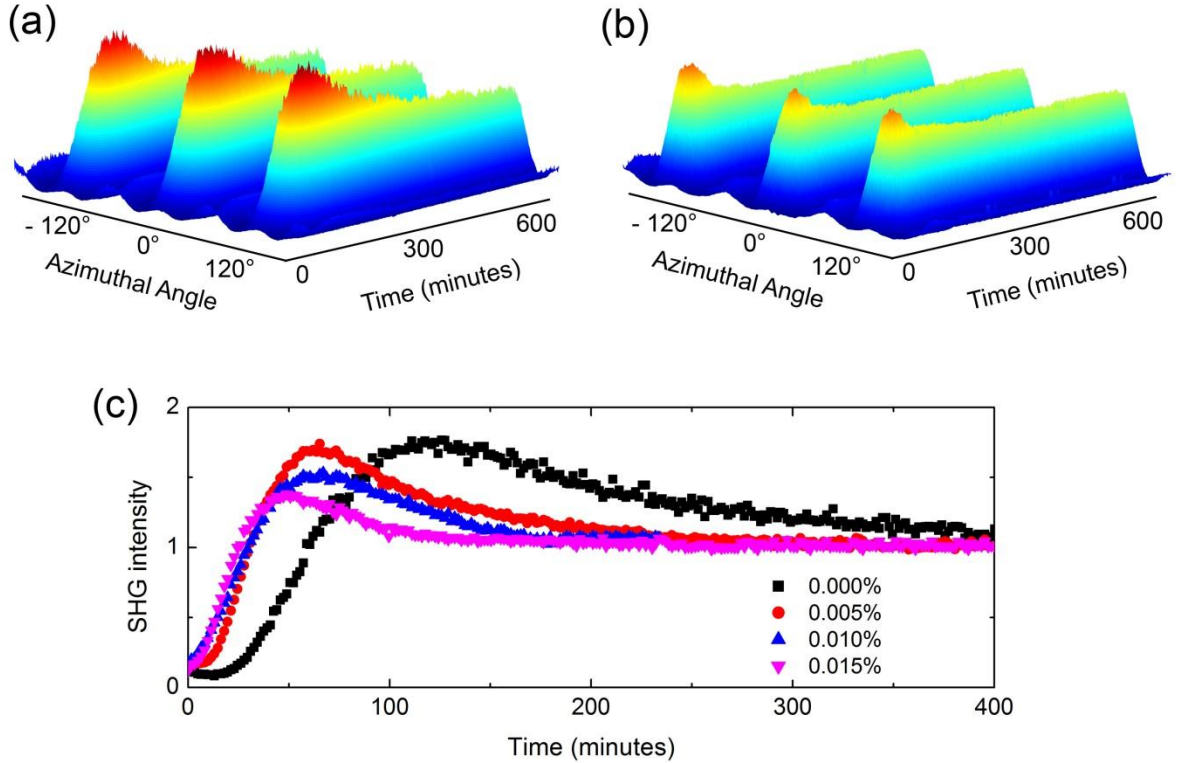


Figure 30. (a) Evolution of SHG during air exposure of an H-terminated unstrained Si sample. (b) As (a), but for 0.015% tensile strain along $\langle\bar{1}01\rangle$. (c) Evolution of the average of the SHG signals at 120°, 0°, and -120° for different tensile strains.

Both sets of data are normalized to the level reached at 600 minutes, where the SHG response essentially no longer evolves. As discussed previously, the three major peaks at 120°, 0°, and -120° correspond to the near alignment of one of the three back bonds to the direction of the excitation field within the material. As oxidation proceeds, these peaks increase due to the increasing average asymmetry of the surface bonds. Figure 30c summarizes these results by showing the average response at these azimuth angles for 0%,

0.005%, 0.010% and 0.015% tensile strains. The evolution is clearly affected by the magnitude of strain. For the unstrained sample, we observe a small decrease in the SHG response for a 20-minute incubation period, then an increase to a maximum at 121 min. For the strained samples the incubation period is reduced significantly, and lower peak values are reached at earlier times.

4.2.3 Dependence on type of strain

We now consider compression and compare it with tension. Figure 31 displays the evolution of a 0° peak during air oxidation for samples of type #1 from Table A under 0.015% tensile and 0.031% compressive strain, along with reference data for unstrained material. The differences are striking. Compression results in a higher peak value reached at a later time.

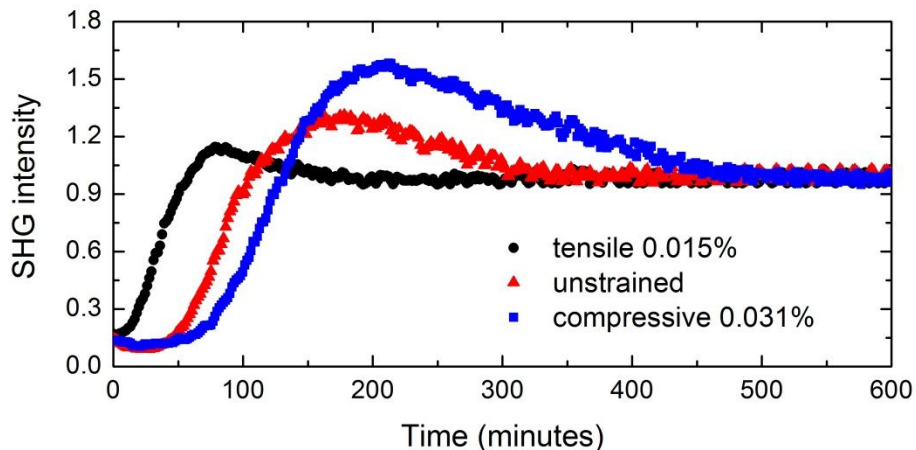


Figure 31. Evolution of the average of SHG signals at azimuth angles of 120° , 0° , and 120° for different tensile strained samples.

These observations lead directly to the conclusion that tensile and compressive strains facilitate and inhibit, respectively, not only the oxidation of back bonds but also the oxidation of the up bond. As discussed previously, Si oxidation proceeds in two steps.⁹¹ The first step results in a large increase in asymmetry of both up and back bonds, directly for the up bonds owing to the larger electronegativity of O relative to H, and indirectly for the back bonds by

chemical induction. The oxidation of the back bonds reduces their contribution in particular, because inserting O in a back bond results in a pair of bonds oriented in approximately opposite directions and hence a partial cancellation of the SHG signal. By the durations of the incubation periods and the values of the peaks, the data therefore show that tensile strain enhances oxidation, while compressive strain has the opposite effect.

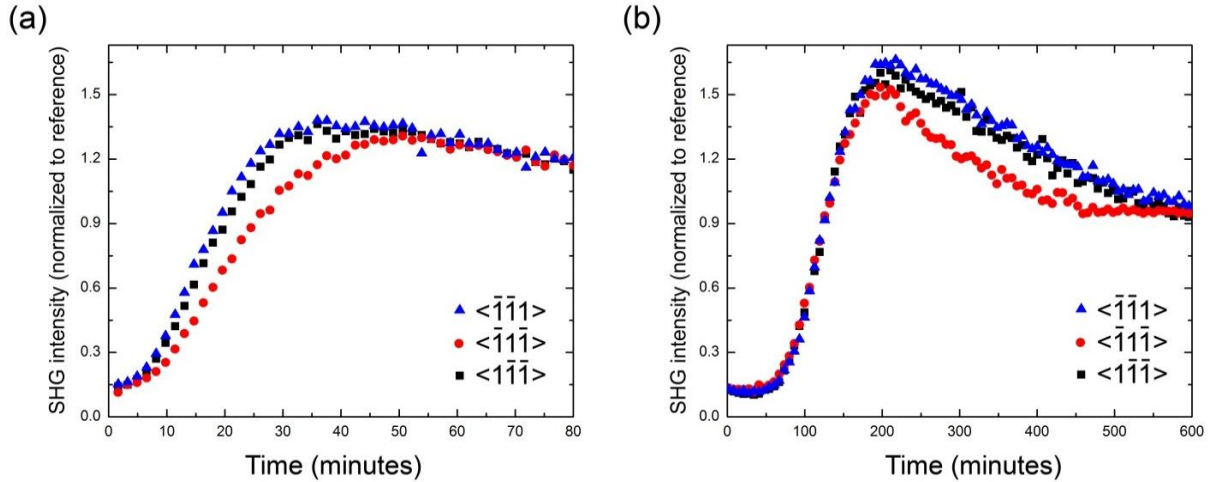


Figure 32. (a) The first 80 min of SHG signals at 120° , 0° , and 120° for a sample under 0.015% tensile strain. (b) As (a), but for 600 min for a sample under 0.031% compressive strain.

We next investigate oxidation rates for the individual bond directions. In tensile stress, back bonds that are better aligned with tensile stress oxidize faster. This is illustrated in Figure 32a, which shows the rise of the three major peaks for a sample under $\langle \bar{1}01 \rangle$ tension. This is perpendicular to the $\langle \bar{1}\bar{1}\bar{1} \rangle$ bonds, and the leading part of the data shows that the $\langle \bar{1}\bar{1}\bar{1} \rangle$ and $\langle 1\bar{1}\bar{1} \rangle$ bonds indeed oxidize more rapidly. The compressive equivalent is illustrated in Figure 32b. From the trailing part of the data we see that the $\langle \bar{1}\bar{1}\bar{1} \rangle$ and $\langle 1\bar{1}\bar{1} \rangle$ bonds oxidize more slowly. Compression therefore has the opposite effect, but is consistent with, and provides additional support for, the two-step oxidation model.

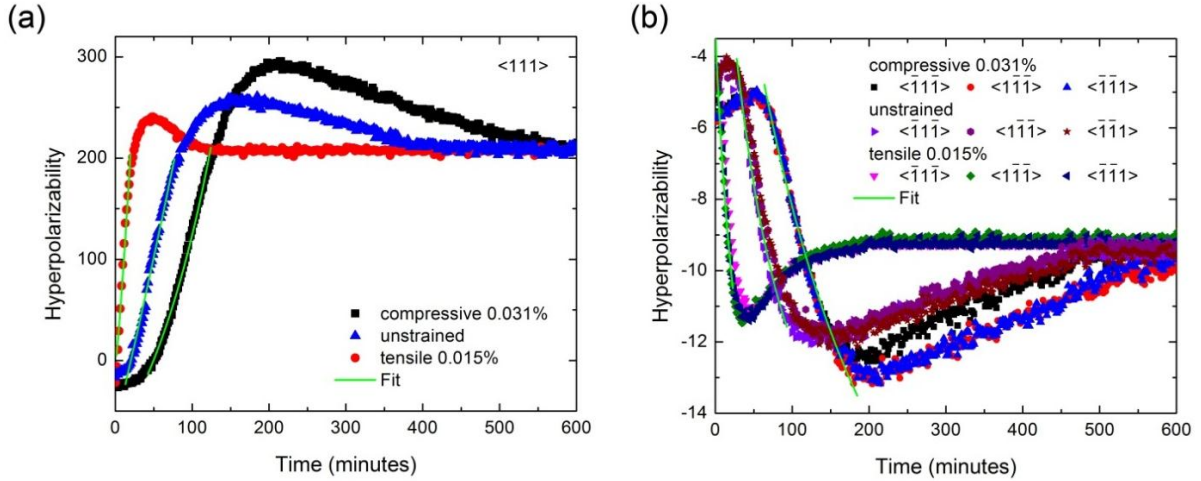


Figure 33. (a) Evolution of the average hyperpolarizabilities of the up bonds for compressed and unstrained samples and a sample under tension. The green lines are fits to an exponential function. (b) As (a), but for Si back bonds.

Further insight is obtained by examining the individual hyperpolarizabilities, which we obtain from Equation 16. Figure 33a and Figure 33b display the time evolution of the hyperpolarizabilities for the up and back bonds, respectively, with the results for the back bonds broken down into the different bonding directions. These data must be interpreted with some care, because all bonds are linked to a certain extent by chemical induction. Nevertheless, from their respective time dependences some general conclusions can be drawn. The overall time dependences are best represented by the Chapman-Richards function, which is difficult to interpret. However, if the initial incubation period is ignored, an exponential describes the leading edges with good accuracy. We show exponential fits on the figures, and summarize the results in Table D. Although the time constant of the initial rise is about 71 min for all 3 data sets in Figure 31, Table D shows that major differences occur for the up and partially aligned back bonds. The time constant for the $\langle 1\bar{1}\bar{1} \rangle$ back-bond ranges from 26 min in tension to 142 min in compression. The up bond shows a similar although smaller dependence on strain. This is in contrast to the results for the unstrained sample, which exhibit the same time constant for both bonds. Clearly, strain not only

significantly modifies the chemical reactivity of bonds during oxidation, but also discriminates among bond directions.

Table D. Parameters yielding the best fits of exponential functions to the data of Fig. 4.

	rise time τ [min]		
	Unstrained	tensile	compressive
up bond $\langle 111 \rangle$	61	43	100
back bond $\langle 1\bar{1}\bar{1} \rangle$	61	26	142

We consider next why these changes occur. The interesting aspect is that the effects seen here are approximately linear in the strain, as seen for example by the dependences of the changes in time constants relative to the unstrained constants in Table D. That is, they depend on the sign of the strain, and not simply on its magnitude. Thus we look for a mechanism that exhibits this characteristic. The obvious one is a transfer of charge between the back and up bonds as a result of the geometric distortion caused by strain. A straightforward calculation shows that the 120° bond angle between the two back bonds that are nearly aligned with the strain, as seen from above, decreases by 0.062° with 0.031% compression. We would therefore expect some charge transfer to occur from these bonds to the up bond. From the increase in incubation period in compression, the result is an H-Si bond that is less susceptible to attack. Analogous effects should occur for the back bonds. Since charge transfer is expected to be linear in bond angle, the main characteristics of the data are explained.

4.2.4 Real-Time Control of Surface Chemistry

We now investigate the possibility of using strain to manipulate oxidation kinetics in real time. Figure 34 shows data for an on-axis (111) surface similar to those shown above.

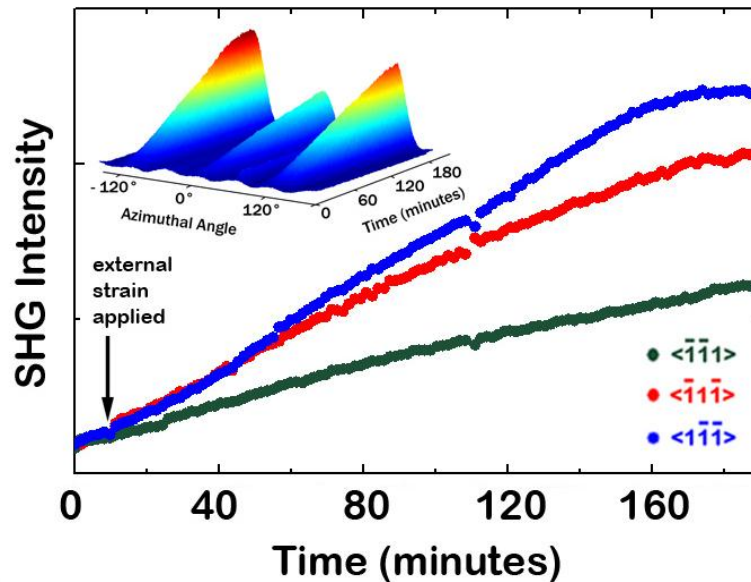


Figure 34. SHG response for the first 190 min for an initially H-terminated singular Si(111) surface as a function of air exposure. No strain was applied for the first 10 min. At that time, marked by the black arrow, strain was applied in an arbitrary direction. Inset: 3D plot of the same data.

For the first 10 min no strain is applied to the sample. During this interval the SHG evolution is consistent with C_{3v} symmetry. At 10 min we applied strain along an arbitrary direction. C_{3v} symmetry is immediately broken, with peaks corresponding to different bond directions now oxidizing at different rates. As with the previous experiments, the SHG response eventually develops C_{3v} symmetry, as expected for an on-axis sample. These data occur at a substantially later time and consequently are not shown in the figure. This result clearly shows the capability of real time manipulation of the oxidation kinetics.

4.3 Effect of Steps on Oxidation of H-Si(111)**

The data in section 4.2 show that strain plays a significant role in the oxidation kinetics of H-terminated Si(111) surfaces. Since steps can also modify oxidation kinetics, we need to investigate step effects as well. Consequently, we performed control experiments on samples of type #6 from Table A. These surfaces consist of two distinct regions: steps and terraces. The terraces have the local structure of the on-axis samples. The steps have a dangling bond in the $\langle 11\bar{1} \rangle$ direction and a support bond along $\langle \bar{1}\bar{1}\bar{1} \rangle$.

Real-time SHG data for one of these vicinal samples are shown in Figure 35.

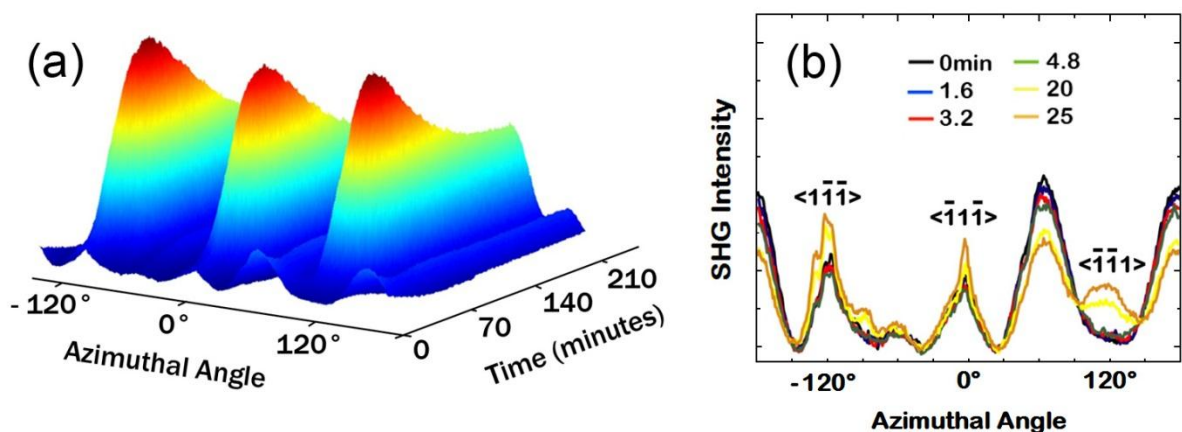


Figure 35. (a) Evolution of p-p SHG data for a 4.6°-vicinal, initially H-terminated Si(111) sample during air exposure. (b) The first four SHG scans of the data in A, together with those at 20 and 25 min.

Six features are apparent. Three grow to approximately the same amplitude, then decay. However, the oxidation kinetics is significantly different from that of strained or unstrained on-axis samples. The early oxidation dynamics is highlighted in Figure 35b, which shows the

** Published in "Measurement and control of in-plane surface chemistry during the oxidation of H-terminated (111) Si"

Bilal Gokce, Eric J. Adles, David E. Aspnes, Kenan Gundogdu
PNAS 107, 17503–17508 (2010)

SHG scans for the first 5 min together with those at 20 and 25 min. For the first 20 min we see little activity, and at the earliest times the $\langle\bar{1}\bar{1}1\rangle$ feature is missing. After 25 min the amplitudes of the major features increase at a faster rate, and all reach their maximum values approximately 75 min into oxidation.

The differences between on-axis and vicinal surfaces allow us to draw two conclusions. First, the anisotropic oxidation that we observe for the on-axis samples is not due to inadvertent arrays of steps on the surface. Second, oxidation of vicinal samples shows a strong dependence on steps and therefore exhibits significantly different dynamics with respect to strained and unstrained on-axis surfaces.

The role of steps in the oxidation kinetics of Si surfaces has been the subject of debate. Some reports suggest that oxidation does not initiate at step sides.⁹² However, FTIR data indicate that steps facilitate oxidation.⁹³ The data elucidate the crucial role of steps. In Figure 36a we show the results of an ABM simulation of the SHG first scan of Figure 35b, where the unoxidized step is shown in Figure 36b and the oxidized step in Figure 36c.

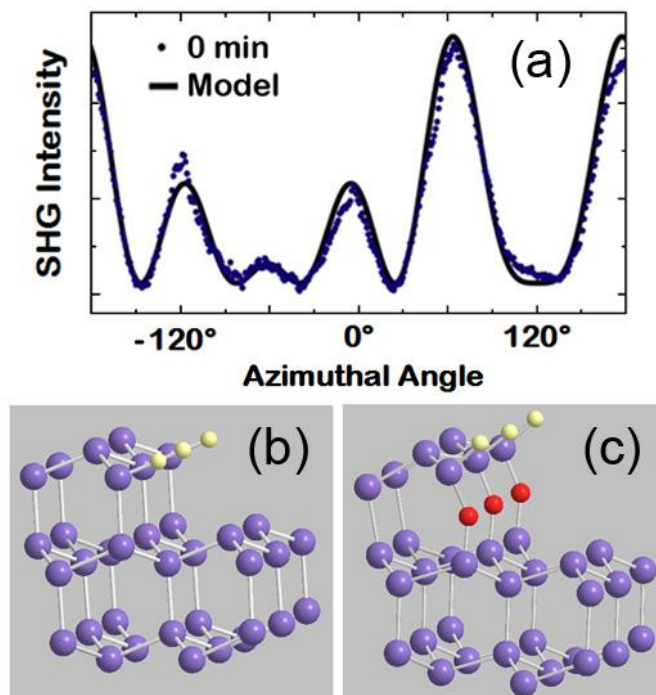


Figure 36. (a, blue dots) SHG data for the first scan in Fig. 8A, together with an ABM simulation (black line). The simulation assumes that only the support bonds at the step sides in (b) are oxidized, as shown in by the red atoms in (c). The hyperpolarizabilities used in the simulation are: 2-Si, 0.3, 0.8 and 0.8 for the Si-O support bond, the Si-H bond, and the two Si-Si bonds to the terraces.

The model assumes that the $\langle 111 \rangle$ support bonds at the sides of the step oxidize first. In this case the SHG signal arises from one Si-H step bond and two Si-Si* back bonds, where Si* represents a Si atom bonded to O. Oxidation of the support bonds actually reduces the asymmetry at the Si-H dangling bond, as discussed above, and increases the asymmetry of the Si-Si* bonds. The model successfully reproduces the data, supporting the conclusion that for vicinal orientations oxidation indeed starts at the support bonds of the steps, and in fact proceeds fast enough to have gone to completion by the time the first scan could be started. At later times oxidation of terrace bonds dominates the SHG response. But with reaction kinetics dominated by steps, we could not observe any differences in the oxidation kinetics of strained and unstrained vicinal samples.

4.4 Effect of Doping on Oxidation of H-Si(111)

The effect of doping on oxidation at elevated temperatures has been characterized by SE^{94,95} surface differential reflectance spectroscopy (SDR)⁹⁶, Auger electron spectroscopy (AES)⁹⁷, and X-ray photoelectron spectroscopy (XPS)⁹⁸, all of which probe oxide thickness. However none of these studies provide an atomic-level understanding of doping on surface chemistry. We try to establish such an understanding in this section.

4.4.1 n-type Surfaces^{††}

The experiments in the previous sections have shown that the bond-specific oxidation kinetics depend also on the carrier concentration of the Si sample. This dependency is summarized in Figure 37a, b, and c where data for differently n-type doped samples (#1,2,4,5 in Table A) are shown. All are normalized to the level where the SHG responses reach equilibrium. Where present, the three major peaks correspond to the alignment of one of the three back bonds in the direction of the exciting field.

^{††} In part published in "Bond-specific reaction kinetics during the oxidation of (111) Si: Effect of n-type doping"

Bilal Gokce, David E. Aspnes, Gerald Lucovsky, Kenan Gundogdu
Applied Physics Letters 98, 021904 (2011)

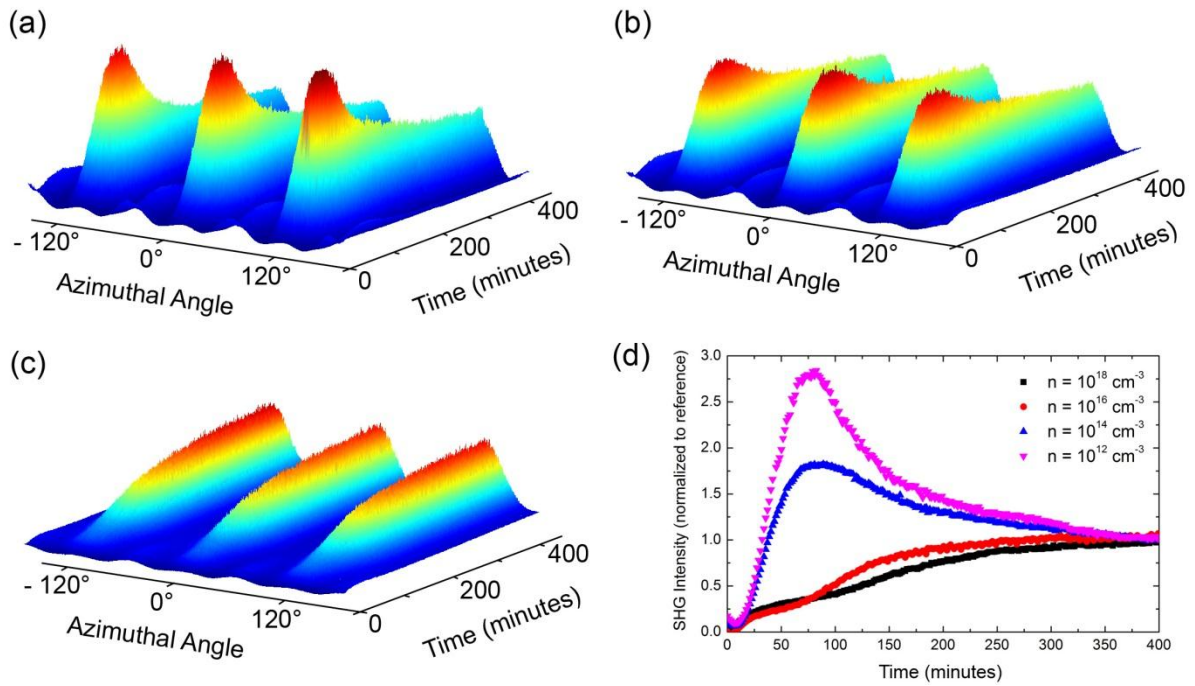


Figure 37. (a) Evolution of SHG for an initially H-terminated P-doped Si(111) sample of carrier concentration 10^{12} cm^{-3} during air exposure. (b) As (a), but with a carrier concentration of 10^{14} cm^{-3} . (c) As (a), but with a carrier concentration of 10^{16} cm^{-3} . (d) Evolution of the average magnitudes of the three SHG peaks for each of these samples, along with that for the As-doped sample with a carrier concentration of $n = 10^{18} \text{ cm}^{-3}$.

As expected, the overall effect of oxidation is to increase the SHG signal, a consequence of the facts that the electronegativity of O is higher than that of H, and the SHG contribution of the relevant Si-Si bonds is negligible. The evolution clearly depends significantly on carrier concentration. For reduced carrier concentrations the SHG intensity initially increases then decreases to the equilibrium level, whereas for high doping levels the SHG intensity increases monotonically. This striking dependence on carrier concentration is even more evident in Figure 37d, which shows the average evolution of the peaks for all four samples, including that of the As-doped sample for which $n = 10^{18} \text{ cm}^{-3}$. To relate these differences to the chemical kinetics of the bonds, we determined the respective hyperpolarizabilities by

fitting the data to the predictions of the ABM⁷². The hyperpolarizability results are summarized in Figure 38.

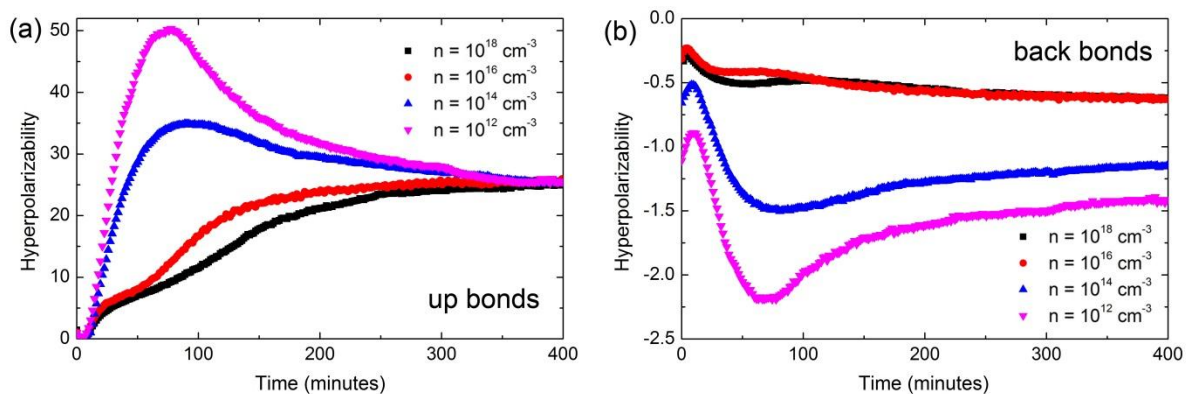


Figure 38. Evolutions of the hyperpolarizabilities of the up and back bonds of the n-type samples as indicated. The hyperpolarizabilities were calculated in the ABM.

The effect of chemistry on hyperpolarizabilities in general can be understood as follows. Generation of SHG by a bond requires that the bond be asymmetric. While an Si-H bond is obviously asymmetric, it is less obvious that terminating an up bond with H generates contributions from the Si-Si back bonds as well. The reason is chemical induction. The greater electronegativity of H removes charge from the Si atom to which it is bonded, making the back bonds asymmetric as well. Thus the SHG contribution of the back bonds tends to track that of the up bond. If the top H is now replaced by O, as for example by replacing the H with OH, the greater electronegativity of O results in greater asymmetries and hence stronger signals for both up and back bonds. This type of response is clearly evident in Figure 38 for the more lightly doped samples.

With this background, the striking difference between the samples with different doping densities can now be explained. For lightly doped samples oxidation proceeds by replacing the H with OH, as discussed above. But for heavily doped structures the reactivity of the back bonds increases and oxidation of both types of bonds occurs at similar rates. Thus the sequential increase and decrease in SHG responses seen for the relatively lightly doped

samples becomes a monotonic change. The fact that essentially the same behavior is seen for both P and As doping shows that the effect is due to carrier concentration, not type of dopant. Possible complications include bulk-quadrupole and electric-field-induced-second-harmonic (EFISH) effects⁹⁹ as stated in section 2.3.3. However, any contribution from the bulk will be constant during oxidation and hence, even if present, can be neglected. The EFISH contribution is isotropic, and is only a factor at high carrier concentrations. We investigated EFISH for the heavily As-doped sample by measuring the SHG response with the sample in a N₂-pressured glove box. For the H terminated surface it is almost zero. For the oxidized surface it increases the signal by about 15%. For the low-doped samples it is insignificant under all conditions. Thus the hyperpolarizabilities provide an accurate representation of the oxidation chemistry of the different bonds.

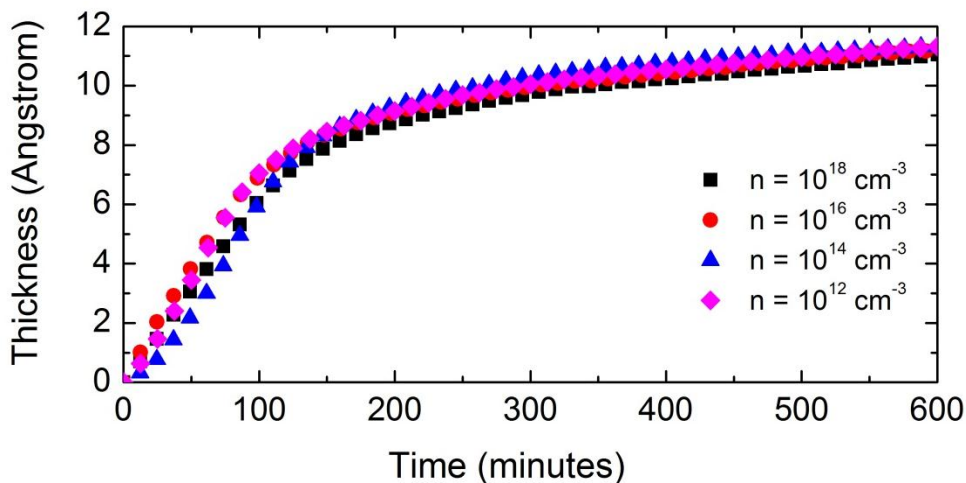


Figure 39. Evolutions of the oxide thicknesses for n-type materials as measured by SE.

To investigate whether this difference extends beyond the top two Si layers, we obtained thickness data on the same set of H-terminated samples as a function of time using SE. The results are surprising. As shown in Figure 39, except for an initial transient the oxide thicknesses increase at a common rate up to about 1 nm, where the measurements were terminated. The final data in Figure 39 include an approximate 0.2 nm contribution from adsorbed hydrocarbons. In fact weeks after the measurement the thickness stays almost same.

This is consistent with other data that we have obtained on a sample that we have measured occasionally for over 30 years. These results indicate that even if the initial chemical reactivities of the different types of bonds are significantly different, this distinction disappears after several Angstroms of oxidation.

4.4.2 p-type Surfaces^{‡‡}

Here, we extend the studies to (111) surfaces of p-type Si wafers (samples #7 - #9 from Table A) and also perform AFM measurements, which indicate significant surface reactivity in air.

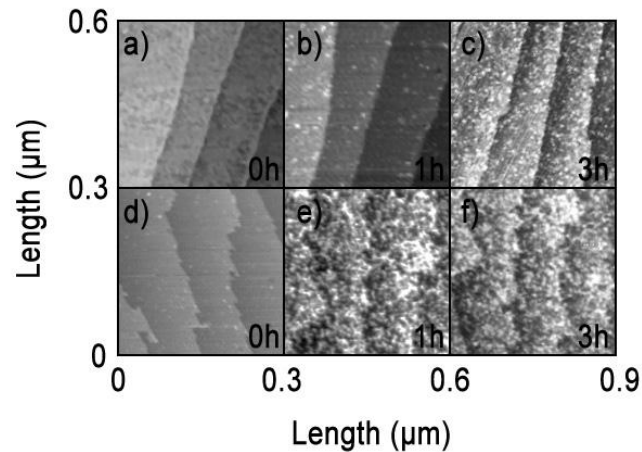


Figure 40. AFM scans of boron doped Si(111) samples for 0h, 1h, and 3h of oxidation in air (a)-(c) carrier concentration $p=1.3 \times 10^{15} \text{ cm}^{-3}$ (d)-(f) carrier concentration $p=5.1 \times 10^{18} \text{ cm}^{-3}$.

Figure 40 shows selections from the time dependent sequence of AFM images for lightly (upper panels) and heavily (lower panels) p-doped samples. In these sequences, the bright

^{‡‡} In part published in "Effect of p-type doping on the oxidation of H-Si(111) studied by second-harmonic generation"

Bilal Gokce, Daniel B. Dougherty, Kenan Gundogdu
 J. Vac. Sci. Technol. A 30, 040603 (2012)

protrusions indicate the effect of surface oxidation as described previously.¹⁰⁰ The effect of a high density of holes is evident by comparison. In panel A and D, the initial H-passivated surfaces exhibit flat terraces separated by monatomic steps. For the lightly doped sample, oxidation takes longer than three hours. On the other hand, the heavily doped material oxidizes relatively rapidly. Most of the surface is covered with a structure consistent with a typical natural oxide in less than one hour. A high concentration of holes obviously impacts surface reactivity significantly.

To gain insight into the bond-specific details of the process observed by AFM, we applied SHG to study the effect of p-type doping on the oxidation of the different surface bonds.

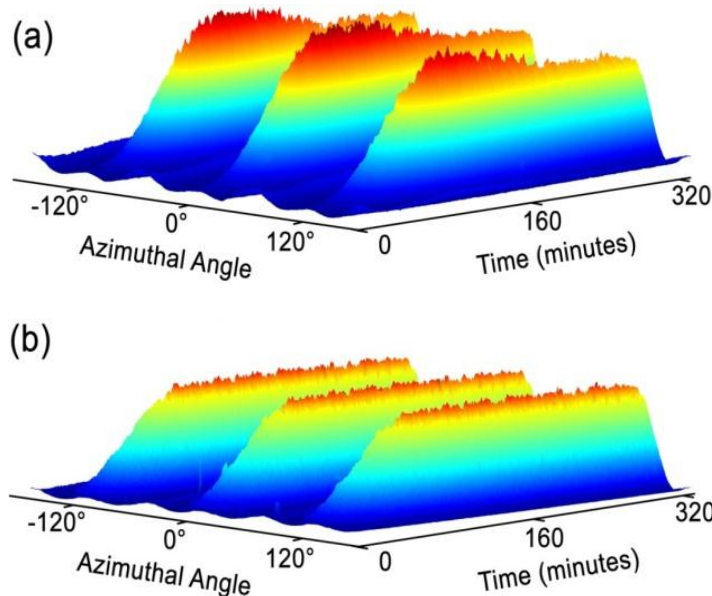


Figure 41. (a) Evolution of SHG during air exposure of an H-terminated Si(111) sample with $p=3.6 \times 10^{16} \text{ cm}^{-3}$ (b) as (a) but for $p=5.1 \times 10^{18} \text{ cm}^{-3}$.

Figure 41a and Figure 41b show SHG data for samples #8 and #9. Both are normalized to the level where the SHG responses no longer change with time. A comparison of the two figures illustrates a significant dependence on carrier concentration. The three features of the heavily doped sample (Figure 41b) rise almost linearly to their maximum value then remain constant

thereafter. In contrast, the same three features of the moderately doped sample (Figure 41a) reaches a higher maximum value and then decreases. We also note the existence of a 20 min incubation period for oxidation of the moderately doped sample.

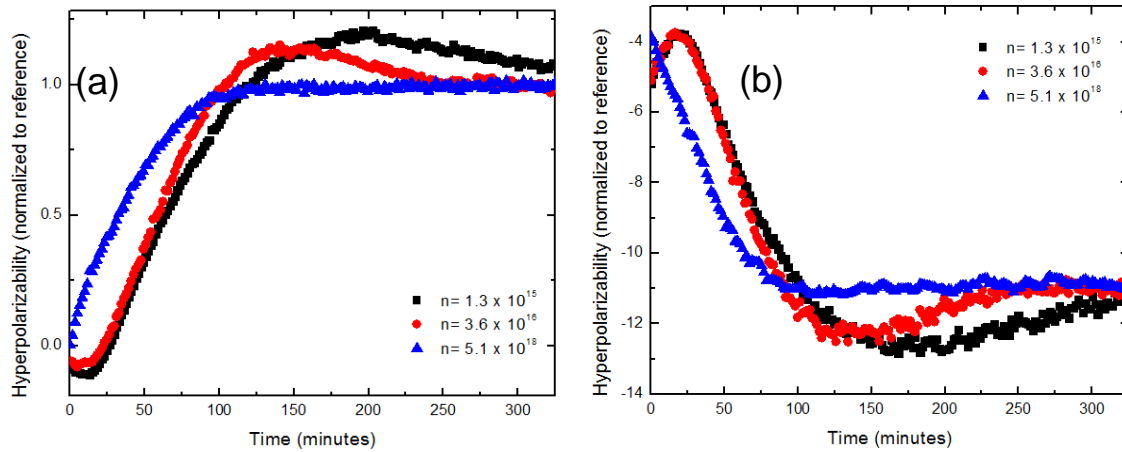


Figure 42. (a) Evolution of the average hyperpolarizabilities of the up bonds for boron-doped Si(111) samples with $p = 1.3 \times 10^{15}$, 3.6×10^{16} , and $5.1 \times 10^{18} \text{ cm}^{-3}$. (b) As (a), but for the Si back bonds.

To obtain a more quantitative understanding of the reaction dynamics of oxidation, we investigated the time evolution of the hyperpolarizabilities for up and back bonds in more detail. The bond model relates the SHG data to the hyperpolarizabilities of the different bonds. Figure 42 summarizes the results for all three samples, thereby highlighting the differences that occur for different carrier concentrations. With increasing concentration the curves shift to earlier times. At the highest hole concentration investigated here, both the incubation period and the peak near 2h have vanished completely. This shows that the up bond is now oxidizing as rapidly as the back bonds.

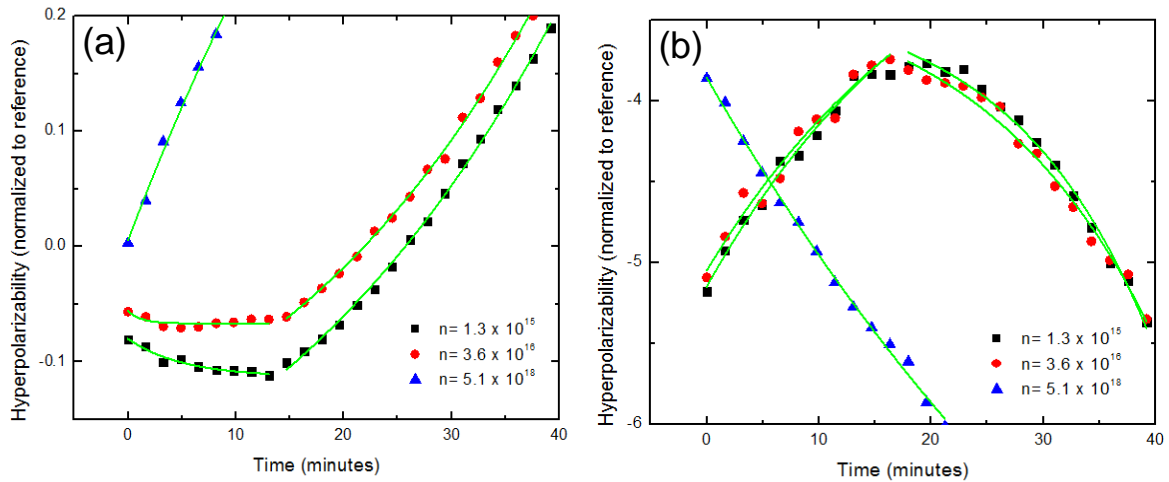


Figure 43. (a) first 40 min of Fig 2a; (b) first 40 min of Fig 2b. The green curves show the exponential fits.

We can make these observations quantitative by least-squares fitting simple exponential functions to the data. An expansion of the first 40 min of the data of Figure 41a is shown in Figure 43. The green curves show the exponential fits. The incubation period, if present, is fitted separately. The time constants for the incubation and rise periods are summarized in Table E.

Table E. Parameters yielding the best fits of exponential functions of the data of Fig. 4.

P	time constants (min)			
	up bonds		back bonds	
	incubation	Rise	Incubation	Rise
$1.3 \times 10^{15} \text{ cm}^{-3}$	-5.2 ± 0.5	33 ± 2	-23 ± 2	15 ± 2
$3.6 \times 10^{16} \text{ cm}^{-3}$	constant	28 ± 3	-22 ± 2	13 ± 2
$5.1 \times 10^{18} \text{ cm}^{-3}$	nonexistent	-22 ± 4	nonexistent	-54 ± 4

The analysis shows that the initial oxidation of p-type Si is dominated by the reaction dynamics of the up bonds. For carrier concentrations of $p = \sim 10^{15} \text{ cm}^{-3}$ as well as 10^{16} cm^{-3} we see that the incubation periods for the back bonds are identical. However, the reactivity of the up bonds clearly changes, further highlighting the dominant influence of up bonds during the incubation period. However, as time evolves the back bonds become more reactive and dominate the oxidation process. This is reflected in a faster rise times for these bonds. The extreme case is the $p = 5.1 \times 10^{18} \text{ cm}^{-3}$ sample. Here the incubation period is completely missing and the evolution is a simple exponential rise with a negative time constant.

From these observations it is clear that holes facilitate oxidation. The most significant effect occurs in the first step, where the -H of the Si-H up bond is replaced by -OH. This is evident not only from the vanishing incubation period and higher rise rates for the up bond, but also in the vanishing of a peak. For low doped samples the process is autocatalytic, whereas for highly doped samples the surfaces are already reactive. The negative time constant suggests a rise to saturation in these samples. These results are consistent with corrosion studies of Si and Ge in aqueous solutions, where the availability of holes which weakens the surface bonds is the rate-limiting step.¹⁰¹

4.5 Observation of Structural Dynamics

The observed oxidation anisotropies of strained surfaces also lead to bond-level structural dynamics that can be observed in SHG data. The Si-O bond length of 1.65 \AA is incommensurate with the Si-Si bond length of 2.35 \AA , so oxidation of particular bonds introduces microscopic strain that can cause additional structural changes. To investigate these effects, we determined the azimuth angles of the peaks of the SHG data of Figure 26. The azimuths were extracted by fitting the evolving features with Gaussian functions, although other functions could also be used without changing the results. These are shown in Figure 44A-C. They were also correlated with models created by MM2 force-field calculations, which are shown in Figure 44D-F. Due to program limitations it is not possible

to create a silicon lattice with more than 100 atoms, so the MM2 calculations are not quantitatively accurate. Nevertheless, they are sufficient to show trends.

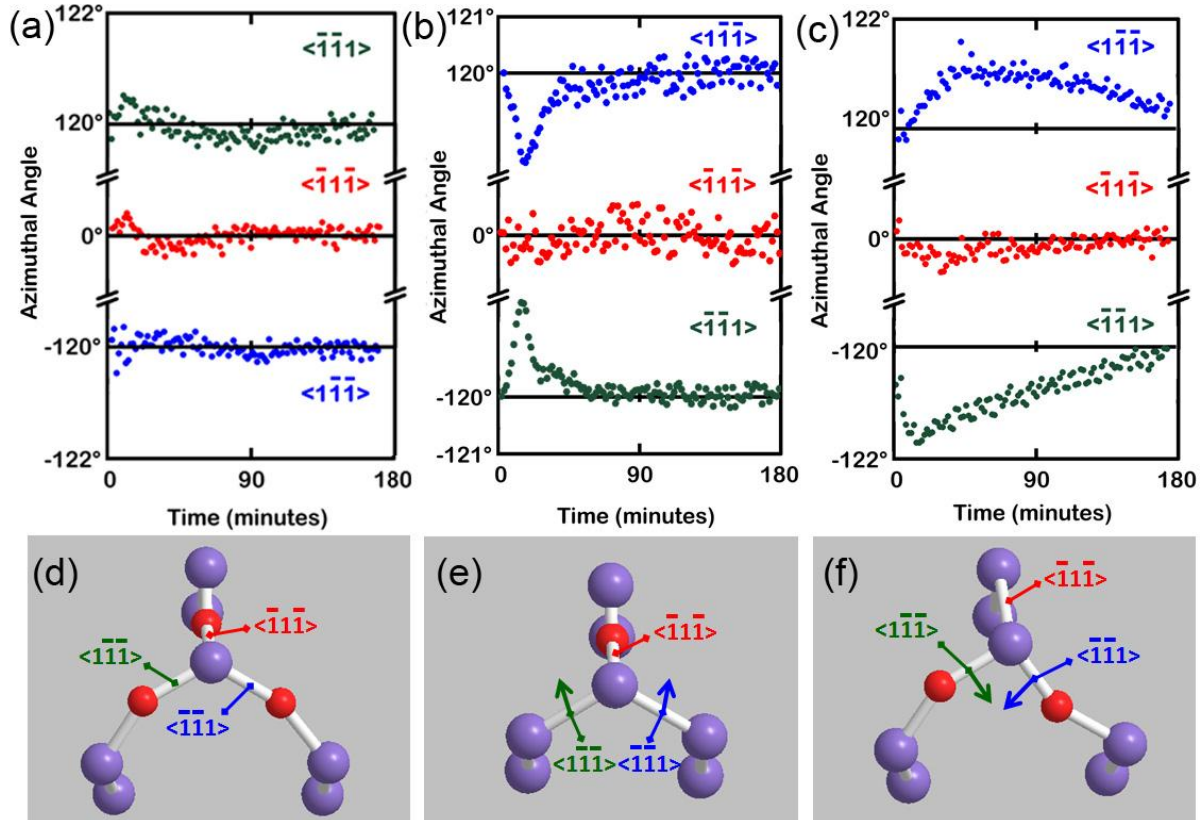


Figure 44. (a) Evolution of the azimuths of the dominant features for the unstrained on-axis sample. (b) As (c), but for the sample strained along $\langle \bar{1}\bar{2}\bar{1} \rangle$. (c) As (b) but for strain along $\langle \bar{1}0\bar{1} \rangle$. (d)-(f) Results of force-field calculations showing the result of O insertion in different bonds.

All figures show that the initial and asymptotic azimuths exhibit the expected equilibrium values for an unperturbed Si(111) lattice. This is also the case of the on-axis sample throughout oxidation, Figure 44A, where oxidation is stochastic and the average azimuthal angle for each bond remains constant to within $\pm 0.3^\circ$. However, significant discrepancies are seen for different bonds in Figure 44B and Figure 44C. In particular, for Figure 44B, where 0.06% strain is applied along $\langle \bar{1}\bar{2}\bar{1} \rangle$, the average azimuth-angle increase of several degrees

shows that the $\langle 1\bar{1}\bar{1} \rangle$ and $\langle \bar{1}\bar{1}1 \rangle$ bonds move away from each other upon oxidation but before oxidation is completed. This is consistent with the MM2 calculation shown in Figure 44E. When 0.05% strain is applied along $\langle \bar{1}01 \rangle$, Figure 44C shows that the average azimuth angles decrease by several degrees. Thus the $\langle 1\bar{1}\bar{1} \rangle$ and $\langle \bar{1}\bar{1}1 \rangle$ bonds both move closer to the $\langle \bar{1}\bar{1}\bar{1} \rangle$ bond. This is again consistent with the diagram provided in Figure 44F. These azimuthal variations indicate an initial accumulation, followed by a relaxation, of microscopic strain. While such local strains are necessarily a general consequence of oxidation, the fact that macroscopic strain makes oxidation anisotropic allows us to resolve properties of individual types of bonds and hence to observe the effect. These data together with the analysis of the experiment on the strained sample clearly indicate that SHG provides a bond sensitive structural characterization method. Oxidation of the vicinal sample is mandated by the step structure, hence no structural dynamics are observable.

4.6 Oxidation of methoxylated Si(111)

To test the validity of the two-step model⁹¹ that we use in the above discussions we investigate the oxidation of methoxylated Si(111). H-Si(111) (#2, Table A) was kept in a box with Methanol for 62hours while the box was continuously purged with Nitrogen. Methanol reacts with Si-H up-bonds to form H₂ and Si-OCH₃ oriented normal to the surface. However the reaction is free of any detectable back bond oxidation.^{85,102}

The evolution of the average magnitudes of the three SHG peaks for an oxidizing methoxylated Si(111) sample in air is shown in Figure 45.

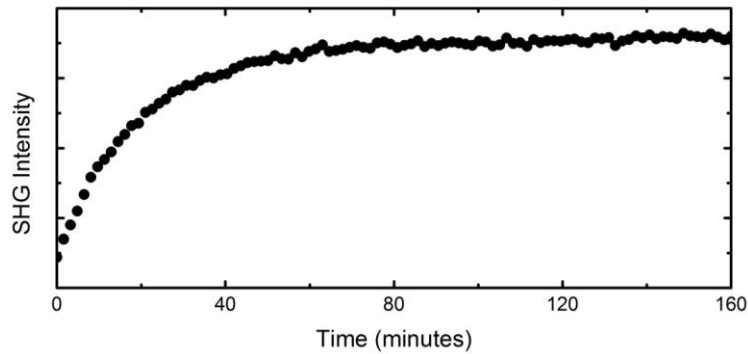


Figure 45. Evolution of the average magnitudes of the three SHG peaks for an oxidizing methoxylated Si(111) sample in air.

In contrast to Figure 30 we clearly observe a single exponential rise which indicates that the two-step process is reduced to a single reaction mechanism which we attribute to the obvious oxidation of the Si-Si back bonds.

4.7 Third-harmonic generation during oxidation of H-Si(100)

The nature of the third-rank tensor, responsible for second-harmonic generation, puts the following restriction on the SH processes: SHG can only resolve rotation axes not exceeding 3-fold symmetry. But macroscopically we have 4-fold symmetry in Si100, therefore we need at least Third-harmonic generation (THG) experiments to characterize the interface. Figure 46 shows a THG spectrum of Si(100) (Sample #10 from Table A).

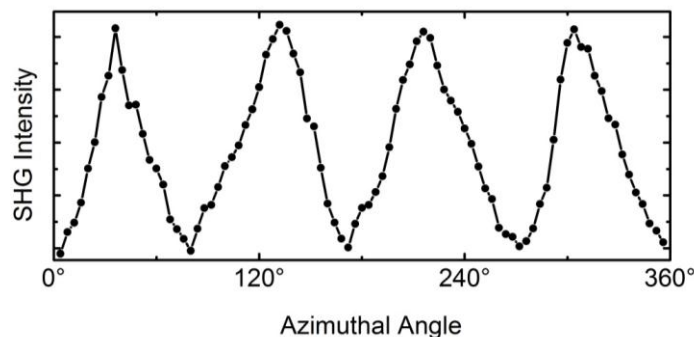


Figure 46. THG signal of a Si(100) sample.

The time evolution of the THG during the oxidation is illustrated in Figure 47.

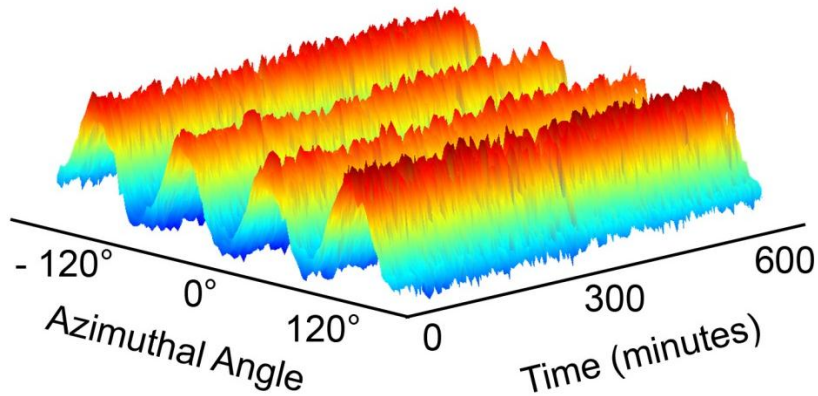


Figure 47. Time evolution of the THG response during oxidation of H-Si(100).

There is no change in the signal evident for 600 hours. This is attributed to the fact that for Si(100) the interface contributes no more than 5% to the total THG signal.¹⁰³ Since THG can't resolve the oxidation kinetics of this system, Fourth-Harmonic Generation (FHG) experiments are needed. The interface sensitivity of FHG is based on the same considerations described for SHG (see Section 2.3.1). However, FHG can't be realized with the laser system used for this thesis work due to its limited wavelength tunability.

5 Conclusion

Control of in-plane chemistry by manipulating reaction rates of certain bond directions is a novel concept, with potential applications in semiconductor technology. The first important step to achieving such control is the development of bond-specific methods that can characterize these effects. By applying a uniaxial strain during Si–SiO₂ interface formation, it is demonstrated that SHG provides the route to characterization followed by control for Si oxidation. We not only are able to control chemical reactivity along different bond directions, but also to probe structural evolution by measuring changes in bond directions.

The results presented in this thesis work are described with reference to a two-step oxidation process, where the H of the “up” bonds is first replaced by OH, followed by O insertion into the “back” bonds. The relatively strong dependences of these reactions on carrier concentration show why consistent results on the durability of H passivation have not been achieved. More interesting are the possibilities of directional oxidation. Anisotropic oxidation can be expected to lead to anisotropic properties in the underlying material, or to anisotropic protection in the case of further processing.

Previously, similar nonlinear optical experiments were modeled by tensorial calculations^{18,19,20}, which are based on the symmetry of the underlying Si lattice. However, our data emphasize that chemistry takes place in real time at the atomic scale, and that symmetry is an end result of chemical processes, i.e., it is not constant but evolves in time. Therefore, effective real-time analysis of nonlinear-optical signals requires models based on microscopic parameters. The ABM used in this work facilitates the interpretation of SHG experiments, expanding its applications to surface chemistry. The approach of using SHG to study dynamics is general, and can be applied to problems that range from bond formation during chemical changes on surfaces to bond dynamics in functional materials that exhibit phase transitions. Although Si might appear to be a special case owing to the relative lack of SHG signals from the bulk, the measurements done here depend mainly on differences with

respect to an intrinsic reference, and thus become more an issue of precision rather than accuracy. I anticipate that significantly more information will become available from these measurements once nonlinear-optical spectroscopy becomes routine.

6 References

1. Lee TH, Bhunia S, Mehregany M. Electromechanical Computing at 500 degrees C with Silicon Carbide. *Science*. Sep 2010;329(5997):1316-1318.
2. Guo LJ, Leobandung E, Chou SY. A silicon single-electron transistor memory operating at room temperature. *Science*. Jan 1997;275(5300):649-651.
3. Touahir L, Sam S, Moraillon A, et al. Functionalized Silicon Surfaces for Biological and Chemical Sensors. *Sens. Lett.* Jun 2010;8(3):447-456.
4. Borisov SM, Wolfbeis OS. Optical biosensors. *Chem. Rev.* Feb 2008;108(2):423-461.
5. Pike AR, Lie LH, Eagling RA, et al. DNA on silicon devices: On-chip synthesis, hybridization, and charge transfer. *Angew. Chem.-Int. Edit.* 2002;41(4):615-+.
6. Wei F, Sun B, Guo Y, Zhao XS. Monitoring DNA hybridization on alkyl modified silicon surface through capacitance measurement. *Biosens. Bioelectron.* Aug 2003;18(9):1157-1163.
7. Wagner P, Nock S, Spudich JA, et al. Bioreactive self-assembled monolayers on hydrogen-passivated Si(111) as a new class of atomically flat substrates for biological scanning probe microscopy. *J. Struct. Biol.* 1997;119(2):189-201.
8. Doshi P, Jellison GE, Rohatgi A. Characterization and optimization of absorbing plasma-enhanced chemical vapor deposited antireflection coatings for silicon photovoltaics. *Appl. Optics*. Oct 20 1997;36(30):7826-7837.
9. Shah A, Vallat-Sauvain E, Torres P, et al. Intrinsic microcrystalline silicon (μ c-Si : H) deposited by VHF-GD (very high frequency-glow discharge): a new material for photovoltaics and optoelectronics. *Materials Science and Engineering B-Solid State Materials for Advanced Technology*. Jan 19 2000;69:219-226.
10. Swanson RM. A vision for crystalline silicon photovoltaics. *Progress in Photovoltaics*. Aug 2006;14(5):443-453.
11. Vetterl O, Finger F, Carius R, et al. Intrinsic microcrystalline silicon: A new material for photovoltaics. *Solar Energy Materials and Solar Cells*. Apr 15 2000;62(1-2):97-108.

12. Iyengar VV, Nayak BK, More KL, et al. Properties of ultrafast laser textured silicon for photovoltaics. *Solar Energy Materials and Solar Cells*. Oct 2011;95(10):2745-2751.
13. Baragwanath AJ, Swift GP, Dai D, Gallant AJ, Chamberlain JM. Silicon based microfluidic cell for terahertz frequencies. *J. Appl. Phys.* Jul 2010;108(1).
14. Chen J-K, Li J-Y. Detection of specific DNA using a microfluidic device featuring tethered poly(N-isopropylacrylamide) on a silicon substrate. *Appl. Phys. Lett.* Aug 9 2010;97(6).
15. Sainiemi L, Nissila T, Kostiainen R, Ketola RA, Franssila S. A microfabricated silicon platform with 60 microfluidic chips for rapid mass spectrometric analysis. *Lab on a Chip*. 2011 2011;11(17):3011-3014.
16. Sharma S, Moniz AR-B, Triantis I, et al. An integrated silicon sensor with microfluidic chip for monitoring potassium and pH. *Microfluidics and Nanofluidics*. May 2011;10(5):1119-1125.
17. Harris NR, Hill M, Beeby S, et al. A silicon microfluidic ultrasonic separator. *Sensors and Actuators B-Chemical*. Oct 15 2003;95(1-3):425-434.
18. Yakovleva J, Davidsson R, Lobanova A, et al. Microfluidic enzyme immunoassay using silicon microchip with immobilized antibodies and chemiluminescence detection. *Analytical Chemistry*. Jul 1 2002;74(13):2994-3004.
19. Ku ISY, Reddyhoff T, Holmes AS, Spikes HA. Wear of silicon surfaces in MEMS. *Wear*. Jul 2011;271(7-8):1050-1058.
20. Mihailovic M, Rops CM, Hao J, Mele L, Creemer JF, Sarro PM. MEMS silicon-based micro-evaporator. *J. Micromech. Microeng.* Jul 2011;21(7).
21. Redondo A, Goddard WA, Swarts CA, McGill TC. Oxidation of Silicon Surfaces. *J. Vac. Sci. Technol.* 1981;19(3):498-501.
22. Warschkow O, Schofield SR, Marks NA, Radny MW, Smith PV, McKenzie DR. Water on silicon (001): C defects and initial steps of surface oxidation. *Phys. Rev. B*. May 2008;77(20).
23. Chowdhury ZR, Cho KV, Kherani NP. High-quality surface passivation of silicon using native oxide and silicon nitride layers. *Appl. Phys. Lett.* Jul 2012;101(2).

24. Hoex B, Schmidt J, Pohl P, van de Sanden MCM, Kessels WMM. Silicon surface passivation by atomic layer deposited Al(2)O(3). *J. Appl. Phys.* Aug 2008;104(4).
25. Leftwich TR, Teplyakov AV. Chemical manipulation of multifunctional hydrocarbons on silicon surfaces. *Surf. Sci. Rep.* Jan 2008;63(1):1-71.
26. Mazzone AM, Rizzoli R. Hydrocarbon molecules deposited onto silicon surfaces: A DFT study of adsorption and conductance. *Journal of Cluster Science.* Dec 2007;18(4):869-881.
27. Dhanekar S, Islam SS, Harsh. Photo-induced electrochemical anodization of p-type silicon: achievement and demonstration of long term surface stability. *Nanotechnology.* Jun 2012;23(23).
28. Brodoceanu D, Landstrom L, Bauerle D. Laser-induced nanopatterning of silicon with colloidal monolayers. *Appl Phys a-Mater.* Mar 2007;86(3):313-314.
29. Hurley PT, Ribbe AE, Buriak JM. Nanopatterning of alkynes on hydrogen-terminated silicon surfaces by scanning probe-induced cathodic electrografting. *Journal of the American Chemical Society.* Sep 2003;125(37):11334-11339.
30. Lu Y, Chen SC. Nanopatterning of a silicon surface by near-field enhanced laser irradiation. *Nanotechnology.* May 2003;14(5):505-508.
31. Hopper MA, Clarke RA, Young L. Thermal Oxidation of Silicon - Insitu Measurement of Growth-Rate Using Ellipsometry. *J. Electrochem. Soc.* 1975 1975;122(9):1216-1222.
32. Massoud HZ, Plummer JD, Irene EA. Thermal-Oxidation of Silicon in Dry Oxygen Growth-Rate Enhancement in the Thin Regime .1. Experimental Results. *J. Electrochem. Soc.* 1985 1985;132(11):2685-2693.
33. Deal BE, Grove AS. General Relationship for Thermal Oxidation of Silicon. *J. Appl. Phys.* 1965;36(12):3770.
34. Grove AS, Sah CT, Leistiko O. Redistribution of Acceptor + Donor Impurities during Thermal Oxidation of Silicon. *J. Appl. Phys.* 1964;35(9):2695.
35. Grove AS, Deal BE, Snow EH, Sah CT. Investigation of Thermally Oxidised Silicon Surfaces Using Metal-Oxide-Semiconductor Structures. *Solid State Electron.* 1965;8(2):145

36. Zhang X, Chabal YJ, Christman SB, Chaban EE, Garfunkel E. Oxidation of H-covered flat and vicinal Si(111)-1x1 surfaces. *J. Vac. Sci. Technol. A-Vac. Surf. Films.* Jul-Aug 2001;19(4):1725-1729.
37. Niwano M. In-situ IR observation of etching and oxidation processes of Si surfaces. *Surf. Sci.* Jun 1999;427-28:199-207.
38. Queeney KT, Chabal YJ, Weldon MK, Raghavachari K. Silicon oxidation and ultra-thin oxide formation on silicon studied by infrared absorption spectroscopy. *Phys. Status Solidi A-Appl. Res.* Sep 1999;175(1):77-88.
39. Niwano M, Kondo Y, Kimura Y. In-situ infrared observation of etching and oxidation processes of si surface in NH₄F solution. Vol 99. Pennington: *Electrochemical Society Inc*; 2002.
40. Ogawa H, Ishikawa K, Aoki M, et al. Observation of oxygen exposed hydrogen terminated silicon surfaces. Vol 96. Pennington: *Electrochemical Society Inc*; 1996.
41. Milekhin A, Friedrich M, Hiller K, Wiemer M, Gessner T, Zahn DRT. Infrared study of Si surfaces and buried interfaces. *J. Vac. Sci. Technol. B.* Jul-Aug 1999;17(4):1733-1737.
42. Lambers J, Hess P. In situ detection of F-2 laser-induced oxidation on hydrogen-terminated Si(111) and Si(110) surfaces by Fourier transform infrared transmission spectroscopy. *Thin Solid Films.* Dec 2001;400(1-2):111-115.
43. Fujimura S, Ishikawa K, Ogawa H. Analysis of native oxide growth process on an atomically flattened and hydrogen terminated Si (111) surface in pure water using Fourier transformed infrared reflection absorption spectroscopy. *J. Vac. Sci. Technol. A-Vac. Surf. Films.* Jan-Feb 1998;16(1):375-381.
44. Meyer C, Lupke G, Emmerichs U, et al. Electronic-Transitions at Si(111)/SiO₂ and Si(111)/Si₃N₄ Interfaces Studied by Optical 2nd-Harmonic Spectroscopy. *Phys. Rev. Lett.* Apr 10 1995;74(15):3001-3004.
45. Emmerichs U, Meyer C, Bakker HJ, et al. Optical 2nd-Harmonic Generation - A Probe of Atomic-Structure and Bonding at Si-SiO₂ Interfaces, and Other Chemically-Modified Si Surfaces. *J. Vac. Sci. Technol. B.* Jul-Aug 1994;12(4):2484-2492.
46. Hollering RWJ, Dijkkamp D, Elswijk HB. Optical 2nd-Harmonic Generation on a Vicinal Si(111) Surface. *Surf. Sci.* Feb 1991;243(1-3):121-126.

47. Hollering RWJ, Barmentlo M. Symmetry Analysis of Vicinal(111) Surfaces by Optical 2nd-Harmonic Generation. *Opt. Commun.* Mar 1992;88(2-3):141-145.
48. Jacob J, Silva AG, Fleischer K, McGilp JF. Optical second-harmonic generation studies of Si(111)-root 3x root 3-Ag and Si(111)-3x1-Ag grown on vicinal Si(111). Weinheim: *Wiley-V C H Verlag GmbH*; 2008.
49. Lupke G, Bottomley DJ, Vandriel HM. 2nd-Harmonic and 3rd-Harmonic Generation from Cubic Centrosymmetric crystals with vicinal faces -Phenomenological Theory and Experiment. *J. Opt. Soc. Am. B-Opt. Phys.* Jan 1994;11(1):33-44.
50. Verheijen MA, Vanhasselt CW, Rasing T. Optical 2nd Harmonic-Generation Study of Vicinal Si(111) Surfaces. *Surf. Sci.* Jul 1991;251:467-471.
51. Cundiff ST, Knox WH, Baumann FH, et al. Si/SiO₂ interface roughness: Comparison between surface second harmonic generation and x-ray scattering. *Appl. Phys. Lett.* Mar 1997;70(11):1414-1416.
52. Dadap JI, Doris B, Deng Q, Downer MC, Lowell JK, Diebold AC. Randomly Oriented Angstrom-Scale Microroughness at the Si(100) SiO₂ Interface Probed by Optical 2nd-Harmonic Generation. *Appl. Phys. Lett.* Apr 1994;64(16):2139-2141.
53. Bjorkman CH, Yasuda T, Shearon CE, et al. Influence of Surface-Roughness on The Electrical-Properties of Si-SiO₂ Interfaces and on 2nd-Harmonic Generation at these Interfaces. *J. Vac. Sci. Technol. B.* Jul-Aug 1993;11(4):1521-1527.
54. Kulyuk LL, Shutov DA, Strumban EE, Aktsipetrov OA. 2nd-Harmonic Generation by an SiO₂-Si Interface - Influence of the Oxide Layer. *J. Opt. Soc. Am. B-Opt. Phys.* Aug 1991;8(8):1766-1769.
55. Govorkov SV, Emelyanov VI, Koroteev NI, Petrov GI, Shumay IL, Yakovlev VV. Inhomogeneous Deformation of Silicon Surface-Layers Probed by 2nd-Harmonic Generation in Reflection. *J. Opt. Soc. Am. B-Opt. Phys.* Jun 1989;6(6):1117-1124.
56. Park H, Qi JB, Xu Y, et al. Boron induced charge traps near the interface of Si/SiO₂ probed by second harmonic generation. *Phys. Status Solidi B-Basic Solid State Phys.* Aug 2010;247(8):1997-2001.
57. Tolk NH, Alles ML, Pasternak R, et al. Oxide interface studies using second harmonic generation. *Microelectron. Eng.* Sep-Oct 2007;84(9-10):2089-2092.

58. Mihaychuk JG, Shamir N, van Driel HM. Multiphoton photoemission and electric-field-induced optical second-harmonic generation as probes of charge transfer across the Si/SiO₂ interface. *Phys. Rev. B*. Jan 1999;59(3):2164-2173.
59. Aktsipetrov OA, Fedyanin AA, Dadap JI, Downer MC. Dc-electric-field-induced second-harmonic generation studies of surfaces and buried interfaces of column IV semiconductors. *Laser Phys*. Nov-Dec 1996;6(6):1142-1151.
60. Ohlhoff C, Lupke G, Meyer C, Kurz H. Static and high-frequency electric fields in silicon MOS and MS structures probed by optical second-harmonic generation. *Phys. Rev. B*. Feb 1997;55(7):4596-4606.
61. Ehlert R, Kwon J, Downer MC. Optical second-harmonic and reflectance-anisotropy spectroscopy of molecular adsorption at Si(001) step-edges. Weinheim: *Wiley-VCH Verlag GmbH*; 2008.
62. Ehlert R PA, Loumakos L, Downer MC. Fingerprinting of Si Surface Bonds Using Nonresonant Optical Second-Harmonic Generation. *Nonlinear Optics: Materials, Fundamentals and Applications (NLO)*. 2011:NTuB5.
63. Maiman TH. Stimulated Optical Radiation in Ruby. *Nature*. 1960;187(4736):493-494.
64. Franken PA, Weinreich G, Peters CW, Hill AE. Generation of optical harmonics. *Phys. Rev. Lett*. 1961;7(4):118.
65. Shen YR. Laser Science: Past, Present, and Future. *AAPPS Bulletin*. 2005;15(2):22-31.
66. Sipe JE, Moss DJ, Vandriel HM. Phenomenological Theory of Optical 2nd-Harmonic and 3rd-Harmonic Generation from Cubic Centrosymmetric Crystals. *Phys. Rev. B*. Jan 1987;35(3):1129-1141.
67. Daum W, Krause HJ, Reichel U, Ibach H. Identification of Strained Silicon Layers at Si-SiO₂ Interfaces and Clean Si Surfaces by Nonlinear-Optical Spectroscopy. *Phys. Rev. Lett*. Aug 1993;71(8):1234-1237.
68. An YQ, Cundiff ST. Bulk and surface contributions to resonant second-harmonic generation from Si(001) surfaces. *Appl. Phys. Lett*. Dec 30 2002;81(27):5174-5176.

69. Hofer U, Li LP, Heinz TF. Desorption of Hydrogen From Si(100)2x1 at Low Coverages - The Influence Of Pi-Bonded Dimers on the Kinetics. *Phys. Rev. B.* Apr 15 1992;45(16):9485-9488.
70. Reider GA, Hofer U, Heinz TF. Desorption-Kinetics of Hydrogen from the Si(111)7x7 Surface. *J. Chem. Phys.* Mar 1 1991;94(5):4080-4083.
71. Powell GD, Wang JF, Aspnes DE. Simplified bond-hyperpolarizability model of second harmonic generation. *Phys. Rev. B.* May 2002;65(20).
72. Adles EJ, Aspnes DE. Application of the anisotropic bond model to second-harmonic generation from amorphous media. *Phys. Rev. B.* Apr 2008;77(16).
73. Kleinman DA, Ashkin A, Boyd GD. 2nd-Harmonic Generation of Light by Focused Laser Beams. *Phys Rev.* 1966;145(1):338.
74. Kleinman DA. Theory of Second Harmonic Generation of Light. *Phys Rev.* 1962;128(4):1761.
75. Levine BF. Bond-Charge Calculation of Nonlinear Optical Susceptibilities for Various Crystal-Structures. *Phys. Rev. B.* 1973;7(6):2600-2626.
76. Aspnes DE, Studna AA. Dielectric Functions and Optical-Parameters of Si, Ge, GaP, GaAs, GaSb, InP, InAs, and InSb from 1.5 to 6.0 eV. *Phys. Rev. B.* 1983;27(2):985-1009.
77. Shen YR. Principles of Nonlinear Optics: *Wiley*, Hoboken; 2003.
78. Cohen ML, Bergstre.Tk. Band Structures and Pseudopotential Form Factors for 14 Semiconductors of Diamond and Zinc-Blende Structures. *Phys Rev.* 1966;141(2):789.
79. Lautenschlager P, Garriga M, Vina L, Cardona M. Temperature-Dependence of the Dielectric Function and Interband Critical-Points in Silicon. *Phys. Rev. B.* Sep 1987;36(9):4821-4830.
80. Palik ED. *Handbook of Optical Constants of Solids*. Vol 1: Academic, Chestnut Hill, MA; 1998.
81. Munford ML, Cortes R, Allongue P. The preparation of ideally ordered flat H-Si(111) surfaces. *Sensor Mater.* 2001;13(5):259-269.

82. Dumas P, Chabal YJ. Electron-Energy-Loss Characterization of the H-Terminated Si(111) and Si(100) Surfaces Obtained by Etching in NH_4F . *Chem Phys Lett.* Jul 12 1991;181(6):537-543.
83. Wade CP, Chidsey CED. Etch-pit initiation by dissolved oxygen on terraces of H-Si(111). *Appl. Phys. Lett.* Sep 1997;71(12):1679-1681.
84. Michalak DJ, Amy SR, Aureau D, Dai M, Esteve A, Chabal YJ. Nanopatterning Si(111) surfaces as a selective surface-chemistry route. *Nat. Mater.* Mar 2010;9(3):266-271.
85. Michalak DJ, Amy SR, Esteve A, Chabal YJ. Investigation of the chemical purity of silicon surfaces reacted with liquid methanol. *J. Phys. Chem. C.* Aug 2008;112(31):11907-11919.
86. Aspnes DE, Harbison JP, Studna AA, Florez LT. Reflectance-Difference Spectroscopy System for Real-Time Measurements of Crystal-Growth. *Appl. Phys. Lett.* Mar 1988;52(12):957-959.
87. Papadimitriou D, Richter W. Highly sensitive strain detection in silicon by reflectance anisotropy spectroscopy. *Phys. Rev. B.* Aug 2005;72(7).
88. Liarokapis E, Papadimitriou D, Rumberg J, Richter W. Raman and RAS measurements on uniaxially strained thin semiconductor layers. *Physica Status Solidi B-Basic Research.* Jan 1999;211(1):309-316.
89. Aspnes DE, Studna AA. High Precision Scanning Ellipsometer. *Appl. Optics.* 1975;14(1):220-228.
90. Aspnes DE, Theeten JB. Optical-Properties of the Interface between Si and its thermally grown Oxide. *Phys. Rev. Lett.* 1979;43(14):1046-1050.
91. Miura T, Niwano M, Shoji D, Miyamoto N. Kinetics of oxidation on hydrogen-terminated Si(100) and (111) surfaces stored in air. *J. Appl. Phys.* Apr 1996;79(8):4373-4380.
92. MacLaren DA, Curson NJ, Atkinson P, Allison W. An AFM study of the processing passivated silicon(111) of a low miscut angle. *Surf. Sci.* Sep 2001;490(3):285-295.
93. Bensliman F, Sawada Y, Tsujino K, Matsumura M. Oxidation of atomically flat and hydrogen-terminated Si(111) surfaces by hydrogen peroxide. *J. Electrochem. Soc.* 2007;154(6):F102-F105.

94. Irene EA. 3-Dimensional Defects in amorphous SiO₂-Films. *J. Electrochem. Soc.* 1978;125(8):C352-C352.
95. Fuoss D, Topich JA. Heavy-Doping Effects and Impurity Segregation during High-Pressure Oxidation of Silicon. *Appl. Phys. Lett.* 1980;36(4):275-277.
96. Takizawa J, Ohno S, Koizumi J, Shudo K, Tanaka M. Real-time coverage monitoring of initial oxidation processes on Si(001) by means of surface differential reflectance. *J. Phys.-Condes. Matter.* May 2006;18(17):L209-L216.
97. Kamiura Y, Hasegawa K, Sano Y, Mizokawa Y, Kawamoto K. Initial oxidation phenomena of heavily phosphorus-doped silicon in dry oxygen. *J. Vac. Sci. Technol. B.* Nov-Dec 2002;20(6):2187-2191.
98. Ying WB, Mizokawa Y. Evaluation of the initial oxidation of heavily phosphorus doped silicon surfaces using angle-dependent X-ray photoelectron spectroscopy. *Thin Solid Films.* Apr 1999;343:393-396.
99. Hirayama H, Watanabe K, Kawada M. Doping dependence of second harmonic generation from native oxide/Si(111) interfaces. *Appl. Surf. Sci.* Jul 1996;100:460-464.
100. Neuwald U, Hessel HE, Feltz A, Memmert U, Behm RJ. Initial-Stages Of Native Oxide-Growth On Hydrogen Passivated Si(111) Surfaces Studied By Scanning Tunneling Microscopy. *Appl. Phys. Lett.* Mar 1992;60(11):1307-1309.
101. Beck F, Gerischer H. Zum Mechanismus der Anodischen Auflösung von Germanium in alkalischer Lösung. *Zeitschrift Fur Elektrochemie.* 1959;63(4):500-510.
102. Michalak DJ, Rivillon S, Chabal YJ, Esteve A, Lewis NS. Infrared spectroscopic investigation of the reaction of hydrogen-terminated, (111)-oriented, silicon surfaces with liquid methanol. *J. Phys. Chem. B.* Oct 2006;110(41):20426-20434.
103. Peng HJ, Aspnes DE. Calculation of bulk third-harmonic generation from crystalline Si with the simplified bond hyperpolarizability model. *Phys. Rev. B.* Oct 2004;70(16).

APPENDICES

Appendix A – Matlab Bond Model Code

```
clear all;
beta = 0.304083*2*pi; % 109.47 this angle is the angle between Si-bonds
gamma=0; % vicinal cut angle

%b's are the bond-vectors for silicon 111
b_1 = [0; 0; 1];
b_2 = [sin(beta); 0; cos(beta)]; %sin(120)=sqrt(3/2)
b_3 = [-0.5*sin(beta); (sqrt(3)/2)*sin(beta); cos(beta)]; %cos(120)=-0.5,
b_4 = [-0.5*sin(beta); -(sqrt(3)/2)*sin(beta); cos(beta)];

theta_i = (29.5/45)*pi/8;
theta_0 = (29.5/45)*pi/8;
e_p = 1; %incidence angle observation angle and E_field amplitude
E_p = [-e_p*cos(theta_i); 0; e_p*sin(theta_i)]; %p_polariz. incident pulse
k_shg = [-sin(theta_0); 0; cos(theta_0)]; %unit vector along the wave
vector of the shg light

%a's are the hyperpolarizabilities, these are assumed values
a_up = 554+515i
a_step = -28.2;
a_down1 = -28.2;
a_down2 = -28.2;
A = zeros(360,1);
B = zeros(360,1);
E_shg = zeros(3,360);

for k=1:360
    phi = (k-1)*2*pi/360;
    R_phi = [cos(phi) sin(phi) 0; -sin(phi) cos(phi) 0; 0 0 1];
    V_g = [cos(gamma) 0 sin(gamma); 0 1 0; -sin(gamma) 0 cos(gamma)];
    b_1a = R_phi*V_g*b_1;
    b_2a = R_phi*V_g*b_2;
    b_3a = R_phi*V_g*b_3;
    b_4a = R_phi*V_g*b_4;
    Ps_2 = a_up*(dot(b_1a,E_p))^2*b_1a;
    Ps_2 = Ps_2+a_step*(dot(b_2a,E_p))^2*b_2a;
    Ps_2 = Ps_2+a_down1*(dot(b_3a,E_p))^2*b_3a;
    Ps_2 = Ps_2+a_down2*(dot(b_4a,E_p))^2*b_4a;

    E_shg(:,k) = Ps_2 - dot(k_shg,Ps_2)*k_shg;
    A(k) = abs(E_shg(2,k))^2;
    B(k) = abs((E_shg(1,k)))^2+ abs((E_shg(3,k))).^2;
end
angle =0:2*pi/360:2*pi*359/360;
figure (8); plot(B);
```

Appendix B – Origin Fitting function

$$\begin{aligned}
 y(x) = & \text{abs}(b * (-\cos(0.00555555 * (x-1) * \pi) * \sin(0.608166 * \pi) * \cos(0.081944444 * \pi) + \cos(0.608166 * \pi) * \\
 & \sin(0.081944444 * \pi))^2 * \cos(0.002777777 * (2 * x - 2) * \pi) * \sin(0.608166 * \pi) + c * (-(-0.5 * \cos(0.00555555 * (x- \\
 & 1) * \pi) * \sin(0.608166 * \pi) + 0.5 * \sin(0.00555555 * (x-1) * \pi) * \sqrt{3} * \sin(0.608166 * \pi)) * \cos(0.081944444 * \pi) + \\
 & \cos(0.608166 * \pi) * \sin(0.081944444 * \pi))^2 * (-0.5 * \cos(0.002777777 * (2 * x - 2) * \pi) * \sin(0.608166 * \pi) + 0.5 * \\
 & \sin(0.002777777 * (2 * x - 2) * \pi) * \sqrt{3} * \sin(0.608166 * \pi)) + d * (-(-0.5 * \cos(0.00555555 * (x-1) * \pi) * \\
 & \sin(0.608166 * \pi) - 0.5 * \sin(0.00555555 * (x-1) * \pi) * \sqrt{3} * \sin(0.608166 * \pi)) * \cos(0.081944444 * \pi) \\
 & + \cos(0.608166 * \pi) * \sin(0.081944444 * \pi))^2 * (-0.5 * \cos(0.002777777 * (2 * x - 2) * \pi) * \sin(0.608166 * \pi) - \\
 & 0.5 * \sin(0.002777777 * (2 * x - 2) * \pi) * \sqrt{3} * \sin(0.608166 * \pi)) + (-\sin((0.081944444 * \pi) * (b * (- \\
 & \cos(0.00555555 * (x-1) * \pi) * \sin(0.608166 * \pi) * \cos(0.081944444 * \pi) + \cos(0.608166 * \pi) * \sin(0.081944444 * \pi))^2 \\
 & * \cos(0.002777777 * (2 * x - 2) * \pi) * \sin(0.608166 * \pi) + c * (-(-0.5 * \cos(0.00555555 * (x-1) * \pi) * \sin(0.608166 * \pi) \\
 & + 0.5 * \sin(0.00555555 * (x-1) * \pi) * \sqrt{3} * \sin(0.608166 * \pi)) * \cos(0.081944444 * \pi) + \cos(0.608166 * \pi) * \\
 & \sin(0.081944444 * \pi))^2 * (-0.5 * \cos(0.002777777 * (2 * x - 2) * \pi) * \sin(0.608166 * \pi) + 0.5 * \sin(0.002777777 * (2 * x - \\
 & 2) * \pi) * \sqrt{3} * \sin(0.608166 * \pi)) + d * (-(-0.5 * \cos(0.00555555 * (x-1) * \pi) * \sin(0.608166 * \pi) - \\
 & 0.5 * \sin(0.00555555 * (x-1) * \pi) * \sqrt{3} * \sin(0.608166 * \pi)) * \cos(0.081944444 * \pi) + \cos(0.608166 * \pi) \\
 & * \sin(0.081944444 * \pi))^2 * (-0.5 * \cos(0.002777777 * (2 * x - 2) * \pi) * \sin(0.608166 * \pi) - 0.5 * \sin(0.002777777 * (2 * x - \\
 & 2) * \pi) * \sqrt{3} * \sin(0.608166 * \pi))) + \cos(0.081944444 * \pi) * (a * \sin((0.081944444 * \pi))^2 + b * (-\cos(0.00555555 * (x- \\
 & 1) * \pi) * \sin(0.608166 * \pi) * \cos(0.081944444 * \pi) + \cos(0.608166 * \pi) * \sin(0.081944444 * \pi))^2 * \cos(0.608166 * \pi) \\
 & + c * (-(-0.5 * \cos(0.00555555 * (x-1) * \pi) * \sin(0.608166 * \pi) + 0.5 * \sin(0.00555555 * (x-1) * \pi) * \sqrt{3} * \\
 & \sin(0.608166 * \pi)) * \cos(0.081944444 * \pi) + \cos(0.608166 * \pi) * \sin(0.081944444 * \pi))^2 * \cos(0.608166 * \pi) + d * \\
 & (-(-0.5 * \cos(0.00555555 * (x-1) * \pi) * \sin(0.608166 * \pi) - 0.5 * \sin(0.00555555 * (x-1) * \pi) * \sqrt{3} * \sin(0.608166 * \pi)) * \\
 & \cos(0.081944444 * \pi) + \cos(0.608166 * \pi) * \sin(0.081944444 * \pi))^2 * \cos(0.608166 * \pi))) * \sin(0.081944444 * \pi))^2 \\
 & + \text{abs}(a * \sin((0.081944444 * \pi))^2 + b * (-\cos(0.00555555 * (x-1) * \pi) * \sin(0.608166 * \pi) * \cos(0.081944444 * \pi) + \\
 & \cos(0.608166 * \pi) * \sin(0.081944444 * \pi))^2 * \cos(0.608166 * \pi) + c * (-(-0.5 * \cos(0.00555555 * (x-1) * \pi) \\
 & * \sin(0.608166 * \pi) + 0.5 * \sin(0.00555555 * (x-1) * \pi) * \sqrt{3} * \sin(0.608166 * \pi)) * \cos(0.081944444 * \pi) + \\
 & \cos(0.608166 * \pi) * \sin(0.081944444 * \pi))^2 * \cos(0.608166 * \pi) + d * (-(-0.5 * \cos(0.00555555 * (x-1) * \pi) * \\
 & \sin(0.608166 * \pi) - 0.5 * \sin(0.00555555 * (x-1) * \pi) * \sqrt{3} * \sin(0.608166 * \pi)) * \cos(0.081944444 * \pi) + \\
 & \cos(0.608166 * \pi) * \sin(0.081944444 * \pi))^2 * \cos(0.608166 * \pi) - (-\sin((0.081944444 * \pi) * (b * (- \\
 & \cos(0.00555555 * (x-1) * \pi) * \sin(0.608166 * \pi) * \cos(0.081944444 * \pi) + \cos(0.608166 * \pi) * \\
 & \sin(0.081944444 * \pi))^2 * \cos(0.002777777 * (2 * x - 2) * \pi) * \sin(0.608166 * \pi) + c * (-(-0.5 * \cos(0.00555555 * (x- \\
 & 1) * \pi) * \sin(0.608166 * \pi) + 0.5 * \sin(0.00555555 * (x-1) * \pi) * \sqrt{3} * \sin(0.608166 * \pi)) * \cos(0.081944444 * \pi) + \\
 & \cos(0.608166 * \pi) * \sin(0.081944444 * \pi))^2 * (-0.5 * \cos(0.002777777 * (2 * x - 2) * \pi) * \sin(0.608166 * \pi) \\
 & + 0.5 * \sin(0.002777777 * (2 * x - 2) * \pi) * \sqrt{3} * \sin(0.608166 * \pi)) + d * (-(-0.5 * \cos(0.00555555 * (x-1) * \pi) *
 \end{aligned}$$

$$\begin{aligned}
& \sin(0.608166\pi) - 0.5 \sin(0.00555555(x-1)\pi) \sqrt{3} \sin(0.608166\pi) \cos(0.081944444\pi) + \\
& \cos(0.608166\pi) \sin(0.081944444\pi)^2 (-0.5 \cos(0.002777777(2x-2)\pi) \sin(0.608166\pi) - \\
& 0.5 \sin(0.002777777(2x-2)\pi) \sqrt{3} \sin(0.608166\pi)) + \cos(0.081944444\pi) * \\
& (a \sin((0.081944444)\pi)^2 + b (-\cos(0.00555555(x-1)\pi) \sin(0.608166\pi) \cos(0.081944444\pi) \\
& + \cos(0.608166\pi) \sin(0.081944444\pi)^2 \cos(0.608166\pi) + c (-(-0.5 \cos(0.00555555(x-1)\pi) * \\
& \sin(0.608166\pi) + 0.5 \sin(0.00555555(x-1)\pi) \sqrt{3} \sin(0.608166\pi) \cos(0.081944444\pi) \\
& + \cos(0.608166\pi) \sin(0.081944444\pi)^2 \cos(0.608166\pi) + d (-(-0.5 \cos(0.00555555(x-1)\pi) * \\
& \sin(0.608166\pi) - 0.5 \sin(0.00555555(x-1)\pi) \sqrt{3} \sin(0.608166\pi) \cos(0.081944444\pi) + \\
& \cos(0.608166\pi) \sin(0.081944444\pi)^2 \cos(0.608166\pi))) \cos(0.081944444\pi))^2 + e
\end{aligned}$$